FERROMAGNETIC RESONANCE IN NICKEL AT LOW TEMPERATURES

by

Jeffrey MacLeod Rudd

B.Sc.(Honours), Simon Fraser University, 1981

A THESIS SUBMITTED IN PARTIAL FULFILLMENT OF

THE REQUIREMENTS FOR THE DEGREE OF

MASTER OF SCIENCE

in the Department

of

Physics

© Jeffrey MacLeod Rudd November 1985

SIMON FRASER UNIVERSITY

1985

All rights reserved. This work may not be reproduced in whole or in part, by photocopy or other means, without permission of the author.

APPROVAL

Name: Jeffrey MacLeod Rudd

Degree: Master of Science

Title of Thesis: Ferromagnetic Resonance in Nickel at Low Temperatures

Examining committee:

Chairman: R. H. Enns

J. F. Cochran

Senior Supervisor

E. D. Crozier

B. Heinrich

C. E. Patton

External Examiner

Department of Physics

Colorado State University

Date Approved: November 29, 1985

PARTIAL COPYRIGHT LICENSE

I hereby grant to Simon Fraser University the right to lend my thesis, project or extended essay (the title of which is shown below) to users of the Simon Fraser University Library, and to make partial or single copies only for such users or in response to a request from the library of any other university, or other educational institution, on its own behalf or for one of its users. I further agree that permission for multiple copying of this work for scholarly purposes may be granted by me or the Dean of Graduate Studies. It is understood that copying or publication of this work for financial gain shall not be allowed without my written permission.

Title of Thesis/Project/Extended Essay

FERROMAGNETIC RESONANCE IN NICKEL

AT LOW TEMPERATURES

Author: _____

(signature)

JEFFREY MacLEOD RUDD

(name)

Dec 12 1985

(date)

ABSTRACT

Ferromagnetic resonance has been measured at 24 GHz in (110) nickel disks at 4 K and from 60 K to room temperature. Samples had a nominal purity of 99.99% and a residual resistivity ratio of 38. The applied field was in the plane of the sample and measurements were made with the field along each of the three principal axes (100), (111) and (110). The room temperature linewidth was found to be isotropic within experimental uncertainty, and the linewidth, ΔH, was found to be 360 Oe. The experimental results indicated that the linewidth is anisotropic at low temperatures. We found $\Delta H_{110} > \Delta H_{111}$ and ΔH_{100} for temperatures below 200 K. At 4 K we found $\Delta H_{100} = 1620 \pm 50$ Oe, $\Delta H_{111} = 1815 \pm 50$ Oe and $\Delta H_{110} = 2050 \pm 50$ Oe. Kambersky has suggested that the large increase in magnetic damping in Nickel on cooling to 4 K is due to the presence of degenerate states at the Fermi surface near the X points of the Brillouin zone. The contribution of these states to the damping has been calculated using a simple model of electrons and spin waves coupled via the spin-orbit interaction. The results exhibited qualitatively the temperature dependence of the damping but the calculated damping parameters were approximately 1/200 those required by experiment. The predicted anisotropy of the linewidth did not agree with experiment. The calculation indicated that ΔH_{100} should be greater than ΔH_{111} by approximately 4% at 4 K. It is suggested that the large sheets of the Fermi surface play an important role in the magnetic damping of Nickel at low temperatures.

ACKNOWLEDGEMENTS

I would like to thank John Cochran for his assistance and patience with this work. I would also like to thank the members of our research group Bret Heinrich, Ken Myrtle and Ken Urquhart for their many contributions. Thanks also to Qiao Rongwen and John Dutcher, to the members of my Committee Carl Patton and Daryl Crozier, and to fellow grad students and otherwise Mike Denhoff, Don Hunter, Andrew Kurn, Bill McMullan and John Simmons.

Finally, I wish to acknowledge the financial support of the Natural Sciences and Engineering Research Council and of Simon Fraser University.

TABLE OF CONTENTS

LIST OF TABLES

LIST OF FIGURES

1. INTRODUCTION

1.1 Introduction

In the work reported in this thesis we were interested in the magnetic damping processes operating in Nickel at low temperatures. These magnetic damping processes are largely responsible for the Ferromagnetic Resonance (FMR) linewidth. The temperature dependence of the FMR linewidth in pure Nickel has been a subject of interest since 1966 when Bhagat and Hirst[1] found that the linewidth increased with decreasing temperature and reached a saturation value at approximately 20 K. Kambersky[2] in 1970 suggested a damping mechanism for Nickel in which the damping increased with an increase in the electron lifetime. This work was extended to low temperatures by Korenman and Prange[3,4]. They found that the magnetic damping should increase with an increasing electron lifetime and that the FMR linewidth should saturate at sufficiently long electron lifetimes. This was the behaviour observed by Bhagat and Hirst.

A qualitative argument, presented below, suggests that the Kambersky-Korenman-Prange damping mechanism may lead to an FMR linewidth which differs depending on whether the applied magnetic field is parallel to a (100), a (111) or a (110)

crystal axis. The difference between the linewidths for the different crystal axes should be greatest at low temperatures where the linewidth had reached its saturation value.

We have attacked this possibility of an anisotropic FMR linewidth at low temperatures in two ways. We have performed the experiment and find that the linewidth is indeed anisotropic. We have carried out a calculation of the damping to be expected from certain electron states on the Fermi surface of Nickel which were thought to be largely responsible for the increase in damping at low temperatures. The results of this calculation indicate that these states do not account for the magnitude or the anisotropy of the linewidth observed in experiment.

In this introductory chapter we give a very brief description of FMR in metals to provide a background to the work presented in this thesis. This description concludes with the presentation of our results. The final section of this chapter is a brief historical overview of experimental work relevant to our work. To extract information from an experimental FMR curve it is necessary to compare the data with the results of a calculation. The theory which is used for these comparisons is the subject of Chapter 2. The experimental details are discussed in Chapter 3. In Chapter 4 the experimental results are presented and compared with the calculations of Chapter 2. The calculation of the damping parameter is carried out in Chapter 5.

Introduction to FMR

For a description of FMR we start with the simplest possible situation: a free electron at rest in a uniform magnetic field H_0. In equilibrium the electron spin magnetic moment, $\bar{\mu}$, will lie parallel with the magnetic field. The spin angular momentum will point opposite to the magnetic field since the magnetic moment points in the opposite direction to the angular momentum. If we start with the spin parallel to the field, rotate it away from the field direction and let it go, what happens? There is a torque on the electron spin of $\bar{\tau} = \bar{\mu} \times \bar{H}_0$ so the spin will precess around the field direction at a circular frequency $\omega = \gamma H_0$, where γ is the gyromagnetic ratio, $\gamma = g|e|/2mc$, the ratio of the magnetic moment to the angular momentum. The precession is in a clockwise sense when looking along the field direction, and the angle of precession is a constant. For an electron $\gamma = 1.76 \times 10^7$ $Oe^{-1}sec^{-1}$ so that in a magnetic field of 2 kOe, say, the precession frequency is 5.6 GHz, which is in the microwave range. If the electron interacts with other objects the precessional motion may be damped as energy is transferred to the surroundings. The angle of precession will decrease with time so that the direction of the spin will spiral in to the field direction. The precessional frequency depends on the magnitude of the applied field. If energy is supplied by a magnetic field which varies

in time with a fixed frequency ω, and the magnitude of the applied field is varied the precessing spin will absorb energy when the resonance condition, $\omega = \gamma H_0$, is satisfied.

We are interested in ferromagnetic materials - materials where Avogadro's number of electron spins have been welded into one giant magnetic moment by the quantum mechanical exchange interaction. What happens in this situation when the material is placed in an applied field? First of all because of electron spin-electron spin and electron spin-lattice interactions the field the electron spins 'see' is not just the applied field H_0. The dipole-dipole interaction between the spins leads to a demagnetizing field. Coupling between the orbital motion of the electrons and their spins leads to magnetocrystalline anisotropy torques, to magnetoelastic torques and to dissipative torques. If the direction of the magnetization changes rapidly in space the exchange interaction can produce a torque on the magnetization. These effects must be considered when analysing the behaviour of the ferromagnet in a magnetic field.

The behaviour of the magnetization is described by the Landau-Lifshitz equation[5]:

$$-1/\gamma \, \partial\bar{M}/\partial t = \bar{M} \times \bar{H}_{eff} + \bar{\tau}_D \qquad (1.1)$$

where $\bar{M}$ is the magnetic moment per unit volume of the material,

and $\bar{H}_{eff}$ is the effective field acting on the magnetization which includes applied fields, demagnetizing fields, and effective fields describing the torques exerted by magnetocrystalline anisotropy and exchange. The damping torques are included as $\bar{\tau}_D$. This equation and the terms entering it are discussed in Chapter 2.

When displaced from equilibrium the magnetization precesses as in the free electron case. The natural frequency is no longer γH_0 but depends on the sample shape, the direction of the applied field with respect to the sample, magnetocrystalline anisotropy, exchange and damping. For example, if a disk shaped sample is used, with the applied field parallel to the plane of the disk (the configuration used in our experiments) resonance occurs when:

$$(\omega/\gamma)^2 = H_0(H_0 + 4\pi M_s) \tag{1.2}$$

in the absence of magnetocrystalline anisotropy, exchange and damping. A Ferromagnetic Resonance experiment consists of irradiating a ferromagnetic sample in an applied field with microwaves of a fixed frequency. The magnitude of the applied field is varied and the energy absorbed by the sample as a function of the field is measured. When the applied field satisfies the resonance condition the energy absorbed becomes a maximum.

The quantities which combine to determine the shape and position of the FMR absorption line include the saturation magnetization $4\pi M_s$, the g-factor, the magnetocrystalline anisotropy constants K1, K2..., the exchange constant A, and the damping torques, usually described by a phenomenological damping constant G (Gilbert damping) or λ (Landau-Lifshitz damping). In practice these quantities are so entangled in determining the value of the applied field at which resonance occurs, H_{fmr}, the linewidth, ΔH, and the lineshape that it is often difficult to extract values for the material parameters from an experimental curve. However measurement of the FMR linewidth provides information about the magnetic damping processes which cannot be so easily obtained using any other technique.

In discussing FMR it is often useful to think in terms of spin waves, which are collective modes of the electron spin system. In the ferromagnetic ground state all the electron spins are parallel. Deviations from this lowest energy configuration may be described as the excitation of spin waves. In particular the precessional motion of the magnetization may be described in terms of spin waves, so that in this picture FMR consists of the excitation of spin waves by the microwave field. Spin waves are characterized by an approximately quadratic dependence of frequency, ω, on wavenumber, k. For spin waves propagating at right angles to the magnetization (as in our experiments) the dispersion relation is[6]:

$$\omega = \gamma\sqrt{(H_0+2Ak^2/M_s)(H_0+4\pi M_s+2Ak^2/M_s)} \qquad (1.3)$$

where A is the exchange constant. Spin waves may be thought of as quasi-particles which interact with other quasi-particles in the system, for example with the conduction electrons in a metal, or with phonons. Magnetic damping occurs when a spin wave is annihilated in a collision with an electron or a phonon.

In an insulating medium the wavenumber of the microwave field is $k \simeq 2\pi/\lambda_0$, where λ_0 is the free space wavelength. For microwaves k is of the order of a few cm^{-1}. FMR occurs when the frequency and wavenumber (energy and momentum) of a spin wave matches the frequency and wavenumber of the microwave field. For k of the order of a few cm^{-1} $2Ak^2/M_s < H_0$ at FMR and resonance occurs when:

$$\omega = \gamma\sqrt{H_0(H_0+4\pi M_s)} \qquad (1.4)$$

The FMR Linewidth in Metals

In pure metals the FMR linewidth is largely due to two contributions: the exchange-conductivity mechanism, and what is described as the intrinsic damping. The relative importance of these two contributions differs from metal to metal. In Nickel the intrinsic damping is the major factor. For example, at room temperature and a microwave frequency of 24 GHz, approximately

300 Oe of the 320 Oe linewidth arises from the intrinsic damping with approximately 20 Oe being due to exchange-conductivity. In Iron however the exchange-conductivity line broadening is larger than the width due to the intrinsic damping. At room temperature and 24 GHz approximately 95 Oe of the 110 Oe linewidth comes from exchange-conductivity broadening with approximately 15 Oe being due to the intrinsic damping.

The Exchange-Conductivity Broadening

Penetration of microwaves into a metal is limited by the skin effect. For a metal in which the electrical conduction may be described by Ohm's law, $j = \sigma_0 e$, where j is the current density, e is the electric field and σ_0 is the dc conductivity, the spatial variation of the microwave fields with distance, z, into the metal is:

$$e(z) = e(0)\exp[(i-1)z/\delta] \qquad (1.5)$$

where δ is the skin depth. The skin depth is, in CGS units:

$$\delta^2 = c^2/2\pi\sigma_0\omega\mu \qquad (1.6)$$

where c is the speed of light and μ is the permeability. For typical metals at microwave frequencies the skin depth is of the order of half a micron. The skin depth depends on the magnitude

of the applied field since the permeability changes as the applied field is swept reaching a maximum at FMR (see Chapter 2). The spatial variation of the microwave fields leads to a spatial variation of the magnetization. The resulting non-uniformity produces an exchange torque which acts to restore the parallelism of the electron spins.

The Fourier spectrum of the field (1.5) consists of a distribution of wavevectors, q, the real part of which exhibits a maximum at $q = 1/\delta$, and has a width of roughly $1/\delta$. Typical values of q at FMR are 10^4-10^5 cm^{-1}, much larger than for an insulator. Spin waves will be excited over a range of values of the applied field, leading to a broadening of the resonance and to a shift from (1.4) in the field at which resonance occurs. These effects increase with a decreasing skin depth, that is, with an increasing conductivity. The combined effects of exchange and conductivity on the resonance lineshape have been discussed by Ament and Rado[7].

Since the conductivity of a pure metal increases with decreasing temperature this exchange-conductivity broadening may become large at low temperatures. At low temperatures the conduction electron mean free path, l, may become comparable with the skin depth (the 'anomalous skin effect regime'). If this occurs Ohm's law is no longer valid and the conductivity becomes 'non-local' or 'wavenumber dependent' (see Chapter 2). The skin depth is no longer (1.6) but instead saturates at a value $\delta_A = (\delta^2 l)^{1/3}$[8]. Since the permeability is large at FMR,

the skin depth is small, and the wavenumber dependence of the conductivity may become important at much higher temperatures than for non-magnetic metals. The result of the wavenumber dependence of the conductivity is that the exchange-conductivity broadening is reduced from that which would be expected based on the dc conductivity. The treatment of FMR using a wavenumber dependent conductivity has been discussed by Hirst and Prange[9].

The Intrinsic Damping

The intrinsic damping has its origin in the coupling between the electron spin system and the crystal lattice through the spin-orbit interaction. In the presence of spin-orbit coupling electron states are no longer spin eigenstates but contain a mixture of up and down spin character. Scattering of an electron, by phonons or impurities, may change the total spin of the system resulting in magnetic damping. The major contribution to the damping due to this mechanism comes from 'spin-flip' scattering in which an electron is scattered from a state of predominantly one spin character to a state of predominantly the opposite spin character, in a different energy band. This inter-band scattering damping mechanism has been considered by Elliott[10] and Kambersky[2]. The damping due to this mechanism varies inversely with the electron relaxation time, or, equivalently, varies as the electrical resistivity.

As a result of spin-orbit coupling the energy of an electron state may be shifted from the energy in the absence of spin-orbit coupling. In ferromagnetic materials the shift may depend on the direction of the magnetization with respect to the crystal axes. The effects of these energy shifts may be large, for example, the shifts are the origin of magnetocrystalline anisotropy, see for example, Kondorskii[11]. In an FMR experiment the precession of the magnetization causes the energies of the electron states to vary periodically with time. This variation is a source of magnetic damping. The simplest way to picture this damping mechanism is to consider the electron spin system and the electron system as distinct and to consider the coupling between them introduced by the spin orbit interaction. An electron on the Fermi surface and a spin wave may collide because of this coupling with the annihilation of the spin wave and scattering of the electron. Energy and momentum must be conserved in such a collision. Energy conservation restricts the scattering to states in the same energy band ('intra-band scattering') because the spin wave energy is much smaller than the electron kinetic energy. The annihilation of a spin wave produces magnetic damping. This damping mechanism was suggested by Kambersky[2] who showed that, near room temperature, the damping should increase with the electron relaxation time, that is it should increase as the electrical conductivity. This work was extended to low temperatures by Korenman and Prange[3,4]. They found that the

damping due to this mechanism became wavenumber dependent and varied as the wavenumber dependent conductivity. For a spherical Fermi surface they found that the Gilbert damping parameter varied as:

$$G(q) \propto \arctan(ql)/q \qquad (1.7)$$

where q is the wavenumber of the electromagnetic field in the metal, and l is the electron mean free path. The mean free path is related to the relaxation time by the Fermi velocity, $l = v_F\tau$. The linewidth due to this damping mechanism increases with increasing relaxation time (decreasing temperature) eventually reaching a constant value, independent of the relaxation time, in the limit $ql >> 1$ (the extreme anomalous limit).

Intra-band Scattering in Nickel

The increase with decreasing temperature and eventual saturation of the linewidth is the behaviour that was observed in pure Nickel at low temperatures and 22 GHz by Bhagat and Hirst[1] and Bhagat and Lubitz[12,13]. They found that the FMR linewidth increased with decreasing temperature starting at approximately 150 K and reached a plateau at approximately 20 K of roughly five times the room temperature value. The value of the linewidth at this plateau was found to be independent of the

residual resistivity ratio (ρ_{295}/ρ_4) of the samples if this ratio was greater than 30. The increase in linewidth was much larger than could be accounted for by any increase in the exchange conductivity broadening due to the increased conductivity.

Lloyd and Bhagat[14] performed experiments with Nickel-Copper alloys to test the dependence of the increase in the linewidth on the resistivity ratio. It was found that the increase in the linewidth disapppeared in a 5.4% Cu-Ni alloy which had a resistivity ratio of 3. The magnetization and other magnetic properties were not much affected by alloying so the results were interpreted as evidence that the increase in the linewidth and the increase in the electron relaxation time were related.

Further evidence for the wavenumber dependence of the damping came from the measurements of Heinrich, Meredith and Cochran[15] in which the transmission of microwaves through thin samples of Nickel was measured as a function of the applied field. At the field corresponding to Ferromagnetic Antiresonance (FMAR) the permeability is small (in the absence of damping it is zero). The skin depth at FMAR is much larger than at FMR so that the typical wavenumbers are much smaller at FMAR than at FMR. The damping parameters deduced from the FMAR data were much larger than those quoted by Bhagat and Lubitz[12] in the same temperature range. This is what would be expected from a damping of the form of equation (1.7) since $\arctan(ql)/q$

decreases with increasing q.

In Nickel a large contribution to this intra-band damping is conjectured to come from d-band minority spin states near the X-points in the Brillouin zone[2] (the X-points are at the zone edge in the (100) directions). The Fermi surface from these bands is a set of three approximately ellipsoidal surfaces centered at the X-points with the long axis of the ellipse along the axis connecting X with the center of the Brillouin zone. These surfaces are called the X_5 hole pockets. In the absence of spin orbit coupling the X_5 level is doubly degenerate. The degeneracy is lifted by the spin orbit interaction, the splitting between the two levels depending on the direction of the magnetization with respect to the crystal axes[16]. As a result the size and the shape of the pockets depends on the direction of the magnetization. For example with the applied field along (111) all three pockets are equivalent. With the magnetization along (100) the pocket along the field direction is smaller in all dimensions than the pockets that are at the X-points perpendicular to the field direction.

In a collision between an electron and a spin wave energy and momentum must be conserved. At low temperatures, long electron relaxation times, conservation of momentum restricts the electrons which may collide with a spin wave to those whose velocity is approximately perpendicular to the direction of spin wave propagation (see Chapter 5). This leads to the idea of an 'effective zone' of the Fermi surface consisting of those

electrons which may interact with spin waves. Since the size and shape of the pockets depends on the direction of the magnetization with respect to the crystal axes the electrons comprising the 'effective zone' will differ depending on the direction of the magnetization. The result may be a dependence of the magnetic damping on the direction of the magnetization which would be manifested as an anisotropy of the FMR linewidth.

The Work Reported in this Thesis

This possibility of an anisotropic linewidth at low temperatures has been investigated in two ways. Ferromagnetic resonance was measured in pure Nickel samples with the applied field parallel to each of the three principal crystal axes (100), (111) and (110). The resistivity ratio of the samples was 38 so that we were above the limit of approximately 30 for which the linewidth was found to reach its limiting value[1]. Because the FMR line becomes very broad on cooling, approximately 1600 Oe at 24 GHz at 4.2 K, the signal becomes small and difficult to detect. We were unable to observe FMR using a conventional field modulation technique at temperatures below approximately 60 K. We used a bolometer to detect the absorption at 4.2 K. Our results indicate that the linewidth is anisotropic at low temperatures. For temperatures below approximately 200 K the (110) linewidth is greater than the (100) and (111) linewidths. The (100) and (111) linewidths were

the same for temperatures above 60 K, the lowest temperature at which we could measure FMR using field modulation. This is the same behaviour observed by Anders, Bastian and Biller[17] for temperatures greater than 77 K. At 4.2 K, the only temperature at which the bolometer could be used, we found that the (100) linewidth was 1620±50 Oe, the (111) linewidth was 1820±50 Oe and the (110) linewidth was 2050±50 Oe.

A calculation of the damping parameter has been carried out using a simple model of electrons and spin waves coupled by the spin orbit interaction. We calculated the susceptibility using the method of Green's functions. The imaginary part of this susceptibility was related to the damping parameter. The expression we obtained for the damping parameter reduced to that obtained by Korenman and Prange[3,4] if we assumed a spherical Fermi surface. The integrals over the Fermi surface which enter the damping parameter were evaluated numerically using the description of the X_5 hole pockets of Hodges, Stone and Gold[16]. The results were not in agreement with experiment. The values of the damping parameter were approximately 100 times too small to account for the linewidth in Nickel at 4.2 K. The calculated anisotropy of the damping parameters was also not in agreement with experiment. For example, based on the calculation we expected that the linewidth for the (100) direction should be approximately 4% larger than the linewidth for the (111) direction. From experiment we found that the (111) linewidth was approximately 12% larger than the (100)

linewidth. The implication of these results is that other portions of the Fermi surface must play an important role in the magnetic damping of Nickel at low temperatures.

1.2 Historical Overview

We present a brief historical overview of the experimental work relevant to the work presented in this thesis. Most of the work cited involves measurements of FMR on Nickel at room temperature and below. The order of presentation is as follows: first the most important FMR measurements are mentioned; then a series of measurements relating to the anisotropy of the FMR linewidth of Nickel which are conveniently discussed as a group, although made concurrently with the first set of experiments. As an example of the treatment of the anomalous skin effect in FMR we discuss a measurement on Iron. Finally FMAR measurements of the damping in Nickel are discussed.

FMR in Nickel

Measurements of the properties of ferromagnets at microwave frequencies have been made since the turn of the century. A review of work done before 1950 is given by Rado[18].

The first measurement of FMR was made by Griffiths[19] in 1946 on samples of Nickel, Iron and Cobalt. His samples were thin films (0.025 mm) electrodeposited on a brass disk. The

linewidth for Nickel was approximately 2000 Oe at 9 GHz. This is much larger than the linewidth for a good single crystal of Nickel at this frequency (approximately 100 Oe, see below).

Low temperature measurements were made in 1956 by Reich[20]. The measurements were made on (110) plane single crystal disks at frequencies of 9 and 24 GHz, at 4.2 K, 77 K and room temperature. The 'half-line-width' at 24 GHz was of the order of 350 Oe and independent of temperature. From the resonance field values a value of the g-factor, $g = 2.21 \pm 0.01$, and values for the magnetocrystalline anisotropy constants K1 and K2 were obtained. The values of K1 were -5.4×10^5 and -8.3×10^5 erg/cm^3 at 77 and 4.2 K respectively. These are approximately two-thirds the accepted values of -8.45×10^5 and -12.9×10^5 [21]. The samples had a poor resistivity ratio, $\rho_{295}/\rho_4 = 7$. This low purity explains the temperature independent linewidth and may also account for the discrepancy in the values of the anisotropy constants. Franse [22] has shown that the anisotropy constants of Nickel may be sensitive to impurities.

The first measurements in which the intrinsic linewidth of Nickel was observed, as opposed to that due to the sample quality or surface preparation techniques, were made by Rodbell[23,24] in 1964 on Nickel platelets and whiskers. Platelets and whiskers are small, very perfect, single crystals grown by a vapor reduction process. The virtue of these samples is that the surfaces are smooth and require no polishing or

other preparation. Thus the measurements reflect as closely as possible the ideal behaviour of the material. The samples are small and very fragile and require great care in handling. This point is discussed further below. Rodbell's measurements were made at 9 and 35 GHz at temperatures from 130 K to 635 K (the Curie Temperature of Nickel). At room temperature the 9.2 GHz linewidth was typically 130 Oe. The results were described by a Landau-Lifshitz damping parameter $\lambda = 2.5 \times 10^8$ sec^{-1} independent of temperature and frequency. This parameter varied slightly from sample to sample. A frequency and temperature independent value for g of 2.22±0.03 was found. No spin-pinning was required to match the results. Values for K1 and K2 were deduced over the temperature range. The values of K1 were in agreement with those of other authors. The values of K2 are in agreement if the correction pointed out by Aubert[25] is taken into account. These measurements are probably the only worthwhile FMR results reported on Nickel platelets.

The frequency dependence of the FMR linewidth at room temperature was investigated in 1965 by Frait and MacFaden[26]. Measurements were made on a number of materials including single crystals of pure Nickel. These samples were disks spark cut from a bulk single crystal, mechanically polished, annealed for several hours, then electropolished. The linewidth at 25 GHz was 520 Oe. This is much larger than the intrinsic linewidth of 330 Oe expected at this frequency for a good sample. The frequency dependence for Nickel (8 to 72 GHz) could not be

explained by any macroscopic theory. The large linewidths were ascribed to inhomogeneities and stresses in the sample. The lesson to be drawn from these results is that it is not straightforward to reproduce the linewidth characteristic of the metal in bulk samples. A value of g = 2.21±0.04 was found. Values of K1 and K2 in agreement with accepted values were obtained.

Bhagat, Hirst and Anderson[27] made measurements similar to those of Frait and MacFaden in 1966. Their samples were (110) plane disks and cylinders oriented with the cylinder axis parallel to either the (111) or (100) axis. These samples were spark cut from bulk single crystals and electropolished. The linewidth at a frequency of 21.7 GHz was 300 Oe. From the frequency dependence of the linewidth(9 to 57 GHz) they found the Landau-Lifshitz damping parameter to be $2.3 \times 10^{8} sec^{-1}$. It was found necessary to use a surface anisotropy $K_s = 0.25 erg/cm^3$ with the anisotropy axis parallel to the sample surface to reproduce the experimental results. The value of the g-factor used in the analysis was 2.22.

These measurements were extended to low temperatures by Bhagat and Hirst[1] in 1966, in the first good low temperature measurements on Nickel. Measurements were made over the temperature range 4.2 K to 300 K at 9, 22 and 35 GHz. They found that the linewidth increased on cooling and that the 4.2 K linewidth was independent of the resistivity ratio in samples with resistivity ratios of 30, 60 and 160. The observed

linewidths at 4.2 K were 640 Oe at 9 GHz, 1500 Oe at 22 GHz and 2200 Oe at 34.8 GHz. These linewidths were much larger than could be explained by the exchange conductivity mechanism. The results were interpreted as evidence for a temperature dependence of the damping parameter.

In 1969 Franse[28] made FMR measurements on Nickel in an attempt to measure the magnetocrystalline anisotropy constants. He used (110) plane disks electrically or mechanically polished. The linewidths were quite large, being 600 Oe at room temperature and 1200 Oe at 77 K at a frequency of 23.3 GHz. The values of K1 and K2 deduced from the FMR data at 77 K were in agreement with the values obtained using a torque magnetometer. Franse comments that the accuracy of FMR measurements of the magnetocrystalline anisotropy constants is much smaller than may be obtained from torque experiments. He also states that it is impossible to obtain values for the higher order constants, K3, K4..., using FMR. This is a problem because these higher order constants are important in Nickel at low temperatures.

The connection between the increase in the linewidth at low temperatures and the increase in the conduction electron mean free path was made in 1970 in the experiments of Lloyd and Bhagat[14]. The temperature dependence of the linewidth at 35 GHz was measured using cylindrical samples oriented with a (100) or a (111) axis along the cylinder axis. The samples used were pure Nickel and 0.17% and 5.4% Copper in Nickel alloys. The linewidth of the 0.17% Cu alloy (resistivity ratio of 30) at

4.2 K was approximately 90% that of pure Nickel, while the 5.4% Cu alloy (resistivity ratio of 3) showed no increase in the linewidth with decreasing temperature. A value of $|K1|/M_s$ of 2150 G for Nickel at 4.2 K is quoted. This is based on "the shift in the resonance field as a function of temperature". The currently accepted value of $|K1|/M_s$ is 2460 G (see the discussion of Nickel parameters in Section 4.1). There is a fair discrepancy between these two values. We will discuss our results on the position of FMR in Chapter 4 and argue that this discrepancy is due to the wavenumber dependence of the magnetic damping.

In 1971 Anders, Bastian and Biller[17] made measurements on (110) Nickel disks. The samples were cut from 99% pure Nickel, electropolished and carefully annealed. FMR was measured for different directions of the applied field with respect to the crystal axes in the sample plane. Measurements were made at 9.2, 19.6 and 26.2 GHz. at temperatures between 77 K and 630 K. The linewidth at 26.2 GHz at room temperature was approximately 350 Oe (this value was taken from their Figure 1). They found the Landau-Lifshitz damping parameter to be 2.3×10^8 sec^{-1} independent of temperature and orientation of the applied field for temperatures from 273 to 630 K. Below 273 K they found that the linewidth was anisotropic, with the (110) linewidth being greater than the (100) and (111) linewidths. The difference in the linewidths for the different crystal axes increased with decreasing temperature. From their Figure it appears that the

difference between the (100) and (111) linewidths was not significant. At 77 K, at 26.2 GHz the (110) linewidth was 820 Oe and the (111) linewidth was 640 Oe. A value for the (100) linewidth at this frequency is not quoted.

In 1974 Bhagat and Lubitz[12,13] reported the results of further experiments on Nickel at low temperatures. The experiments were aimed at defining the temperature dependence of the linewidth between 77 K and 4.2 K where the linewidth attains its saturation value. The samples were cylinders with a (111) axis along the cylinder axis. These were electropolished and annealed. Values of the Landau-Lifshitz damping parameter obtained by comparing the experimental data with the calculation of Hirst and Prange[9] which includes a non-local conductivity are quoted. A value of g = 2.22 and a surface anisotropy of 0.1 erg/cm^2 were used in the analysis. It is important to note that in none of the work reported by Bhagat and colleagues is there any mention of an anisotropy in the linewidth at low temperatures. We will come back to this point when we discuss our results in Chapter 4.

Anisotropy of the Linewidth

We discuss now a series of measurements related to the anisotropy of the FMR linewidth. In 1967 Vittoria, Barker and Yelon[29] made measurements on Nickel platelets of the dependence of the FMR linewidth on the direction of the applied

field with respect to the crystal axes. They made measurements by rotating the applied field both in the sample plane and out of the sample plane. Their results were interpreted as evidence that the damping parameter was anisotropic.

In response to these measurements Anderson, Bhagat and Cheng[30] in 1971 reported similar measurements made on single crystal disks cut from a bulk single crystal. Measurements were made on (100) and (110) normal disks at 22 GHz. The linewidth was found to be isotropic for in-plane variations of the direction of the applied field, within the experiemntal uncertainty of ±10 Oe. The linewidth for out of plane variations of the direction of the applied field was anisotropic because of the misalignment obetween the magnetization and the applied field caused by the demagnetizing field. All the results were consistent with an isotropic damping parameter.

Maksymowicz and Leaver[31], also in 1971, made similar measurements on Nickel platelets, both in and out of the sample plane. The dependence of the linewidth on angle was described as 'a sum of a constant term and a term resulting from the Gilbert type equation of motion'. The damping parameter required was isotropic.

In 1972 Bailey and Vittoria[32] reported further measurements on platelets. The measurements were of the in-plane variation of the linewidth at 9.4 GHz at temperatures from 171 to 293 K. The results indicayed that the (100) linewidth was larger than the (110) linewidth at all

temperatures and that the difference between the linewidths for the two directions increased on cooling. The room temperature linewidth was 165 Oe which was larger by approximately 30% than the linewidths found by Rodbell[24] at a similar frequency.

Experiments using Nickel platelets are very difficult because of the extreme fragility of the samples. Almost any handling at all will damage the platelet resulting in broadening of the FMR line. This was demonstrated very clearly by Wu, Quach and Yelon[33] who made measurements on Nickel-Cobalt platelets. Nickel Cobalt platelets are thicker, and hence more robust, than pure Nickel platelets. However even with careful handling of the samples the results showed anomalies which could be explained only as a consequence of damage to the samples due to handling. It appears then that the anisotropy of the linewidth observed by Vittoria et al[29,32] resulted from the use of damaged samples rather than as a result of an anisotropy of the intrinsic damping.

Vittoria et al[34,35] were also responsible for two papers in which the angular variation of the linewidth was calculated. In the second of these papers the claim is made that the combination of exchange and magnetocrystalline anisotropy may produce an anisotropy of the linewidth. This is true if the linewidth is almost entirely due to exchange conductivity broadening and if the conductivity is large. The authors suggest that they performed calculations appropriate for Nickel, however they use a Landau-Lifshitz damping parameter of

0.375×10^8 sec^{-1} which is much smaller than the currently accepted value of 2.45×10^8 sec^{-1}. We have performed calculations in which both exchange and magnetocrystalline anisotropy are included using realistic parameters for Nickel at a temperature corresponding to 77 K with a local conductivity and we find no difference between the calculated linewidths for the (100), (111) or the (110) directions.

The Anomalous Skin Effect

At low temperatures the wavenumber dependence of the conductivity becomes important and must be considered in a calculation carried out for comparison with experiment. A calculation of the FMR absorption with a non-local conductivity was carried out by Hirst and Prange[9]. A computer program based on their calculation was used in the analysis of the data of Bhagat and Hirst[1] and Bhagat and Lubitz[12,13]. The linewidth in Nickel is dominated by the intrinsic damping as stated in Section 1.1. Measurements on Iron whiskers at low temperatures made in 1967 by Bhagat, Anderson and Wu[36] provided a test of the Hirst-Prange theory in a material in which the linewidth is predominantly due to exchange conductivity broadening. The experimental results for Iron were in good agreement with the theory, which predicted that the exchange conductivity broadening should increase much less rapidly with decreasing temperature (increasing conductivity)

than would be expected if a theory using the dc conductivity were used. In addition to broadening the FMR line, exchange conductivity produces a shift in the value of the applied magnetic field at which resonance occurs. Calculated values of this shift as a function of resistivity ratio for Iron are quoted in the paper. Unfortunately the shifts in the resonance field due to magnetocrystalline anisotropy were not known well enough to permit a comparison between the experimental and calculated resonance positions.

FMAR Measurements in Nickel

The microwave permeability is large at FMR with the result that the skin depth is small. As stated above typical wavenumbers at FMR are 10^4-10^5 cm^{-1}. At the value of the applied field corresponding to Ferromagnetic Antiresonance(FMAR, see Chapter 2) the permeability is small so that the skin depth becomes large. Typically wavenumbers at FMAR are 1/20 those at FMR. Measurement of the transmission of microwaves at FMAR through thin samples provides a very sensitive measure of the damping parameter, see for example Cochran and Heinrich[37]. Since this is a transmission technique it is sensitive to the bulk of the sample as opposed to FMR which is sensitive to a surface layer approximately one microwave skin depth thick.

Transmission measurements through polycrystalline Nickel foils by Dewar, Heinrich and Cochran[38] yielded values of

$G = 2.45 \pm .1 \times 10^8$ sec^{-1} for the damping parameter at room temperature and a value of $g = 2.187 \pm .005$ for the g-factor. These may be considered the definitive values for these parameters.

Low temperature measurements were made on single crystal samples by Heinrich, Meredith and Cochran[15] and by Myrtle[39]. The damping parameter was found to increase with decreasing temperature below approximately 250 K. The increase was much more rapid than the increase in the damping parameter found in the FMR measurements of Bhagat and Lubitz[12]. This was interpreted as evidence for the wavenumber dependence of the damping. The temperature dependence of the FMAR damping parameter was described well by the expression:

$$G(T) = a\sigma_0(T)/\sigma_0(295) + b\rho(T)/\rho(295) \qquad (1.8)$$

where σ_0 and ρ are the dc conductivity and resistivity respectively, and a and b were constants chosen to match experiment. The values of a and b which fitted the temperature dependence were $a = 1.07 \times 10^8 sec^{-1}$ and $b = 1.19 \times 10^8 sec^{-1}$. The first of these terms corresponds to the result of Korenman and Prange[3,4] with the substitution $\arctan(ql)/ql \simeq 1$ since the values of q are small at FMAR. The second term corresponds to the result of Elliott[10] and Kambersky[2] for spin-flip scattering.

2. THEORY

2.1 Introduction

Two different problems are of theoretical interest in connection with the work reported in this thesis. First, the phenomenological theory which is used to deduce fundamental magnetic parameters from experiment, and second, the microscopic theory which can be used to calculate a value of the damping parameter, G, from the band structure for comparison with the value of G deduced from the data and the phenomenological theory used to describe FMR absorption. The phenomenological theory is described in this chapter; a discussion of the calculation of the damping parameter is postponed until Chapter 5.

The quantity measured in a ferromagnetic resonance experiment is either the absorbed power as a function of the applied magnetic field, or the derivative of the absorbed power with respect to the field. The resulting curve is described by the resonance field, H_{fmr}, the value of the applied field at which the absorbed power is a maximum, and by the linewidth, ΔH, the field interval between the extrema of the derivative of the absorption with respect to field.

The position and shape of an FMR absorption line depend upon a number of factors. Material parameters include the

saturation magnetization, M_s, the spectroscopic splitting factor, g, magnetocrystalline anisotropy constants, K1, K2, the exchange constant, A, the damping parameter, G, and the electrical conductivity, σ_0. The microwave frequency and the sample shape also play a role. These factors are so entangled in determining the position and linewidth that to extract values for material parameters from an experimental line it is usually necessary to compare the data with an FMR lineshape calculated using a phenomenological theory. Frequency and temperature dependences of the resonance field and linewidth often prove useful in sorting out the various contributions. Care must be taken when fitting the observed lineshapes as these can be easily affected by experimental factors which do not affect H_{fmr} or ΔH. For example the asymmetry of an experimental derivative line, the ratio of the high field derivative peak to the low field derivative peak, often differs from that expected from a calculation while the linewidth and position are close to those expected (see Bhagat, Hirst and Anderson[27]).

Three calculations are described in this chapter. These correspond to the variety of situations with which we are faced experimentally. In the first calculation, Section 2.2, the standard FMR treatment is presented. The applied field is taken to be parallel to the sample plane and also parallel to one of the three principal crystal directions (100), (110), (111). A local electrical conductivity is assumed, ie $\bar{j} = \sigma_0 \bar{e}$, where $\bar{j}$ is the current density, $\bar{e}$ the electric field and σ_0 the dc

conductivity. This calculation is appropriate for temperature regimes where the approximation of a local conductivity is valid. For Nickel this approximation is valid for temperatures above approximately 77 K. The effects of exchange are included. This is the simplest geometry to treat as the magnetization is parallel to the applied field at the fields at which resonance occurs, and it corresponds to the geometry which is used in an experiment.

If the applied field is allowed an arbitrary orientation with respect to the sample plane and the crystal axes, magnetocrystalline anisotropy and demagnetizing effects combine so the static magnetization is not, in general, parallel to the applied field. The angle between the magnetization and the field depends on the magnitude of the field. The magnetization is said to 'drag' behind the field. In an experiment an attempt is made to align the sample such that the external field is applied exactly in the sample plane and exactly parallel to a crystal axis. If these conditions are not met dragging will occur. The observed lines will differ from those expected on the basis of the calculation of Section 2.2. To obtain an idea of the magnitude of the discrepancy introduced by misalignment a calculation is carried out in Section 2.3 which allows for arbitrary orientation of the applied field relative to the sample plane, as well as relative to the crystal axes. A local conductivity is assumed. Exchange is not included as the calculation becomes quite complicated. This is not a major

shortcoming since for Nickel exchange torques are small compared with the damping torque.

At low temperatures (below 77 K) the increase in conduction electron mean free path results in the conductivity and the damping becoming wavenumber (q) dependent. A different approach for a calculation of the absorption is required. These effects are considered in the third calculation, outlined in Section 2.4. The geometry is the same as in the first calculation the applied field being in the plane of the sample and along a principal axis. Exchange is included.

Experimental Geometry

In the experiments reported in this thesis the sample was a Nickel single crystal in the form of a thin disk cut with a (110) axis normal to its plane. The sample formed part of the endwall of a cylindrical microwave cavity. The applied field was oriented parallel to the sample plane (the 'parallel configuration') and could be rotated in that plane. The sample was attached to a demountable endplate so that experiments could be performed for the applied field parallel to the different crystal directions but with the microwave magnetic field maintained perpendicular to the static magnetic field.

For the calculations outlined in this chapter the geometry of Figure 2.1 is assumed. The sample forms an infinite slab lying in the x-y plane, with the sample normal along $[1\bar{1}0]$: in

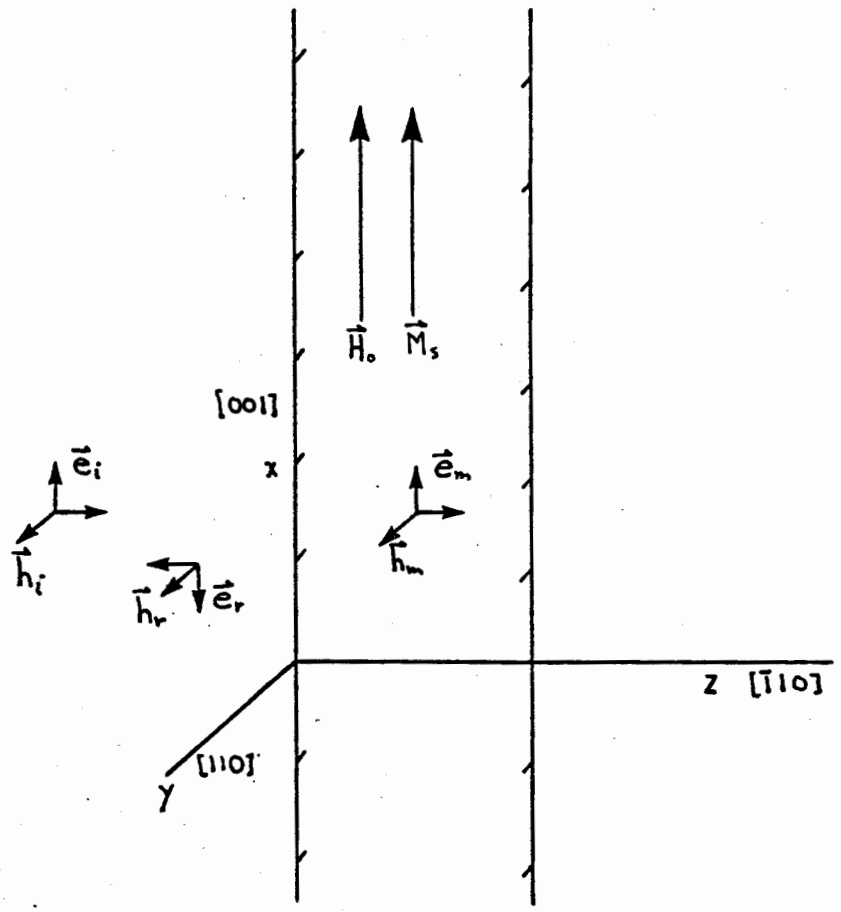

Figure 2.1 The geometry used for the calculation of the absorption. The sample lies in the x-y plane. The geometry shown is for a calculation with the applied field parallel to the [001] axis. The sample may be rotated about the z-axis so that the [111] or the [110] axes can be oriented parallel to the x-axis.

consequence the [001], [110] and [111] directions lie in the sample plane (see Figure 2.2). For the first and third calculations (Sections 2.2 and 2.4) the applied field points along the x-direction and the crystal is oriented with a principal axis in the x-direction.

Linearly polarized microwaves, with the microwave magnetic field along the y-direction, propagate in the z-direction and are incident on the sample at z = 0. The slab thickness is much larger than the microwave skin depth so the sample may be treated as semi-infinite. The slab is taken to be in free space. It can be shown (see, for example, Urquhart[40]) that the results for the calculation with boundary conditions corresponding to a sample in a cavity differ only by a scaling factor from those of the free space calculation.

2.2 Calculation of the Absorption

This calculation breaks into two distinct pieces. First the microwave permeability is found by solving the Landau-Lifshitz equation. This permeability is then combined with Maxwell's equations to solve the boundary value problem of reflection from the metal surface yielding the absorbed power as a function of applied field.

The Landau-Lifshitz equation (often termed the equation of motion) is simply the statement that the rate of change of angular momentum is equal to the torque. The Landau-Lifshitz

equation may be written:

$$-1/\gamma \, \partial\bar{M}/\partial t = \Sigma \, \bar{\tau} \qquad (2.1)$$

where $\bar{M}$ is the magnetic moment per unit volume, $\gamma = g|e|/2mc = (g/2)(1.7588 \times 10^7 \text{ Oe}^{-1} \text{ sec}^{-1})$ is the gyromagnetic ratio, (the ratio of magnetic moment to angular momentum for an electron), the g-factor for Nickel is $g = 2.187 \pm .005$[38], and $\bar{\tau}$ represents the torques acting on the magnetization.

In equilibrium the magnetization is parallel to the applied field. Only small deviations from equilibrium will be considered and therefore the magnetization can be written:

$$\bar{M} = \bar{M}_s + \bar{m}(\bar{r},t) \qquad (2.2)$$

where $\bar{M}_s$ is the saturation magnetization (parallel to the applied field) and $\bar{m}(\bar{r},t)$ is the deviation of $\bar{M}$ from $\bar{M}_s$. The magnitude of $\bar{m}$ is taken to be much less than M_s. All quantities are assumed to vary in the z-direction only, with a time and space dependence $\exp(i(kz-wt))$ so $\bar{m}(\bar{r},t) = \bar{m} \exp(i(kz-\omega t))$.

The torques acting on the magnetization are due to (i) static and microwave applied fields; (ii) demagnetizing fields; (iii) magnetocrystalline anisotropy; (iv) exchange; (v) magnetostriction; and (vi) damping. These are discussed individually below.

The concept of an 'effective field' proves important in what follows to describe the torques acting on the magnetization. A brief discussion is given here. For more detail the reader is referred to 'Micromagnetics' by W.F. Brown[41].

Three components are required to define the vector $\bar{M}$. These may be the components in a rectangular coordinate system (M_x,M_y,M_z), or the components in a spherical-polar coordinate system (M,θ,ϕ) where M is the magnitude of $\bar{M}$, θ and ϕ are the polar and azimuthal angles respectively. The magnitude of the magnetization is fixed, $M = M_s$, so only the angles are independent. If the energy of the system, magnetization and surroundings, is written $E(\theta,\phi)$ the components of the torque on the magnetization are $-\partial E/\partial\theta$ and $-\partial E/\partial\phi$. It is usually more convenient to work with the components (M_x,M_y,M_z). The vector $\bar{H} = -\partial E/\partial\bar{M}$ may be regarded as an 'effective field' and the torque found from $\bar{\tau} = \bar{M} \times \bar{H}$. The energy may be written $E(M_x,M_y,M_z)$ or, taking into account the constraint on the length of $\bar{M}$, $E(M_x,M_y,\sqrt{M_s^2-(M_x^2+M_y^2)})$. The effective fields obtained from these two ways of writing the energy will be different, however the torques will be the same.

A simple example might be useful. Consider an applied magnetic field along the z-axis. The energy is $E = -\bar{M}\cdot\bar{H}_0$. Let $E_1 = -M_zH_0$ and $E_2 = -(\sqrt{M_s^2-(M_x^2+M_y^2)})H_0$. These expressions are equivalent. The effective fields $\bar{H} = -\partial E/\partial\bar{M}$ are:

$$\bar{H}_1 = (0,0,H_o)$$

$$\bar{H}_2 = (-M_x,-M_y,0)\ H_o/\sqrt{M_s^2-(M_x^2+M_y^2)}$$

Although these look very different it is easy to verify that they yield the same torque:

$$\bar{\tau} = (M_y,-M_x,0)\ H_o$$

Throughout this thesis energies will be written as $E(M_x,M_y,M_z)$ rather than explicitly taking into account the constraint on the length of the magnetization.

Applied Fields

The torque due to the applied fields is:

$$\bar{\tau} = \bar{M} \times (\bar{H}_o + \bar{h}(\bar{r},t)) \qquad (2.3)$$

where $\bar{H}_o$ is the static applied field and $\bar{h}(\bar{r},t)$ the microwave field. The magnitude of the microwave field is much less than H_o.

Demagnetizing Field

The torque due to the demagnetizing effects is written in terms of an effective demagnetizing field H_d:

$$\bar{\tau} = \bar{M} \times \bar{H}_d \tag{2.4}$$

In the special case of a uniformly magnetized ellipsoidal sample the demagnetizing field is uniform and may be written in terms of the demagnetizing tensor $\mathbb{D}$:

$$\bar{H}_d = -4\pi \mathbb{D} \cdot \bar{M}$$

The components of $\mathbb{D}$ are the demagnetizing factors for the three principal axes of the ellipsoid. A thin disk may be treated as the limiting case of an ellipsoid, with a demagnetizing factor $D_{\parallel}$ if the magnetization is in the plane of the disk, and $D_{\perp}$ if the magnetization is perpendicular to the sample plane. If the ratio of the sample thickness to diameter is small $D_{\parallel}$ will be small and $D_{\perp}$ approximately 1. For an infinite slab $D_{\parallel} = 0$. Kraus and Frait[42] give an empirical expression for the demagnetizing field at the center of a disk when the magnetization is in the sample plane:

$$H_d = 2\pi M_s R(\sqrt{(1 + 4R)} + 0.366 M_s/H_o) \tag{2.5}$$

where R is the thickness to diameter ratio. For the samples used in the present work R was approximately 10^{-2}, $2\pi M_s$ = 3.2 kOe and $M_s/H_0<0.4$ at the fields of interest, so the demagnetizing field was of the order of 30 Oe. This field is included in the calculation by replacing H_0 by H_0+H_d, H_d points in the opposite direction to H_0 of course. For the rest of this chapter this in plane demagnetizing field will be ignored. In the general case where the magnetization may point out of the sample plane the z-component of the demagnetizing field is $-4\pi M_z$ where M_z is the component of $\bar{M}_s$ normal to the sample plane. An important point is that only the demagnetizing field due to the static magnetization is considered here. The microwave demagnetizing effects are taken into account by means of Maxwell's equations.

Magnetocrystalline Anisotropy

As a result of spin-orbit coupling the energy of a ferromagnet depends on the direction of the magnetization with respect to the crystal axes. This energy is called the magnetocrystalline anisotropy energy. The term 'magnetocrystalline anisotropy' will recur many times in this thesis so it will be abbreviated as 'MCA'. MCA is often referred to as, simply, the anisotropy. It is thought that this usage could lead to confusion with the sought after anisotropy of the FMR linewidth, hence the abbreviation.

MCA is important in this work for a number of reasons. The large torque arising from MCA introduces experimental problems in mounting the samples; they tend to rotate unless H_0 is accurately aligned with a principal axis. The dragging of the magnetization due to MCA can lead to problems of analysing the data. Both MCA and magnetic damping are a consequence of spin-orbit coupling. The observation of Furey (quoted by a number of authors, see for example Kambersky [2] or Franse [22]) that a large part of the MCA of Nickel arises from the electron states around the X_5 hole pockets played a part in focussing the attention of workers interested in magnetic damping on those parts of the Fermi surface.

The standard method of treating MCA is to write the part of the free energy per unit volume of the sample which depends on the orientation of the magnetization as a series in the direction cosines of the magnetization with respect to the cubic crystal axes:

$$E_{AN} = K1S + K2P + K3S^2 + \ldots \qquad (2.6)$$

where K1, K2, K3 ... are the magnetocrystalline anisotropy constants, $S = a_1^2a_2^2 + a_2^2a_3^2 + a_3^2a_1^2$ and $P = a_1^2a_2^2a_3^2$, and a_1, a_2, a_3 are the direction cosines. Any combination of the direction cosines which has the necessary cubic symmetry can be written in terms of S and P (see for example Aubert et al[43]).

MCA in Nickel at room temperature is well described by the first two terms in this series, however the description becomes more complicated at low temperatures where four anisotropy constants are required plus two additional constants which are not part of the series (2.6) (Gersdorf[44]). This will be discussed further in chapter 4. For the calculations in this chapter the series (2.6) with K1, K2 and K3 will be used.

In Nickel K1 is negative so the MCA energy is a minimum if the magnetization points along a (111) direction (the 'easy axis'), and a maximum if the magnetization points along a (100) direction (the 'hard axis'). There is a saddle point in the energy about the (110) directions. The MCA torque on the magnetization is zero for these three directions. If the magnetization lies in either a (100) or (110) normal crystal plane there is an in plane torque but there is no MCA torque tending to rotate the magnetization out of that plane.

The torque on the magnetization is written in terms of the effective field $\bar{H}_{AN}$:

$$\bar{\tau} = \bar{M} \times \bar{H}_{AN} \qquad (2.7)$$

With $\bar{M}_S$ along the [001] direction, as in figure 2.1, the direction cosines are (see Figure 2.3):

$$a_1 = (M_y - M_z)/(\sqrt{2})M_S$$

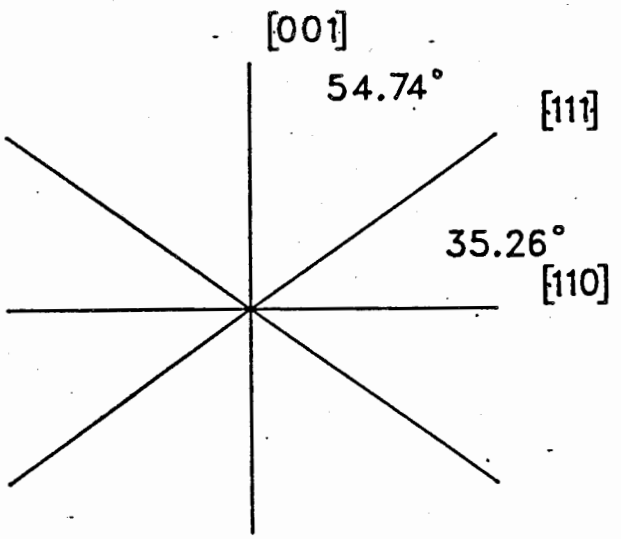

Figure 2.2 The crystal axes in the [1$\bar{1}$0] plane.

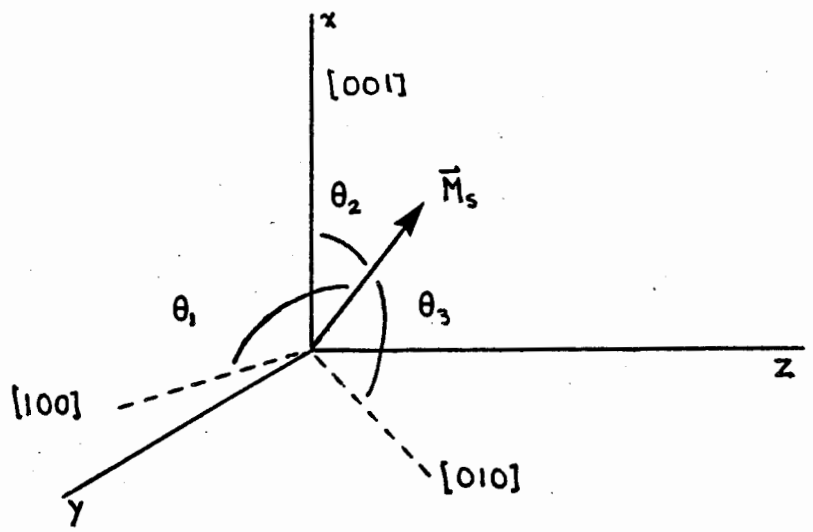

Figure 2.3 The angles used in determining the effective MCA fields. The [100] and [010] axes are in the y-z plane. The direction cosines are: $a_1 = \cos(\theta_1) = (1/\sqrt{2}M_s)(M_y - M_z)$;

$a_2 = \cos(\theta_2) = (1/\sqrt{2}M_s)(M_y + M_z)$;

$a_3 = \cos(\theta_3) = M_x/M_s$.

$$a_2 = (M_y+M_z)/(\sqrt{2})M_s$$

$$a_3 = M_x/M_s$$

Recall that the sample normal is along $[1\bar{1}0]$. The polynomials S and P are:

$$S = [4M_x^2(M_y^2+M_z^2) + (M_y^4-2M_y^2M_z^2+M_z^4)]/4M_s^4$$

$$P = [M_x^2(M_y^4-2M_y^2M_z^2+M_z^4)]/4M_s^6$$

We are interested in the case where M_y and M_z are small, $M_y = m_y$, $M_z = m_z$ and $M_x \simeq M_s$. Keeping only terms of first order in m_y and m_z the components of the effective MCA field are:

$$H_{ANx} = 0$$

$$H_{ANy} = (-2K1/M_s)m_y/M_s$$

$$H_{ANz} = (-2K1/M_s)m_z/M_s$$

Note that using this method to calculate the effective field there is no component of $\bar{H}_{AN}$ in the direction of $\bar{M}_s$. The non-zero components of $\bar{H}_{AN}$ are proportional to the deviation of the magnetization from equilibrium, and in equilibrium (m_y=0, m_z=0) $\bar{H}_{AN} = 0$.

The effective MCA field when $\bar{M}_s$ is parallel to the [110] or [111] directions is found in a similar manner. If $\bar{H}_{AN}$ is written:

$$\bar{H}_{AN} = (0, -\alpha m_y/M_s, -\gamma m_z/M_s) \tag{2.8}$$

then the coefficients α and γ are as listed in Table 2-1. This notation is that used by Cochran and Heinrich[37], this γ should not be confused with the gyromagnetic ratio. Note that α and γ are equal when $\bar{M}_s$ is parallel to a (100) or a (111) direction but differ when $\bar{M}_s$ is parallel to a (110) direction.

Exchange

The exchange interaction leads to an energy which depends on the angle between electron spins. This interaction is responsible for ferromagnetism and in a ferromagnet this energy is a minimum if all of the spins are parallel, or, equivalently, if the magnetization is uniform in space. Any non-uniformity of the magnetization increases the exchange energy.

An expression for this energy increase may be found from symmetry arguments (see Turov[45]). For example, the energy expression must have the symmetry of the crystal lattice and must be invariant on replacing $\bar{M}$ by $-\bar{M}$. The most general expression involving ∇M_x, ∇M_y and ∇M_z which does not depend on

TABLE 2-1

Orientation of $\bar{M}_s$	a	γ
[001]	$2K1/M_s$	$2K1/M_s$
[111]	$-4/3(K1/M_s+K2/3M_s+2K3/3M_s)$	$-4/3(K1/M_s+K2/3M_s+2K3/3M_s)$
[110]	$K1/M_s+K2/2M_s+K3/2M_s$	$-(2K1/M_s+K3/M_s)$

the direction of $\bar{M}$ or the direction of the gradients of the components of $\bar{M}$ is, to second order in $\bar{M}$ and ∇:

$$E_{exc} = (A/M_s^2)((\nabla M_x)^2+(\nabla M_y)^2+(\nabla M_z)^2)$$

where A is the exchange constant, A = 1×10^{-6} erg/cm in Nickel, see Table 4-1. It can be shown[41] that the effective exchange field is:

$$\bar{H}_{exc} = 2(A/M_s^2)(\nabla^2 M_x, \nabla^2 M_y, \nabla^2 M_z)$$

With a spatial dependence of $\exp(ikz)$ this expression becomes:

$$\bar{H}_{exc} = -(2Ak^2/M_s^2)\bar{m}(\bar{r},t) \qquad (2.9)$$

The exchange torque may be important in ferromagnetic metals because the limited penetration of microwaves leads to a

spatial variation of the magnetization. The magnitude of the exchange field is discussed below. It is a small effect in Nickel.

Magnetostriction

If the sample is strained in any way there is a torque on the magnetization due to magnetostriction. The sample may be strained during preparation, for example, by mechanical polishing followed by inadequate electropolishing, or it may be strained during an experiment by the mounting used to hold the sample. If the sample is soldered to a diaphragm of a different metal the differential thermal contraction on cooling may lead to strain. A uniform stress shifts the position of the resonance; shifts up to 100 Oe can easily be produced (Cochran and Heinrich[37]). A non-uniform stress broadens the resonance as different parts of the sample resonate at different values of the applied field. Care was taken to avoid straining the samples in the present experiments and therefore magnetostriction is not included in the calculation of linewidths and line positions. The effect of a uniform stress on the field at which FMR occurs is discussed by MacDonald[46].

Damping

Magnetic relaxation processes are included in a calculation of FMR by introducing a damping torque. Two forms for this damping torque are in common use, the Gilbert form:

$$\bar{\tau} = -(G/\gamma^2 M_S^2)(\bar{M} \times \partial\bar{M}/\partial t) \qquad (2.10)$$

where G is the Gilbert damping parameter, and the Landau-Lifshitz form:

$$\bar{\tau} = (\lambda/\gamma M_S^2)(\bar{M} \times (\bar{M} \times \bar{H})) \qquad (2.11)$$

where λ is the Landau-Lifshitz damping parameter. The field entering the Landau-Lifshitz form is the effective field, including the applied, demagnetizing, MCA and exchange fields. In both forms $\partial\bar{M}/\partial t$ is perpendicular to $\bar{M}$, that is the length of the magnetization remains constant during relaxation back to equilibrium. It can be demonstrated (see for example Baartman[47]) that the two forms are equivalent but that the values of the damping parameter and the gyromagnetic ratio deduced from experimental data will be slightly different depending on whether the Gilbert or the Landau-Lifshitz form is used in the analysis of the data. If G and γ are values appropriate for Gilbert damping, the corresponding parameters

for Landau-Lifshitz damping are:

$$\lambda = G/(1 + (G/\gamma M_s)^2)$$

$$\gamma_{LL} = \gamma/(1 + (G/\gamma M_s)^2)$$

For light damping, $(G/\gamma M_s) << 1$, the two forms are equivalent and the parameters have the same values. In Nickel $G/\gamma M_s = 0.026$ at room temperature and is of the order of 0.15 at 4.2 K (based on the value of G required to reproduce the experimental linewidth assuming a wavenumber independent damping). Thus there is no essential difference between the two forms of damping for Nickel in the temperature regions in which we are interested. The Gilbert form will be used in this work.

Calculation of the Permeability

Gathering these effective fields (2.3, 2.8, 2.9) into the Landau-Lifshitz equation and using the Gilbert form for the damping torque we have:

$$-\frac{1}{\gamma}\frac{\partial \bar{M}}{\partial t} = \bar{M} \times (\bar{H}_{eff} + \bar{h}(\bar{r},t)) - \frac{G}{\gamma^2 M_s^2} \bar{M} \times \frac{\partial \bar{M}}{\partial t} \qquad (2.12)$$

where $\bar{H}_{eff} = \bar{H}_o + \bar{H}_{AN} + \bar{H}_{exc}$. Recall that $\bar{M} = \bar{M}_s + \bar{m}(\bar{r},t)$. $\bar{M}_s$ is parallel to the x-axis, the z-axis points into the slab, parallel to the sample normal. $\bar{m}$ and $\bar{h}$ are assumed to vary as

$\exp(i(kz-\omega t))$ and are considered to be small so that quantities second order in m and h may be neglected. Writing out the three equations (2.12):

$$m_x = 0$$

$$(H_o+a+\frac{2A}{M_s}k^2-i\frac{\omega\ G}{\gamma\gamma M_s})m_y + i\frac{\omega}{\gamma}m_z = M_s h_y \qquad (2.13)$$

$$-i\frac{\omega}{\gamma}m_y + (H_o+\gamma+\frac{2A}{M_s}k^2-i\frac{\omega\ G}{\gamma\gamma M_s})m_z = M_s h_z$$

Solving for $\bar{m}$ in terms of $\bar{h}$ gives the susceptibility tensor $\tilde{\chi}$, where $\bar{m} = \tilde{\chi}\cdot\bar{h}$ or:

$$\begin{bmatrix} m_x \\ m_y \\ m_z \end{bmatrix} = \frac{M_s}{H_y H_z-(\omega/\gamma)^2}\begin{bmatrix} 0 & 0 & 0 \\ 0 & H_z & -i\frac{\omega}{\gamma} \\ 0 & i\frac{\omega}{\gamma} & H_y \end{bmatrix}\begin{bmatrix} h_x \\ h_y \\ h_z \end{bmatrix} \qquad (2.14)$$

where:

$$H_y = H_o + a + 2Ak^2/M_s - i(\omega/\gamma)G/\gamma M_s \qquad (2.15)$$

$$H_z = H_o + \gamma + 2Ak^2/M_s - i(\omega/\gamma)G/\gamma M_s$$

It is interesting to note that the damping torque appears in the magnetic field term for Gilbert damping. Had we used the Landau-Lifshitz form for the damping torque the second and third equations of (2.13) would have read:

$$(H_o+a+\frac{2A}{M_s}k^2)m_y + (i\frac{\omega}{\gamma}-\frac{\lambda}{\gamma M_s}(H_o+\gamma+\frac{2A}{M_s}k^2))m_z = M_s(h_y-\frac{\lambda}{\gamma M_s}h_z) \quad (2.16)$$

$$-(i\frac{\omega}{\gamma}-\frac{\lambda}{\gamma M_s}(H_o+a+\frac{2A}{M_s}k^2))m_y + (H_o+\gamma+\frac{2A}{M_s}k^2)m_z = M_s(h_z+\frac{\lambda}{\gamma M_s}h_y)$$

The damping enters the susceptibility through the frequency.

The microwave demagnetizing field, due to m_z, may now be included. Since $\nabla\cdot\mathbf{B} = 0$ from Maxwell's equations, we have $b_z = h_z + 4\pi m_z = 0$ or $h_z = -4\pi m_z$. Combining this with equations (2.13) we may solve for m_y, m_z, and h_z in terms of h_y, the quantity which will be related to the applied microwave field.

$$m_y/h_y = M_s B_z/(H_y B_z - (\omega/\gamma)^2)$$

$$m_z/h_y = i(\omega/\gamma)M_s/(H_y B_z - (\omega/\gamma)^2) \quad (2.17)$$

$$m_z/m_y = i(\omega/\gamma)/B_z$$

$$h_z/h_y = -i(\omega/\gamma)4\pi M_s/(H_y B_z - (\omega/\gamma)^2)$$

with $B_y = H_y + 4\pi M_s$, $B_z = H_z + 4\pi M_s$ and H_y and H_z are given by equation (2.15). The ratio m_y/h_y defines what will be called the effective susceptibility χ. This is NOT a component of the susceptibility tensor. The ratio m_z/m_y indicates the degree of ellipticity of the precession of the magnetization.

The ratio b_y/h_y is given by the effective permeability $\mu = 1 + 4\pi\chi$:

$$\mu = \frac{B_y B_z - (\omega/\gamma)^2}{H_y B_z - (\omega/\gamma)^2} \tag{2.18}$$

$$= \frac{(B_0+a+\frac{2A}{M_s}k^2-i\frac{\omega\ G}{\gamma\gamma M_s})(B_0+\gamma+\frac{2A}{M_s}k^2-i\frac{\omega\ G}{\gamma\gamma M_s})-(\frac{\omega}{\gamma})^2}{(H_0+a+\frac{2A}{M_s}k^2-i\frac{\omega\ G}{\gamma\gamma M_s})(B_0+\gamma+\frac{2A}{M_s}k^2-i\frac{\omega\ G}{\gamma\gamma M_s})-(\frac{\omega}{\gamma})^2}$$

where $B_0 = H_0 + 4\pi M_s$. Ignoring MCA, exchange and damping the permeability becomes:

$$\mu = (B_0^2-(\omega/\gamma)^2)/(B_0H_0 -(\omega/\gamma)^2) \tag{2.19}$$

There are two interesting values of magnetic field in this expression. When $B_0 = (\omega/\gamma)$, that is $H_0 = (\omega/\gamma) - 4\pi M_s$, the permeability vanishes, the microwave Б field is zero. This condition corresponds to ferromagnetic anti-resonance (FMAR). When $B_0H_0 = (\omega/\gamma)^2$ the denominator vanishes and the permeability becomes very large. This condition is ferromagnetic resonance.

The effective permeability contains all the information required for this calculation. However when we consider dragging of the magnetization in Section 2.3 it will be impossible to define a single quantity analogous to the effective permeability. It will be necessary to work with the permeability tensor. For comparison with the calculation of Section 2.3 it is useful to write out the permeability tensor

$\tilde{\mu} = \tilde{1} + 4\pi\tilde{\chi}$ or:

$$\tilde{\mu} = \frac{1}{H_y H_z - (\omega/\gamma)^2} \begin{bmatrix} 0 & 0 & 0 \\ 0 & H_y H_z - (\omega/\gamma)^2 & -i\frac{\omega}{\gamma}4\pi M_s \\ 0 & i\frac{\omega}{\gamma}4\pi M_s & B_z H_y - (\omega/\gamma)^2 \end{bmatrix} \tag{2.20}$$

Maxwell's Equations

We now have the microwave permeability of the magnetic metal. This permeability is available in two forms, the permeability tensor (2.20) in which the microwave demagnetizing field has not been included, and the scalar permeability (2.18) which relates b_y to h_y with the microwave demagnetizing field explicitly taken into account. The problem now is to combine the permeability (either (2.20) or (2.18)) with Maxwell's equations to solve the boundary value problem of the reflection of microwaves from the metal surface. Maxwell's equations are, in CGS units:

$$\nabla \times \bar{e} = -(1/c)\partial\bar{B}/\partial t$$

$$\nabla \times \bar{h} = (4\pi/c)\bar{j} + (1/c)\partial\bar{d}/\partial t \tag{2.21}$$

$$\nabla\cdot\bar{d} = 4\pi\rho$$

$$\nabla \cdot \mathbf{B} = 0$$

In this section we treat the case where the conduction electron mean free path is much smaller than the microwave skin depth. Ohm's law is valid so that the current density $\vec{j}$ is related to the electric field $\vec{e}$ by:

$$\vec{j}(\vec{r},t) = \sigma_0 \vec{e}(\vec{r},t) \qquad (2.22)$$

where σ_0 is the dc conductivity. With the space and time variation $\exp(i(\vec{k}\cdot\vec{r}-\omega t))$ the two curl equations become:

$$i\vec{k} \times \vec{e} = i(\omega/c)\,\mathbf{B} = i(\omega/c)\tilde{\mu}\cdot\vec{h} \qquad (2.23)$$
$$i\vec{k} \times \vec{h} = [(4\pi\sigma_0/c) - i(\omega\epsilon/c)]\vec{e}$$

where ϵ is the dielectric constant of the metal. The displacement current term in Ampere's law, $i(\omega\epsilon/c)\vec{e}$, may be neglected at microwave frequencies. For metals σ_0 is typically 10^{17} sec^{-1} and ϵ is of order 1 so that for $\omega \simeq 10^{11}$ sec^{-1}, $4\pi\sigma_0 >> \omega\epsilon$. For propagation along the z-direction ($\vec{k} = k\hat{z}$) these equations become:

$$ik\begin{bmatrix}-e_y\\ e_x\\ 0\end{bmatrix} = i\omega/c\begin{bmatrix}b_x\\ b_y\\ b_z\end{bmatrix} = i\omega/c\begin{bmatrix}\mu_{xx} & \mu_{xy} & \mu_{xz}\\ \mu_{yx} & \mu_{yy} & \mu_{yz}\\ \mu_{zx} & \mu_{zy} & \mu_{zz}\end{bmatrix}\begin{bmatrix}h_x\\ h_y\\ h_z\end{bmatrix} \tag{2.24}$$

$$ik\begin{bmatrix}-h_y\\ h_x\\ 0\end{bmatrix} = 4\pi\sigma_o/c\begin{bmatrix}e_x\\ e_y\\ e_z\end{bmatrix} \tag{2.25}$$

The microwave demagnetizing condition, $b_z = 0$, is included automatically in the third of equations (2.24). Eliminating the electric field leaves the three equations:

$$\begin{bmatrix}b_x\\ b_y\\ b_z\end{bmatrix} = -ic^2k^2/4\pi\sigma_o\omega\begin{bmatrix}h_x\\ h_y\\ 0\end{bmatrix} \tag{2.26}$$

from which one gets the equations:

$$\begin{bmatrix} [\mu_{xx}+i k^2\delta^2/2]\mu_{xy} & \mu_{xz} \\ \mu_{yx} & [\mu_{yy}+i k^2\delta^2/2]\mu_{yz} \\ \mu_{zx} & \mu_{zy} \quad \mu_{zz} \end{bmatrix} \begin{bmatrix} h_x \\ h_y \\ h_z \end{bmatrix} = \begin{bmatrix} 0 \\ 0 \\ 0 \end{bmatrix} \qquad (2.27)$$

where $\delta^2 = c^2/2\pi\sigma_0\omega$, δ is the skin depth for a permeability $\mu = 1$. This homogeneous system of equations has a solution only if the determinant of the coefficients is zero. The condition that the determinant of the coefficients equal zero determines the values of the wavevector k of the microwave fields in the metal.

For the case we are considering it is not necessary to work with this tensor representation. From (2.20) and (2.26) we have:

$$b_x = h_x \qquad (2.28a)$$

$$b_x = -i k^2\delta^2/2 \; h_x$$

so that:

$$-i k^2\delta^2/2 = 1 \qquad (2.28b)$$

From (2.18) and (2.26) we have:

$$b_y = \mu h_y \qquad (2.29a)$$

$$b_y = -i k^2\delta^2/2 \; h_y$$

so that:

$$-i k^2 \delta^2/2 = \mu \qquad (2.29b)$$

Consider first the situation with no exchange (A = 0). The permeability is then independent of k^2 and there are two solutions for k^2:

$$k^2 = 2i/\delta^2 \qquad (2.30)$$
$$k^2 = 2i\mu/\delta^2$$

These correspond to four waves which can propagate in the metal, two of which propagate in the +z direction and two of which propagate in the -z direction. Only the waves travelling in the +z direction will be considered here because we deal only with the case where the slab thickness is much greater than the skin depth.

The wave described by $k = \sqrt{2i\mu}/\delta$ corresponds to the result expected for a non-magnetic metal. This wave is linearly polarized with its $\bar{h}$ field parallel to M_s (the x-direction). The wave described by $k = \sqrt{2i\mu}/\delta$ is the interesting one, as the wavevector exhibits the resonant behaviour of the permeability. The microwave $\bar{h}$ field is perpendicular to $\bar{M}_s$ and has both y and z components. The $\bar{h}$ vector traces out an elliptical path in the opposite sense to the precessing components of the magnetization, so that $h_z = -4\pi m_z$. The ratio h_z/h_y was given above in equation (2.18). The electric field $\bar{e}$ has only x components and the $\bar{b}$ field has only y components as expected.

If exchange is included in the calculation the permeability depends on k^2 and the relation $\mu + ik^2\delta^2 = 0$ becomes a cubic equation in k^2:

$$\frac{i\delta^2}{2}\left(\frac{2A}{M_s}\right)^2(k^2)^3 + \frac{2A}{M_s}\left[\frac{i\delta^2}{2}(B_z' + H_y') + \frac{2A}{M_s}\right](k^2)^2 \qquad (2.31)$$
$$+ \left[\frac{i\delta^2}{2}(H_y'B_z' - (\omega/\gamma)^2) + \frac{2A}{M_s}(B_y' + B_z')\right]k^2$$
$$+ [B_y'B_z' - (\omega/\gamma)^2] = 0$$

where $H_y' = H_0+a-i(\omega/\gamma)(G/\gamma M_s)$, $H_z' = H_0+\gamma-i(\omega/\gamma)(G/\gamma M_s)$ and $B' = H' + 4\pi M_s$. There are four values of k^2 and eight waves which can propagate in the metal. Consider only those waves which propagate in the +z direction. One value of k is $k = \sqrt{2i}/\delta$ and corresponds to the non-magnetic wave as above. The other three waves have their $\bar{h}$ fields perpendicular to M_s. For values of the applied magnetic field far from the resonance field value these three waves can be categorized as one having primarily electromagnetic character, corresponding to the no-exchange wave, and two which are primarily of spin-wave character. Near FMR it is not possible to make this distinction. For a detailed discussion of the nature of these waves see Cochran et al[48].

The Boundary Value Problem

Having found the wavevectors, k, of the waves in the metal, the boundary value problem may now be solved. As a reminder, the geometry and field amplitudes are indicated in Figure 2.4. Microwaves are incident normally on the surface of a metal slab, the incoming microwaves, e_i, h_i, being linearly polarized with the $\bar{e}$ field along the x direction, parallel to the applied field $\bar{H}_o$ and the magnetization $\bar{M}_s$, and the $\bar{h}$ field along the y direction. We wish to determine the reflected field amplitudes, e_r, h_r, and e_m, h_m, the field amplitudes transmitted into the metal, as well as the reflected and the absorbed power.

The fields $\bar{e}$ and $\bar{h}$ must satisfy the boundary condition that their tangential components be continuous across the interface. As an example consider the case with no exchange. With the microwaves incident as in Figure 2.4 only the resonant wave is excited in the metal. The boundary conditions are:

$$e_{ix} + e_{rx} = e_{mx} \qquad (2.32)$$

$$h_{iy} + h_{ry} = h_{my}$$

From Maxwell's equations, in the vacuum:

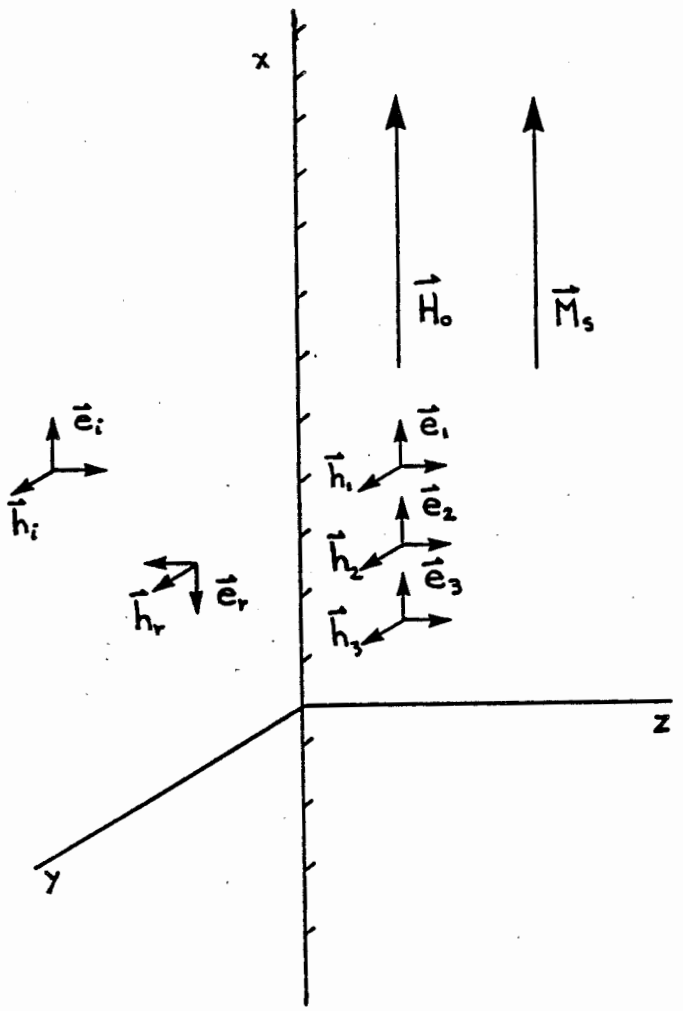

Figure 2.4 Geometry for the boundary value problem.

$$e_{ix} = h_{iy} \qquad (2.33a)$$

$$e_{rx} = -h_{ry}$$

and in the metal:

$$e_{mx} = Z_s h_{my} \qquad (2.33b)$$

where:

$$Z_s = -i\omega\delta^2 k/2c \qquad (2.34)$$

$$= (\omega\delta/2c)\sqrt{-2i\mu}$$

Z_s is the surface impedance of the metal, and the second equality follows from equation (2.30). For a non-magnetic metal having a conductivity equal to that of Nickel at room temperature ($\rho = 7.2\text{x}10^{-6}$ Ωcm, $\sigma_0 = 1.25 \times 10^{17}$ sec^{-1}, see Table 4-1) and a microwave frequency of 24 GHz, one obtains $Z_s \simeq 2.2\text{x}10^{-4}(1 - i)$.

Solving equations (2.32) for h_r and h_m we find:

$$h_{ry}/h_{iy} = (1-Z_s)/(1+Z_s) \qquad (2.35)$$

$$h_{my}/h_{iy} = 2/(1+Z_s)$$

The reflected power, P_r, is found using the Poynting vector

(Jackson[49]):

$$\bar{S} = (c/8\pi)\ \mathrm{Real}(\bar{e} \times \bar{h}^*)$$

Since $\bar{e}$ is perpendicular to $\bar{h}$ and $e_{rx} = -h_{ry}$ the reflected power is proportional to $|h_{ry}|^2$. The ratio of the reflected power to the incident power, P_i, is:

$$P_r/P_i = |h_{ry}/h_{iy}|^2 \qquad (2.36)$$
$$= |(1-Z_s)/(1+Z_s)|^2$$

The absorbed power, P_a, is the incident power less the reflected power:

$$P_a/P_i = 1 - |(1-Z_s)/(1+Z_s)|^2 \qquad (2.37)$$

Writing $Z_s = r + ix$ where both r and x are small, and ignoring quantities of second order:

$$|(1-Z_s)/(1+Z_s)|^2 = ((1-r)^2+x^2)/\ ((1+r)^2+x^2)$$
$$\simeq (1-2r)/(1+2r)$$
$$\simeq (1-4r)$$

Therefore, for small Z_s (the usual situation):

$$P_a/P_i \simeq 4 \times \text{Real}(Z_s) \tag{2.38}$$

From (2.38) and the definition of Z_s, the absorbed power is proportional to the real part of $\sqrt{-i\mu}$.

Returning to the case in which exchange is included, three magnetic waves will be excited. We have two boundary conditions for the tangential components of $\bar{e}$ and $\bar{h}$ (2.32): however there are four unknown amplitudes (one reflected wave and three transmitted waves in the metal). Two additional boundary conditions are therefore required. These are the spin-pinning conditions on the amplitude of the components of the magnetization and the spatial derivatives of the magnetization at the surface, see Rado and Weertman[50]. For a uniaxial surface anisotropy energy, $E = K_s\cos^2(\theta)$, where θ is the angle between the magnetization and the x-axis and K_s is the surface anisotropy constant, with the axis parallel to the equilibrium direction of the magnetization the boundary conditions are:

$$\begin{aligned} A(\partial m_y/\partial z)|_o + K_s m_y|_o &= 0 \\ A(\partial m_z/\partial z)|_o + K_s m_z|_o &= 0 \end{aligned} \tag{2.39}$$

the subscript 0 indicating that the quantities are evaluated at the surface of the slab, $z = 0$. These boundary conditions have been discussed by Cochran, Heinrich and Dewar[48]. If $K_s = 0$ the conditions (2.39) become $\partial\bar{m}/\partial z|_o = 0$ corresponding to

'unpinned' or free spins. If K_s is large we have $\bar{m}|_0 \simeq 0$ corresponding to spins pinned at the surface.

With the geometry of Figure 2.4, and using space and time variations $\exp(i(kz-\omega t))$, the four boundary conditions (2.32) and (2.39) become:

$$
\begin{aligned}
& e_{ix} + e_{rx} = e_{1x} + e_{2x} + e_{3x} \\
& h_{iy} + h_{ry} = h_{1y} + h_{2y} + h_{3y} \\
& (iAk_1 + K_s)m_{1y} + (iAk_2 + K_s)m_{2y} + \\
& (iAk_3 + K_s)m_{3y} = 0 \\
& (iAk_1 + K_s)m_{1z} + (iAk_2 + K_s)m_{2z} + \\
& (iAk_3 + K_s)m_{3z} = 0
\end{aligned}
\tag{2.40}
$$

The subscripts 1, 2, 3 refer to the value of k for the three roots of equation (2.31). The electric field components in the metal are related to the $\bar{h}$ components by (see equations (2.33) and (2.34)):

$$e_{jx} = Z_{sj}\, h_{jy} \tag{2.41}$$

where:

$$Z_{sj} = -i\omega\delta^2 k_j/2c$$

The components of the microwave magnetizations $\bar{m}_j$ are related to

the h_{jy} by equations (2.17) with the appropriate value of k:

(2.42)

$$m_{jy} = \frac{M_s}{D}\left(B_o+\gamma+\frac{2A}{M_s}k_j^2-i\frac{\omega\ G}{\gamma\gamma M_s}\right)h_{jy}$$

$$m_{jz} = \frac{M_s}{D}\ i\frac{\omega}{\gamma}h_{jy}$$

$$D = \left(H_o+a+\frac{2A}{M_s}k_j^2-i\frac{\omega\ G}{\gamma\gamma M_s}\right)\left(B_o+\gamma+\frac{2A}{M_s}k_j^2-i\frac{\omega\ G}{\gamma\gamma M_s}\right)-\left(\frac{\omega}{\gamma}\right)^2$$

Combining equations (2.40), (2.41), (2.42) we may solve for the field amplitudes h_r, h_1, h_2 and h_3. Knowing the reflected wave amplitude enables one to calculate the power absorbed by the sample (see equation 2.37). The expressions for the wave amplitudes are complicated and there is little point in writing the equations out in detail. However a computer program has been written to calculate the susceptibility and to solve the boundary value problem numerically. The program calculates the absorption and the absorption derivative as a function of the applied field for a given set of parameters which characterize the metal.

Application to Nickel

Calculated curves of the absorption and the absorption derivative as a function of the applied field are shown in

Figure 2.5. Parameters appropriate to Nickel at room temperature and a microwave frequency of 24 GHz were used in the calculation. The values of the parameters are listed in Table 4-1 in Chapter 4. The field at which resonance occurs, H_{fmr}, and the FMR linewidth, ΔH, are indicated on the figure.

A brief discussion of the effect of the various parameters on the FMR absorption will be given here. This discussion will be amplified in Chapter 4. In the absence of MCA, damping and exchange, FMR occurs at the applied field where the permeability becomes infinite:

$$H_0(H_0 + 4\pi M_s) = (\omega/\gamma)^2 \qquad (2.43)$$

(see equation (2.18)). For the remainder of this section this field value will be termed H_{fmr0}. Including MCA, but neglecting damping and exchange, the permeability becomes, for the applied field along a (100) direction and the sample normal along $[1\bar{1}0]$:

$$\mu = \frac{(B_0 + 2K1/M_s)^2 - (\omega/\gamma)^2}{(B_0 + 2K1/M_s)(H_0 + 2K1/M_s) - (\omega/\gamma)^2} \qquad (2.44)$$

The permeability becomes infinite when:

$$(H_0+2K1/M_s)(H_0+4\pi M_s+2K1/M_s) = (\omega/\gamma)^2 \qquad (2.45)$$

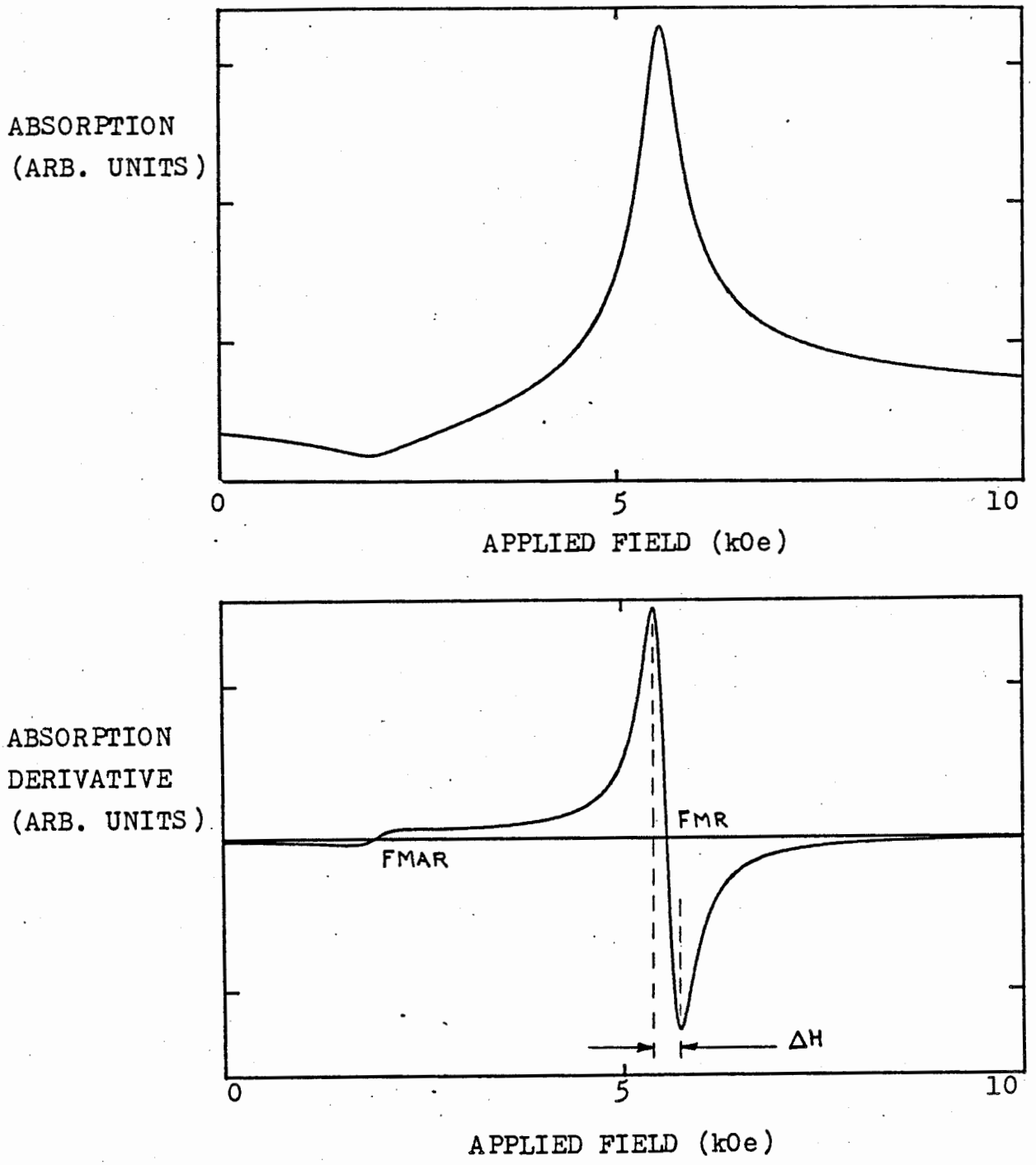

Figure 2.5 Calculated absorption and absorption derivative. Parameters appropriate for Nickel at room temperature were used in the calculation, see Table 4-1. The microwave frequency was 23.95 GHz.

that is the resonance field is shifted from H_{fmr0} by $2|K1|/M_s$. The shift is to a higher field if K1 is negative, as it is for Nickel. For M_s along a (111) direction the shift is to a lower field for Nickel (see Table 2-1). The direction of the shift for M_s along a (110) direction is not obvious as the anisotropy fields α and γ are different. The value $2|K1|/M_s$ provides a measure of the magnitude of MCA effects. For Nickel at room temperature $2|K1|/M_s \simeq 240$ Oe, and at 4.2 K $2|K1|/M_s \simeq 4.92$ kOe.

Including damping, but neglecting MCA and exchange, the permeability becomes:

$$\mu = \frac{(B_0 - i\frac{\omega\, G}{\gamma\gamma M_s})^2 - (\frac{\omega}{\gamma})^2}{(B_0 - i\frac{\omega\, G}{\gamma\gamma M_s})(H_0 - i\frac{\omega\, G}{\gamma\gamma M_s}) - (\frac{\omega}{\gamma})^2} \qquad (2.46)$$

$$\simeq \frac{B_0^2 - (\frac{\omega}{\gamma})^2 - 2B_0 i\frac{\omega\, G}{\gamma\gamma M_s}}{B_0 H_0 - (\frac{\omega}{\gamma})^2 - (B_0 + H_0) i\frac{\omega\, G}{\gamma\gamma M_s}}$$

where the second order term in $(G/\gamma M_s)$ has been neglected in the second equation. The permeability is now complex. It is important to remember that in an experiment we measure the absorbed power which varies as the real part of the square root of $-i$ times the permeability, see equation (2.38). The real and imaginary parts of the permeability become mixed in taking the square root. The result of damping is a shift in H_{fmr} to a higher field; and a broadening proportional to, and of the order of, $(\omega/\gamma)(G/\gamma M_s)$. At a frequency of 24 GHZ, at room

temperature, $(\omega/\gamma)(G/\gamma M_s)$ is approximately 200 Oe, while at 4.2 K it is approximately 1100 Oe.

Including exchange, but neglecting MCA and damping, the permeability becomes:

$$\mu = \frac{(B_o + \frac{2A}{M_s}k^2)^2 - (\frac{\omega}{\gamma})^2}{(B_o + \frac{2A}{M_s}k^2)(H_o + \frac{2A}{M_s}k^2) - (\frac{\omega}{\gamma})^2} \qquad (2.47)$$

The wavenumber, k, depends on the field through the permeability:

$$k^2 = 2i\mu/\delta^2$$

Again the permeability is complex. Since k^2 is proportional to $1/\delta^2$ the exchange field $2Ak^2/M_s$ is proportional to (A/δ^2) or $(A\sigma_o)$ where σ_o is the dc conductivity. A large conductivity results in a small skin depth and large gradients of the magnetization, i.e. the exchange field will be large. For Nickel at room temperature and a frequency of 24 GHz the skin depth $\delta = 0.9$ μm. At FMR $|\mu| \simeq 20$ so $k \simeq 5 \times 10^4$ cm^{-1}, and $2Ak^2/M_s \simeq 10$ Oe. The exchange field shifts the resonance. Some broadening is also produced as the field distribution in the metal is not described by a single wavenumber.

An idea of the relative importance of the damping and the exchange contributions to the shift in FMR and the linewidth may be had from the numbers listed in Table 2-2. Values of the

TABLE 2-2

	H_{fmr}(kOe)	δH(Oe)	ΔH(Oe)
G=0, A=0	5.326	--	--
$G=2.45\times10^{8}sec^{-1}$, A=0	5.337	11	300
G=0, $A=1.0\times10^{-6}$erg/cm	5.290	-36	50
$G=2.45\times10^{8}sec^{-1}$ $A=1.0\times10^{-6}$erg/cm	5.314	-12	320

Calculated values for the resonance field, H_{fmr}, the shift in peak position, $\delta H = H_{fmr} - H_{fmr0}$, and the linewidth, ΔH. Parameters appropriate for Nickel at room temperature were used in the calculations: $4\pi M_s$=6.16 kOe, f=23.95 GHz, $\rho=7.2\times10^{-6}$ Ωcm, The MCA constants have been set equal to zero for these calculations.

---

resonance field, H_{fmr}, the shift $\delta H = H_{fmr}-H_{fmr0}$, and the linewidth, ΔH are listed for four situations: (i) no damping, no exchange; (ii) damping, no exchange; (iii) exchange, no damping; and (iv) damping and exchange. Room temperature Nickel parameters were used in the calculations. Since MCA does not contribute to the linewidth it has not been included in these calculations. As can be seen from Table 2-2 the shift due to exchange is approximately three times that due to damping, and in the opposite direction, while the linewidth is dominated by the damping. Of course the shifts for case (iv) are not just the sum of those for cases (ii) and (iii).

2.3 Arbitrary Orientation of the Magnetization

The calculation described in Section 2.2 is valid only for the very stringent conditions that the sample plane coincides with a (110) crystal plane, that the applied field is parallel to the sample plane, and that the applied field be parallel to one of the three principal crystal axes (100), (110), or (111), in that plane. Since there is no static MCA torque on the magnetization for these directions the magnetization will be parallel to the applied field, at least at the field values of interest. This is the simplest geometry to treat and is that aimed for in an experiment.

Deviation from this ideal situation may occur for a number of reasons. The sample plane may not coincide with a (110) plane. The applied field may not be exactly aligned with the crystal axis, being tilted out of the sample plane or rotated in the plane. In such a case the magnetization will not, in general, be parallel to the applied field. A calculation of the FMR absorption must take this into account. The result of the lack of alignment is a shift and a broadening of the absorption line relative to the position and linewidth which would be expected if those effects were not considered. The magnitude of these so-called dragging effects in Nickel is greatest at low temperatures where the MCA becomes large.

The motives for carrying out the following calculation are twofold. First to determine the effect of a small misalignment

of the field with the crystal axes, either in or out of the sample plane, on the absorption. Second, to obtain an idea of the angular variation of the resonance field, H_{fmr}, in the (110) plane. The calculated variation of the resonance field may be compared with the experimental variation to determine the location of the principal axes in the sample plane. The angular variation of the resonance field has a maximum when the applied field is parallel to a (100) or (110) axis in the sample plane. It is straightforward to locate these axes in an experiment by rotating the magnet and finding the angle for which the resonance field has the largest value. The angular variation has a minimum near the (111) axis but the exact position of the minimum depends on the value of the MCA constants. To determine the location of the (111) axis it is necessary to compare the calculated and the experimental angular dependences. Also the agreement between the calculated and experimental angular variations serves as a test of how closely the sample plane coincides with a (110) crystal plane.

Three steps are involved in the calculation of the absorption as a function of the applied field. First the orientation of the magnetization in equilibrium for a given magnitude and orientation of the applied field must be determined. The permeability is then found using the Landau-Lifshitz equation. Finally the boundary value problem is solved. The second and third steps are the same as in the calculation outlined in Section 2.2 but the algebra is much more

involved.

A computer program was written to carry out this calculation numerically. The program yielded values for the orientation of the magnetization, the permeability, the wavevectors in the metal, the absorption and the absorption derivative. In the calculation that was programmed it was assumed that the sample plane was a (110) crystal plane. The applied field was allowed an arbitrary orientation with respect to the sample plane and the crystal axes. A local conductivity was assumed and exchange was neglected because of the complications involved. As was seen above exchange effects are comparatively small in Nickel. A further assumption, implicit in the calculation of Section 2.2, is that the sample forms a single domain. The magnetization changes by rotation only.

The geometry assumed is shown in Figure 2.6. The x-y-z axes are the same as those defined in Figure 2.1: the z-axis pointing into the slab, parallel to the sample normal, and the y-axis being parallel to the incident microwave magnetic field. This coordinate system will be called the 'laboratory frame'. The orientation of the applied field and the magnetization are specified by angles (θ_H,ϕ_H) and (θ,ϕ) respectively, the equilibrium values of (θ,ϕ) being (θ_M,ϕ_M). The sample normal is the $[1\bar{1}0]$ axis. The sample may be rotated about the $[1\bar{1}0]$ axis, the angle between the [001] axis and the x-axis being ψ.

In the calculation of the permeability it is desirable to work in a coordinate system with one axis parallel to the

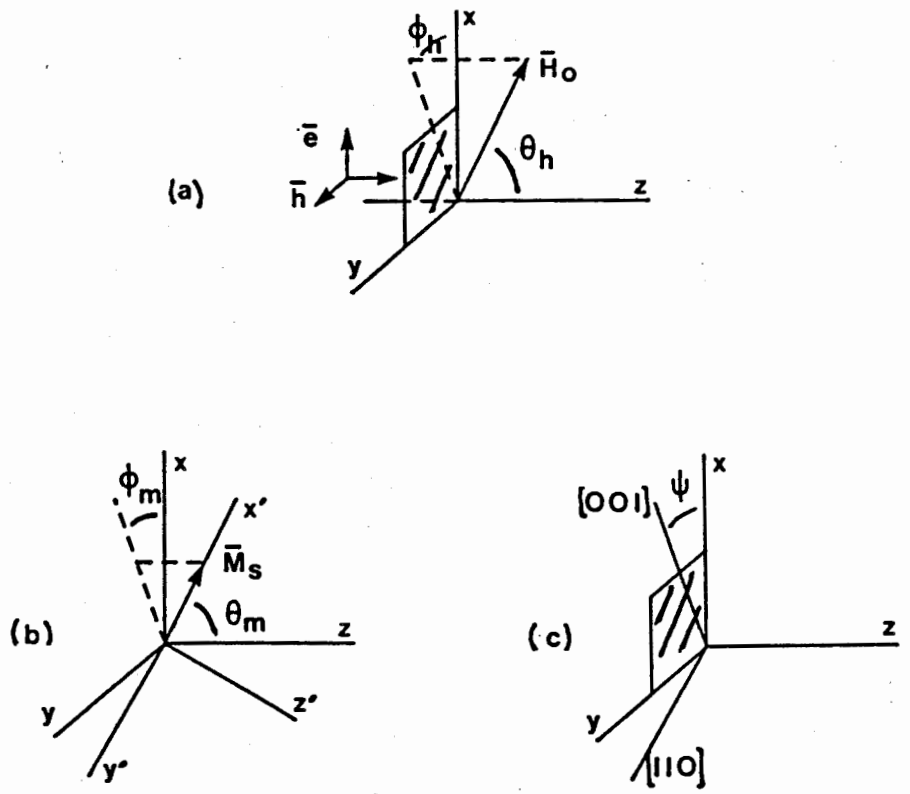

Figure 2.6 The angles required for the calculation of Section 2.3. The x-y-z axes define the laboratory frame where the sample lies in the x-y plane, the z-axis points into the slab and the y-axis is the direction of the microwave magnetic field. (a) The applied field, $\bar{H}_o$. (b) The magnetization, $\bar{M}_s$, and the magnetization frame x′-y′-z′. The x′ axis is parallel to $\bar{M}_s$, the y′ axis lies in the x-y plane. (c) The crystal axes, ψ is the angle between the [001] axis and the x-axis. The [001], [111] and [110] axes lie in the x-y plane.

magnetization as the Landau-Lifshitz equation has a simple form in such a system. The 'magnetization frame', (x',y',z'), is defined with the x′-axis along M_s. A convenient choice for a second axis is to have the y′-axis in the sample plane. The magnetization frame coincides with the laboratory frame if the magnetization lies along the x-axis.

If $\bar{h}$ is a vector in the laboratory frame, and $\bar{h}'$ is the same vector in the magnetization frame then:

$$\bar{h}' = \mathbf{T}\,\bar{h}$$

where $\mathbf{T}$ is the matrix representing a rotation about the z-axis by ϕ_M, followed by a rotation about the y′-axis by $(\pi/2 - \theta_M)$.

$$\mathbf{T} = \begin{bmatrix} \sin\theta_M\cos\phi_M & \sin\theta_M\sin\phi_M & \cos\theta_M \\ -\sin\phi_M & \cos\phi_M & 0 \\ -\cos\theta_M\cos\phi_M & -\cos\theta_M\sin\phi_M & \sin\theta_M \end{bmatrix} \qquad (2.48)$$

The permeability tensor is calculated in the magnetization frame $\tilde{\mu}'$. The transformation to the lab frame is:

$$\tilde{\mu} = \mathbf{T}^{-1}\tilde{\mu}'\mathbf{T}$$

where $\mathbf{T}^{-1}$ is just the transpose of $\mathbf{T}$.

Equilibrium Orientation of the Magnetization

Three equivalent ways of stating the equilibrium condition for the orientation of the magnetization are that M_s is parallel to the effective static internal field, that the torque on the magnetization is zero, or that the free energy is a minimum. In the calculation that was programmed the minimum of the free energy was found.

The contributions to the free energy are due to the applied field, $E = -\bar{M}\cdot\bar{H}_0$, the demagnetizing field, $E = 4\pi M_z^2$, where the in-plane demagnetizing field is neglected (see Section 2.2), and MCA, the energy being given by the series (2.6). The total free energy is:

$$E = -\bar{M}\cdot\bar{H}_0 + 4\pi M_z^2 + K1S + K2P + K3S^2 \qquad (2.49)$$

This expression written out in terms of θ_H, ϕ_H, ψ, θ and ϕ is very complicated. No apology is offered for not including it here. It is straightforward to set up a numerical procedure to find the angles θ_M and ϕ_M which minimize this energy.

To demonstrate the magnitude of this dragging effect plots of the calculated variation of θ_M and ϕ_M with the applied field are shown in Figures 2.7 and 2.8. MCA constants for Nickel at 4.2 K were used in the calculations. These are listed in Table 4-1 in Chapter 4. For the calculations shown in Figure 2.7 the applied field was parallel to the sample plane,

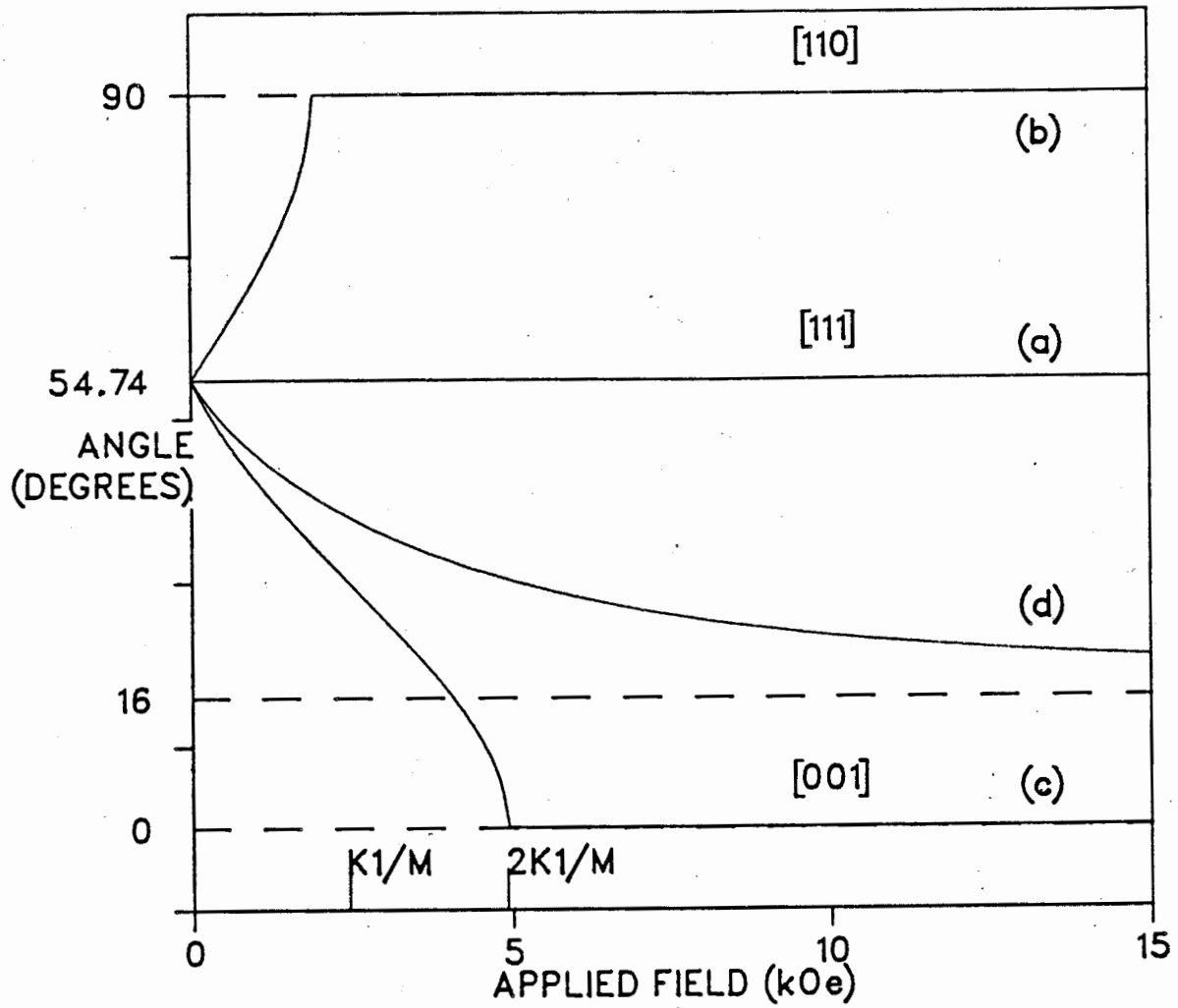

Figure 2.7 Calculated variation of the the direction of the magnetization with the applied field. The applied field was assumed to lie in the sample plane and parallel to (a) [111], (b) [110], (c) [001], (d) 16° from [001]. The angle between the magnetization and the [001] axis is plotted. For (b), (c) and (d) the direction of the applied field (ϕ_H) is indicated by a dashed line. Parameters appropriate for Nickel at 4.2 K were used in the calculation, see Table 4-1. The MCA fields $|K1|/M_s$ and $2|K1|/M_s$ are indicated on the figure.

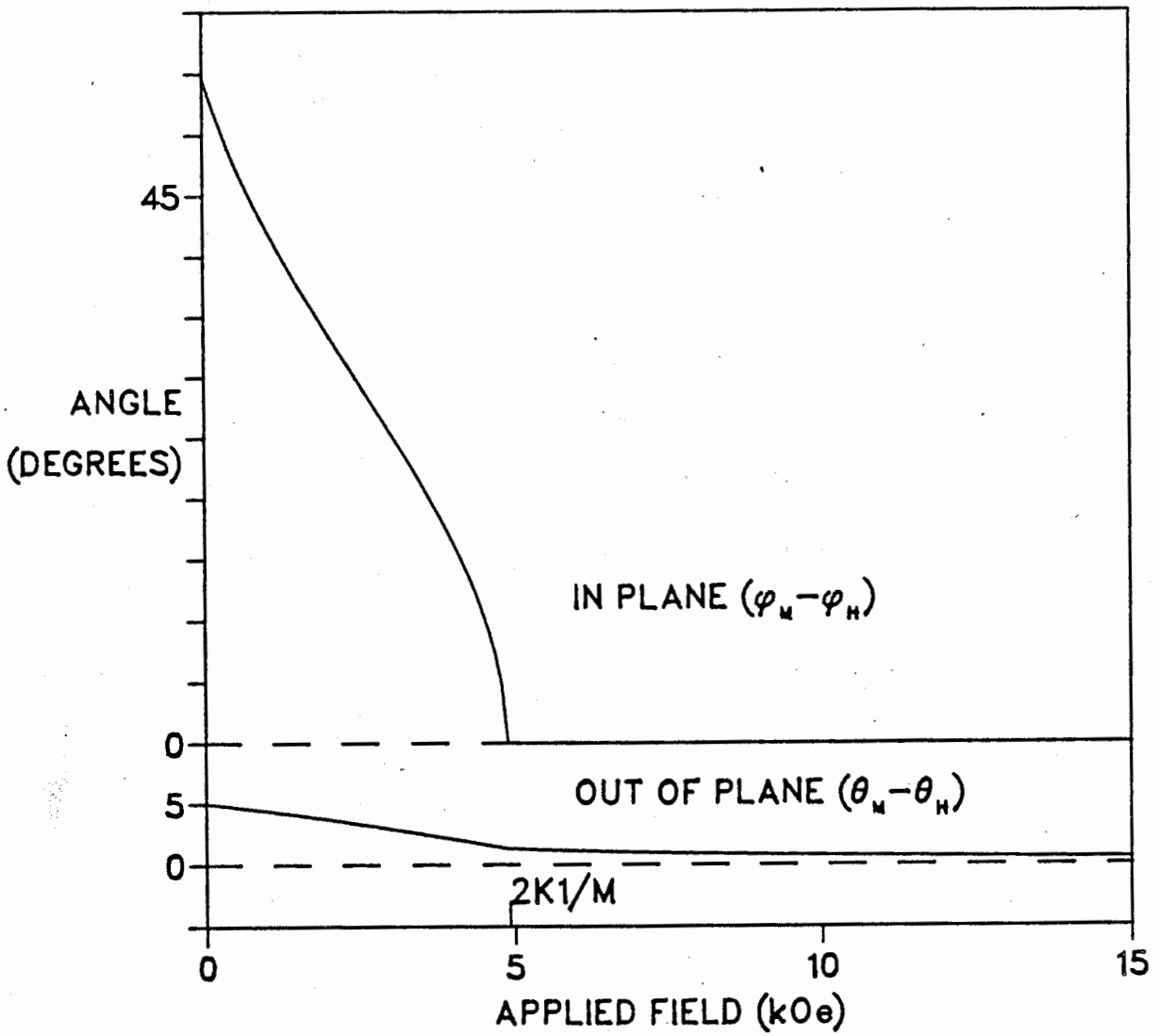

Figure 2.8 As Figure 2.7 however the applied field was assumed to point 5° out of the sample plane with its in-plane projection parallel to [001]. The angle between the in-plane components of $\bar{M}_s$ and $\bar{H}_o$, $(\phi_M - \phi_H)$, and the out-of-plane angle, $(\theta_M - \theta_H)$, are plotted. Parameters appropriate for Nickel at 4.2 K were used in the calculation, see Table 4-1.

and so the magnetization was also parallel to the plane. The angle between the magnetization and the [001] direction, $(\phi_M - \psi)$, is plotted rather than ϕ_M as this permits several plots to be displayed on one figure. The angle the field makes with the [001] direction, $(\phi_H - \psi)$, is shown by a dashed line. Curves are shown for the field along (a) [111]; (b) along [110]; (c) along [001]; and (d) 16° from the [001] direction. This last direction exhibits the most spectacular dragging effects. In curve (a) the magnetization is parallel to the field for all values of the field. For curves (b) and (c) the magnetization is parallel to the field for fields above approximately $|K1|/M_s$ (2.46 kOe) and $2|K1|/M_s$ (4.92 kOe) respectively. Alignment of the magnetization with the field occurs at exactly these field values if K2 and K3 are zero. Ferromagnetic resonance in Nickel at 24 GHz at 4.2 K occurs at field values of 5.5 kOe and 10 kOe respectively for these two directions so that dragging does not affect the observed resonance lines when the external field is applied along any of the three principle axes in the sample plane. In curve (d) it should be noted that even when the magnitude of the applied field is 15 kOe there is an angle of 5° between the magnetization and the field.

For the calculation shown in Figure 2.8 the applied field was tipped 5° out of the sample plane but with its in plane projection parallel to the [001] axis. The variation of ϕ_M is similar to that of Figure 2.7 (c). The variation of θ_M is approximately linear in field with a kink at $H_o = 2|K1|/M_s$, the

field at which ϕ_M becomes zero. The angle between $\bar{M}_s$ and $\bar{H}_o$ decreases from 1.5° at $H_o = 2|K1|/M_s$ to 0.5° at H_o = 12 kOe.

The Permeability

The Landau-Lifshitz equation, rewritten for reference, is:

$$-\frac{1}{\gamma}\frac{\partial \bar{M}'}{\partial t} = \bar{M}' \times (\bar{H}'_{eff} + \bar{h}'(\bar{r}',t)) - \frac{G}{\gamma^2 M_s^2}\bar{M}' \times \frac{\partial \bar{M}'}{\partial t} \qquad (2.12)$$

where the primes indicate quantities measured in the magnetization frame, since it is convenient to carry out the calculations in that frame. The effective fields (both static and dynamic) are found by taking the derivative of the free energy with respect to the magnetization:

$$\bar{H}'_{eff} = -\partial E/\partial \bar{M}' \qquad (2.50)$$

$$H'_x = -\partial E/\partial M'_x|_o = -E_x$$

$$H'_y = -\partial E/\partial M'_y|_o = 0$$

$$H'_z = -\partial E/\partial M'_z|_o = 0$$

where the energy E is given by equation (2.49), and we use the notation E_x to denote the derivative of the free energy with respect to M'_x evaluated at equilibrium ($M'_x = M_s$, $M'_y = 0$, $M'_z = 0$). H'_x is the static internal field. Expanding H'_y for small deviations from equilibrium ($\bar{m}'$):

$$H'_y = \partial H'_y/\partial m'_y|_o m'_y + \partial H'_y/\partial m'_z|_o m'_z \qquad (2.51)$$
$$= -\partial^2 E/\partial m'^2_y|_o m'_y - \partial^2 E/\partial m'_z \partial m'_y|_o m'_z$$

Similarly:

$$H_z = -\partial^2 E/\partial m'^2_z|_o m'_z - \partial^2 E/\partial m'_y \partial m'_z|_o m'_y \qquad (2.52)$$

The cross derivative could be made equal to zero by an appropriate rotation of the magnetization frame about the x′-axis. However with the frame as defined it is necessary to carry this term through. The term is zero if the magnetization lies in the sample plane or in a (100) or (110) crystal plane.

The second derivatives have two parts, one due to MCA, and one due to the microwave demagnetizing field. It was seen above (equation (2.24)) that the microwave demagnetizing field was treated automatically by Maxwell's equations without including it in the calculation of the susceptibility (2.13). By reviewing the steps outlined in Section 2.2 it can be seen that had the microwave demagnetizing field been included in the calculation of the susceptibility it would have been counted twice in the complete calculation. The effective fields (2.51 and 2.52) must include only the MCA contribution. With:

$$E_{yy} = \partial^2 E_{AN}/\partial m'^2_y|_o$$

$$E_{zz} = \partial^2 E_{AN}/\partial m_z'^2 |_o$$

$$E_{zy} = \partial^2 E_{AN}/\partial m_z' \partial m_y' |_o$$

then:

$$H_y' = -E_{yy} m_y' - E_{zy} m_z' \qquad (2.53)$$

$$H_z' = -E_{zz} m_z' - E_{zy} m_y'$$

If M_s lies in the sample plane ($\theta_M = \pi/2$) and along a principal axis, then $E_{yy} = M_s a$ and $E_{zz} = M_s \gamma$ where a and γ are the effective MCA fields listed in Table 2-1. The equations of motion become (with a time variation $\exp(-i\omega t)$):

$$m_x = 0$$

$$(-E_x + M_s E_{yy} - i(\omega/\gamma)(G/\gamma M_s)) m_y + (i\omega/\gamma + M_s E_{zy}) m_z = M_s h_y$$

$$-(i\omega/\gamma - M_s E_{zy}) m_y + (-E_x + M_s E_{zz} - i(\omega/\gamma)(G/\gamma M_s)) m_z = M_s h_z$$

The permeability is found following the same steps as in Section 2.1. The non-zero components of the permeability tensor are:

$$\mu_{xx}' = 1 \qquad (2.54)$$

$$\mu_{yy}' = [(-E_x + M_s E_{zz} - i(\omega/\gamma)(G/\gamma M_s))(-E_x + 4\pi M_s + M_s E_{yy} - i(\omega/\gamma)(G/\gamma M_s)) - (M_s E_{zy})^2 - (\omega/\gamma)^2]/D$$

$$\mu_{yz}' = -4\pi M_s (i\omega/\gamma + M_s E_{zy})/D$$

$$\mu'_{zy}=4\pi M_s(i\omega/\gamma - M_s E_{zy})/D$$

$$\mu'_{zz}=[(-E_x+M_s E_{yy}-i(\omega/\gamma)(G/\gamma M_s))(-E_x+4\pi M_s+M_s E_{zz}-i(\omega/\gamma)(G/\gamma M_s)] - (M_s E_{zy})^2 - (\omega/\gamma)^2)/D$$

$$D=[(-E_x+M_s E_{yy}-i(\omega/\gamma)(G/\gamma M_s))(-E_x+M_s E_{zz}-i(\omega/\gamma)(G/\gamma M_s)) - (M_s E_{zy})^2 - (\omega/\gamma)^2]$$

This permeability tensor is transformed into the lab frame:

$$\tilde{\mu} = \tilde{T}^{-1}\tilde{\mu}'\tilde{T}$$

In general all nine components of $\tilde{\mu}$ are non-zero.

Maxwell's Equations

The permeability tensor, $\tilde{\mu}$, is combined with Maxwell's equations in the same way as above (see equation (2.26)). We are neglecting exchange and therefore there are two values of k^2 corresponding to two forward and two backward propagating waves in the metal. If the magnetization is parallel to the sample plane these are the non-resonant wave with $\bar{h}$ parallel to $\bar{M}_s$, and the resonant wave with $\bar{h}$ perpendicular to $\bar{M}_s$. If the magnetization is perpendicular to the sample plane the two waves correspond to circularly polarized waves, one of which is resonant and the other is not. In the general case both waves have some resonant character.

The Boundary Value Problem

Both waves in the metal will be excited unless the magnetization is parallel to either the x or y-axes. As a result the reflected microwaves are elliptically polarized. The boundary conditions are (see Figure 2.4):

$$e_{ix} + e_{rx} = e_{1x} + e_{2x}$$

$$e_{ry} = e_{1y} + e_{2y}$$

$$h_{iy} + h_{ry} = h_{1y} + h_{2y}$$

$$h_{rx} = h_{1x} + h_{2x}$$

where e_1, h_1 and e_2, h_2 are the amplitudes of the two waves in the metal. From these equations, the relations between e_j and h_j, $e_j = Z_{sj} h_j$, and the equations (2.26) with the appropriate value of k, the unknown field amplitudes h_{rx}, h_{ry}, h_{1x}, h_{1y}, h_{2x} and h_{2y} may be found. The reflected power is:

$$P_r/P_i = (|h_{ry}|^2 + |h_{rx}|^2)/|h_i|^2 .$$

The calculation follows through as in Section 2.2.

An Example of the Effects of Dragging

The results of two calculations of the absorbed power as a function of the applied field are shown in Figure 2.9. The parameters used in the calculations were appropriate for Nickel at 4.2 K. These are listed in Table 4-1. For both calculations the applied field was parallel to the sample plane and 16° from the [001] direction (see Figure 2.7 for the variation of ϕ_M with the applied field for this situation). Curve (a) is the result that would be expected if dragging were not considered, if the magnetization remained parallel to the applied field for all values of the field. This is not what happens of course. In curve (b) the dragging has been taken into consideration. The shift in FMR to a lower field and the line broadening are clear from the comparison of the two curves.

Although graphs of the angular variation of H_{fmr} and the linewidth, ΔH, are presented in Chapter 4, a few numbers are worth quoting here. The linewidth is approximately 1600 Oe at 4.2 K. If the applied field is 1° away from the [001] axis, in the sample plane, the calculated linewidth is 10 Oe greater than the [001] linewidth. A 2° misalignment results in an additional broadening of 40 Oe. If the applied field is tipped 2° out of the sample plane with its in plane projection parallel to the [001] axis the additional broadening is 10 Oe (compare the angular variation of θ_M and ϕ_M in Figure 2.8). These differences are of the order of the experimental uncertainty.

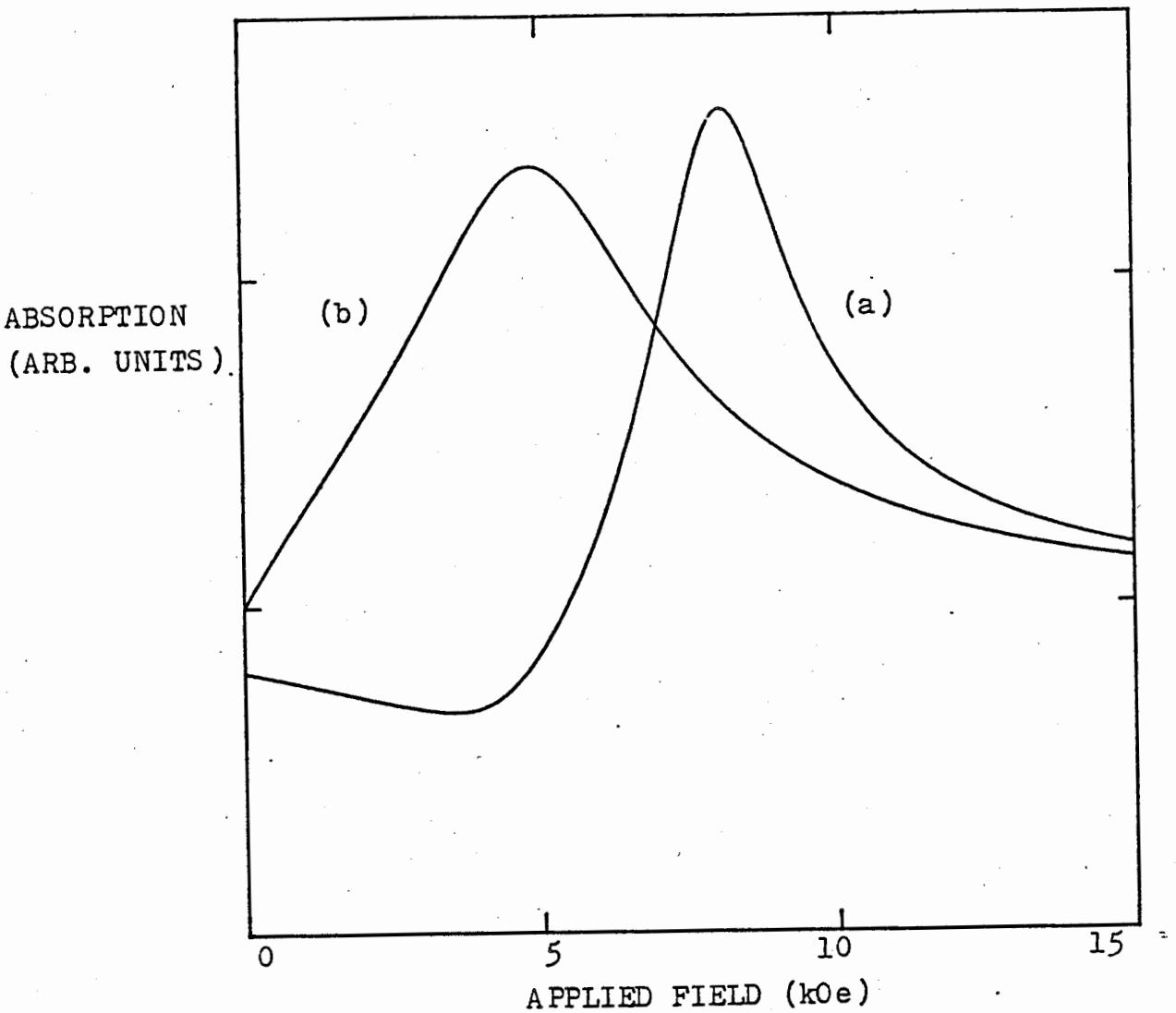

Figure 2.9 Calculated absorption in Nickel at 4.2 K, with the applied field assumed to lie parallel to the sample plane and 16° from the [001] axis. (a) the magnetization was assumed to remain parallel to the applied field for all values of the applied field. (b) the lack of alignment between the magnetization and the applied field was considered. Parameters used are listed in Table 4-1.

A Further Point

If we assume that the magnetization and the applied field are parallel then, by analogy with (2.45), resonance will occur at the value of the applied field which satisfies:

$$(\omega/\gamma)^2 = [H + a(\phi)][B + \gamma(\phi)] \tag{2.55}$$

where ϕ is the angle between the applied field and the [001] axis; with $\psi = 0$, $\phi = \phi_H = \phi_M$. The effective MCA fields are (compare 2.53):

$$a(\phi) = M_S \partial^2 E_{AN}/\partial m_y^2 |_\phi \tag{2.56}$$

$$\gamma(\phi) = M_S \partial^2 E_{AN}/\partial m_z^2 |_\phi$$

If we consider K1, K2 and K3 these effective fields are, in a (110) normal crystal plane:

$$a(\phi) = (1/M_S)[2K1 + (-13K1 + 3K2 + 12K3)\sin^2\phi +$$
$$(1/2)(24K1 - 23K2 - 122K3)\sin^4\phi +$$
$$(1/2)(18K2 + 171K3)\sin^6\phi - 36K3\sin^8\phi] \tag{2.57}$$

$$\gamma(\phi) = (1/M_s)[2K1 + (-7K1 - K2 + 4K3)\sin^2\phi + (1/2)(6K1 - K2 - 34K3)\sin^4\phi + (3/2)(K2 + 11K3)\sin^6\phi (9/2)(K3)\sin^8\phi]$$

If $2|K1|/M_s << H_{fmr}$ then M_s will be parallel to the applied field at the fields at which FMR occurs and the expression (2.55) will describe the angular variation of the resonance field (neglecting the damping and exchange shifts). This is the situation in Nickel at room temperature where $2|K1|/M_s \simeq 240$ Oe and $H_{fmr} \simeq 5$ kOe. If $2|K1|/M_s \simeq H_{fmr}$ as in Nickel at low temperatures where $2|K1|/M_s \simeq 4.92$ kOe, dragging will have a large effect and (2.55) will not describe the angular variation of H_{fmr}.

The expression (2.55) combined with the variation of the angle between the magnetization and the applied field, $\phi_M - \phi_H$, enables one to give a simple picture of why dragging leads to shifts of FMR and to broadened lines. In Figure 2.10 curves (c) and (d) of Figure 2.7 are plotted together with $H_{fmr}(\phi)$ of (2.55) plotted as ϕ against H_{fmr}. The microwave frequency in Figure 2.10(a) is 24GHz and 9.5GHz in Figure2.10(b). If the magnetization were parallel to the applied field FMR would occur at the intersection of the two curves ϕ_H and $H_{fmr}(\phi)$, for example at the points A and B in (a). As a first approximation we may assume that the effective static internal field (parallel to the magnetization) is equal to the applied field. This is true only if the magnetization is parallel to the applied field,

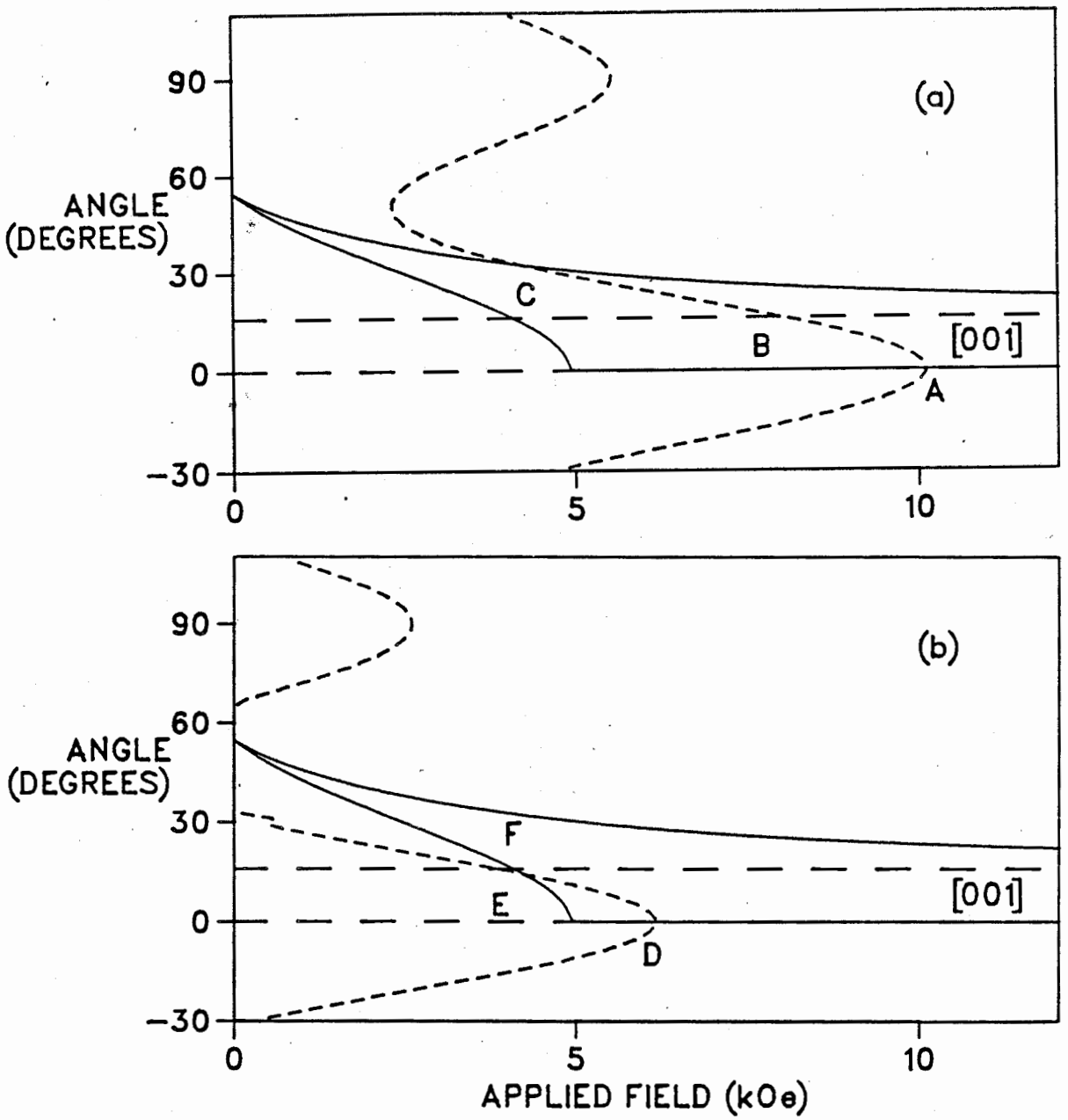

Figure 2.10 Calculated variation of the direction of the magnetization with the applied field, as in Figure 2.7. The short dashed lines are a plot of $H_{fmr}(\phi)$ from eqn (2.57) at (a) 24 GHz, (b) 9.5 GHz, plotted with the angle on the vertical axis. FMR occurs at the intersection of the curves $\phi_M(H)$ and $H_{fmr}(\phi)$: points A, B, D and F if dragging is ignored, points A, C, D and E if dragging is considered. Parameters appropriate for Nickel at 4.2 K were used in the calculations.

but this assumption is adequate for the present qualitative discussion. With this assumption FMR would occur at the intersection of $\phi_M(H)$ and $H_{fmr}(\phi)$, that is at the points A and C in (a). We see that the intersection at C is at a much lower value of the field than the intersection at B. This is the shift in the resonance which is seen in the calculated absorption curves shown in Figure 2.9. We could imagine drawing dashed lines parallel to $H_{fmr}(\phi)$ at $H_{fmr}(\phi)\pm\Delta H_0/2$ where ΔH_0 represents the linewidth with no dragging. The calculated linewidth with dragging would be the field interval between the intersections of $\phi_M(H)$ with the curves $H_{fmr}(\phi)\pm\Delta H_0/2$. For the [001] curve this interval is just ΔH_0. However for the applied field 16° off [001] this interval would be much greater than ΔH_0.

The effects of dragging become more pronounced at low microwave frequencies because of the smaller values of H_{fmr}. The variation of $H_{fmr}(\phi)$ at 9.5 GHz is shown in Figure2.10(b) with the same curves of $\phi_M(H)$ as in (a). If the applied field is parallel to [001] the curve $\phi_M(H)$ intersects $H_{fmr}(\phi)$ at two points, D and E. This means that the absorption line will have two peaks, the peak corresponding to D being the peak expected if there were no dragging and the peak at E being purely a result of dragging. This behaviour is observed in Nickel at 4.2 K, see Chapter 4. For the applied field 16° off the [001] axis the resonance would be expected at F if there were no dragging, but as can be seen from the figure, no resonance will

be observed as the curves $\phi_M(H)$ and $H_{fmr}(\phi)$ do not intersect. This behaviour is also observed experimentally, the resonance disappearing for small angles between the applied field and the [001] axis.

2.4 The Anomalous Skin Effect and FMR

The calculations outlined in Sections 2.2 and 2.3 describe the experimental results well when the temperature is large enough that the electrical conduction at microwave frequencies can be described by Ohm's law using the dc conductivity. At low temperatures the conductivity increases and the conduction electron mean free path, l, may become comparable to the microwave skin depth, δ. When this occurs Ohm's law does not provide a satisfactory description of the electrical conduction. The electrical conductivity becomes wavenumber dependent or non-local. According to the analysis of Korenman and Prange[3,4] the magnetic damping also becomes wavenumber dependent at low temperatures. The wavenumber dependence of the damping is related to the increase in the conduction electron mean free path as discussed in Chapter 1. In this Section we outline a procedure for calculating the FMR absorption with wavenumber dependent quantities.

First let us consider the criteria for determining when wavenumber dependent effects will be important. The electrons in a metal which contribute to the electrical conduction travel

at the Fermi velocity v_F. The conductivity is limited by the scattering of these conduction electrons by phonons or impurities. If the average time between scattering of an electron is τ, the electron mean free path is $l = v_F\tau$.

Ohm's law is:

$$\bar{j}(\bar{r},t) = \sigma_0\bar{e}(\bar{r},t) \qquad (2.22)$$

where j is the current density, e is the electric field and σ_0 is the dc conductivity. Ohm's law states that the current density at a point in space at a certain time is related to the electric field at that point and at that time only. The relationship between the current density and the electric field is said to be a local one. This relation holds if (i) the mean free path l is much shorter than the length of spatial variations of the electric field, or $ql << 1$ where q is a typical wavevector of the electric field; and (ii) the relaxation time τ is much shorter than the period of oscillation of the electric field, or $\omega\tau << 1$ where ω is the angular frequency of the electric field. These two conditions are equivalent to saying that the electron experiences a constant electric field between scattering events. If either of these conditions does not hold the simple local relation between the current density and the electric field must be replaced by a non-local relation which accounts for the fact that the current density at a point at a given time depends on the value of the

electric field at other points in space and at earlier times. The non-local relation is written:

$$\bar{j}(\bar{r},t) = \int d^3r dt' K(\bar{r}-\bar{r}';t-t')\bar{e}(\bar{r}',t')$$

The electrical conductivity is described by the quantity K. If the electric field varies in space and time as $\exp(i(\bar{q}\cdot\bar{r}-\omega t))$, i.e. if the field is described by a single wavenumber q, and a single frequency ω, this relation becomes, for an infinite medium:

$$\bar{j}(\bar{q},\omega) = \sigma(\bar{q},\omega)\bar{e}(\bar{q},\omega) \qquad (2.58)$$

where $\sigma(\bar{q},\omega)$ is the frequency and wavenumber dependent conductivity, $\sigma(\bar{q},\omega)$ is the Fourier transform of $K(\bar{r},t)$. This expression resembles Ohm's law and may be called a generalized Ohm's law.

If we assume that the local Ohm's law is valid and consider what happens when an electromagnetic wave of frequency ω is incident on a non-magnetic metal($\mu = 1$), the electric field in the metal will be:

$$\bar{e}(\bar{r},t) = \bar{e}_0\exp(i(\bar{k}\cdot\bar{r}-\omega t))$$

where $k = (1 + i)/\delta$ and δ is the skin depth for a local conductivity, $\delta^2 = c^2/2\pi\sigma_0\omega$. The electric field oscillates in

space with a wavelength $2\pi\delta$ and the amplitude decays exponentially with distance into the metal with a decay constant δ. The wavenumber spectrum of this electric field distribution has a maximum at $q = 1/\delta$, that is, the scale of spatial variation of the electric field is determined by the skin depth. The condition $ql << 1$ is equivalent to $l/\delta << 1$. The wavenumber dependence of the conductivity becomes important when $ql \simeq 1$, or when the electron mean free path becomes comparable to the skin depth expected from a calculation based on a local conductivity.

In a magnetic metal $k = \sqrt{2i\mu}/\delta$ (equation 2.29), the effective skin depth is reduced by the permeability. Since the permeability is large at FMR the values of q are also large and $q(FMR)l$ may be $>> ql$ for a non-magnetic metal having the same dc conductivity. This means that wavenumber dependent effects may be important at FMR at much higher temperatures than for a non-magnetic metal having the same dc conductivity.

A consequence of the wavenumber dependence of the conductivity is that the microwave penetration depth is no longer δ when $ql > 1$ but saturates at a constant value $\delta_A = (\delta^2 l)^{1/3}$[8]. For FMR measurements this means that the effects of exchange at low temperatures are reduced over those which would be expected if a local conductivity were used.

Some representative values for Nickel are given in Table 2-3 for room temperature, and for resistivity ratios of 10, corresponding to 77 K, 38, corresponding to 4.2 K for the

samples used in our experiments, and 100. Listed in the Table are the values of the skin depth for a permeability of 1, the magnitude of the permeability at FMR calculated using the program of Section 2.3 with the values of the damping parameter required by experiment (see Chapter 4), the values of the average wavevector q for permeability 1 and at FMR assuming $q = 1/\delta$, the electron mean free path and the dimensionless ratios $\omega\tau$ and ql. These numbers should be viewed as approximate, not absolute. As can be seen $\omega\tau$ is estimated to be much less than 1 over the range of temperature and purity represented in the Table. While ql is much less than 1 at room temperature it is clear that wavenumber dependent effects are likely to be important at low temperatures. The temperature at which wavenumber dependent effects become important is a matter for experiment to decide but we can see, for example, that a local conductivity would probably be applicable for Nickel at 77 K.

Having established the need for considering a non-local conductivity we may write down the expression for the conductivity of a metal characterized by a spherical Fermi surface[51]:

$$\sigma(q,\omega)=\sigma_0\{-\frac{3(1-i\omega\tau)}{2(ql)^2}+\frac{3i}{4ql}[1+(\frac{1-i\omega\tau}{ql})^2]\ln(\frac{1-i\omega\tau-iql}{1-i\omega\tau+iql})\} \qquad (2.59)$$

In the limit $ql<<1$ and $\omega\tau<<1$ this expression reduces to the dc

TABLE 2-3

Temp. (K)	295	77	4.2	--
ρ_{295}/ρ_4	1	10	38	100
τ(sec)	10^{-14}	10^{-13}	3.8×10^{-13}	10^{-12}
$\omega\tau$	1.5×10^{-3}	1.5×10^{-2}	5.7×10^{-2}	1.5×10^{-1}
δ(cm)(μ=1)	8.7×10^{-5}	2.7×10^{-5}	1.4×10^{-5}	$.87\times10^{-5}$
$q=1/\delta(cm^{-1})$	1.2×10^{4}	3.6×10^{4}	7.1×10^{4}	11.5×10^{4}
G(sec^{-1})	2.45×10^{8}	8×10^{8}	14×10^{8}	14×10^{8}
$\lvert\mu$(FMR)$\rvert$	21.2	7.6	4.6	4.6
q(FMR)(cm^{-1})	5.3×10^{4}	10.0×10^{4}	15.2×10^{4}	24.7×10^{4}
l (A)	25	250	950	2500
q(FMR)l	0.013	0.25	1.44	6.2

$\delta^2 = c^2/2\pi\omega\sigma_0 = 10^9\rho(\Omega cm)/4\pi^2 f$

$q(FMR) = q\sqrt{|\mu(FMR)|}$

$\rho_{295} = 7.2\times10^{-6}\Omega cm$

f = 24 GHz

$v_F = 2.5\times10^7$ cm/sec

$l = v_F\tau$

The values of the damping parameter used in calculating the permeability are those required by experiment, if a non-local conductivity and a wavenumber independent damping is assumed, see Chapter 4.

conductivity σ_0; in the limit $ql>1$ and $\omega\tau<<1$:

$$\sigma(q,\omega) = (3/2)\sigma_0 \arctan(ql)/ql$$

using $\arctan(x) = (i/2)\ln[(1-ix)/(1+ix)]$. Although the Fermi surface of Nickel is not spherical this expression can be expected to provide a good first approximation.

The permeability is also wavenumber dependent. The calculation of the permeability follows exactly as in Section 2.2. If the exchange torque is considered the permeability depends on q. This wavenumber dependence was treated in Section 2.2. At low temperatures the magnetic damping becomes wavenumber dependent introducing an additional q-dependence. This is a result of the intra-band scattering mechanism mentioned in the Chapter 1. Following the discussion of Cochran and Heinrich[37] the spin-flip and intra-band contributions to the damping may be included by assuming:

$$G(q,T) = a(\sigma_0(T)/\sigma_0(295))\arctan(ql_D)/ql_D + b\rho(T)/\rho(295) \qquad (2.60)$$

where T is the temperature. The first term corresponds to the result of Korenman and Prange[3,4] for intra-band scattering, while the second is the result expected for spin-flip scattering(Elliott[10], Kambersky[2]). The parameters a and b are varied to match the experimental results for the temperature

dependence of the damping parameter[37]. The mean free path which enters the damping, l_D, is the mean free path of the d-band electrons on the X_5 hole pockets. There is no reason to assume that this mean free path should be the same as the mean free path which enters the conductivity. This expression provided a good description of the FMAR results of Cochran and Heinrich with the substitution $\arctan(ql_D)/ql_D = 1$ at FMAR. Since δ is large at FMAR, ql_D is small.

The wavenumber dependent permeability, including exchange and wavenumber dependent damping is:

$$\mu(q) = \frac{(B_0+a+\frac{2A}{M_S}q^2-i\frac{\omega G(q)}{\gamma\ \gamma M_S})(B_0+\gamma+\frac{2A}{M_S}q^2-i\frac{\omega G(q)}{\gamma\ \gamma M_S})-(\frac{\omega}{\gamma})^2}{(H_0+a+\frac{2A}{M_S}q^2-i\frac{\omega G(q)}{\gamma\ \gamma M_S})(B_0+\gamma+\frac{2A}{M_S}q^2-i\frac{\omega G(q)}{\gamma\ \gamma M_S})-(\frac{\omega}{\gamma})^2} \qquad (2.61)$$

A calculation involving a wavenumber dependent conductivity requires a knowledge of how the conduction electrons scatter after a collision with the metal surface. Two limiting cases are usually discussed: (i) specular scattering, or mirror reflection of electrons colliding with the surface; or (ii) diffuse scattering, where the trajectory of an electron after a collision with the surface is totally unrelated to the trajectory before the collision. A complete calculation would also have to include the effect of the applied magnetic field on the trajectories of the conduction electrons.

Cochran and Heinrich[52] have carried out calculations of the absorption and transmission of microwaves in ferromagnetic

materials using a non-local conductivity. Three combinations of surface scattering, curvature of electron orbits in the applied magnetic field and exchange were used in the calculations: (i) specular scattering, curvature of the orbits neglected and exchange; (ii) diffuse scattering, curved orbits and no exchange; and (iii) diffuse scattering, curvature of the orbits neglected and no exchange. Their results show that the field dependence of the absorption is insensitive to the type of surface scattering, and that neglect of the curvature of the electron orbits has little effect. This insensitivity is a result of the similarity of the electric field distributions in the skin layer for the two forms of surface scattering.

The computer program we used to make calculations for comparison with experiment was the program of (i) above with the addition of a wavenumber dependent damping of the form 2.60. We will outline the procedure used to calculate the absorption with the assumptions of specular scattering, wavenumber dependent permeability and no curvature of electron orbits. For a discussion of the calculation of the absorption if diffuse scattering is assumed the reader is referred to the paper of Hirst and Prange[9].

The same geometry was used for this calculation as was used for the calculation of Section 2.2, see Figures 2.1 and 2.4. The sample is assumed to form a slab of infinite extent lying in the x-y plane. The front surface of the slab is at $z = 0$. The slab thickness is much greater than the microwave skin depth so

that the sample may be considered semi-infinite in the z-direction. The applied field lies in the sample plane and points in the x-direction. We consider only cases where the applied field is parallel to a principal axis and assume that the magnetization is parallel to the applied field for all values of the applied field. The calculation will be valid for all field values if the field is along (111), for fields greater than $|K1|/M_s$ if the field is along (110) and for fields greater than $2|K1|/M_s$ if the field is along (100), see Section 2.3. MCA is included through the effective fields a and γ, see Table 2-1. Microwaves travel in the +z-direction with the electric field in the x-direction and the magnetic field in the y-direction.

As was demonstrated in Section 2.2 the power absorbed by the specimen is proportional to the real part of the surface impedance. The surface impedance is the ratio of the electric and magnetic fields at the surface of the metal. With the geometry of Section 2.2:

$$Z_s = e_x(0)/h_y(0)$$

In Section 2.2 this quantity was found by (i) solving the Landau-Lifshitz equation for the permeability μ; (ii) combining this permeability with Maxwell's equations to determine the wavevectors of the waves which could propagate in the metal; and (iii) solving the boundary value problem of the reflection of microwaves from the surface of the metal. With a wavenumber

dependent conductivity (ii) is not as simple as in the local conductivity case as we cannot use Ohm's law to relate the current density in the metal to the electric field. Instead we work with the Fourier transforms of the fields in the metal and use the generalized Ohm's law (2.58).

To describe the approach taken when assuming specular scattering we can do no better than to quote Pippard[8]: "With specular scattering electrons leaving the surface have suffered an energy change exactly as if they had come straight through the surface from an identical semi-infinite metal in which the real electric field is mirrored. We may therefore replace the real problem by one in which the metal is infinite and $e_x(-z) = e_x(z)$. There will be a discontinuity in the gradient of e_x at $z = 0$ which means that there must be a current sheet I supplied by an external source at $z = 0$ in order to produce any field in the infinite metal." Pippard was considering the case in which there was no applied magnetic field so that the electron orbits were not curved. We have a magnetic field but are neglecting the curvature of the orbits and so may use the same replacement. Since $e_x(-z) = e_x(z)$, from Faraday's law $h_y(-z) = -h_y(z)$ and there will be a discontinuity in h_y at $z = 0$.

Maxwell's equations are:

$$\nabla \times \bar{e} = -(1/c)\partial \bar{B}/\partial t$$

$$\nabla \times \bar{h} = (4\pi/c)\bar{j}$$

where the displacement current has been neglected as in Section 2.2. The fields are assumed to vary in the z-direction only and to have a time dependence $\exp(-i\omega t)$ so:

$$\partial e_x/\partial z = (i\omega/c)b_y \qquad (2.62)$$
$$\partial h_y/\partial z = -(4\pi/c)j_x$$

If Ohm's law were valid we would have $j_x = \sigma_0 e_x$ and we would recover the results of Section 2.2. We take the Fourier transform of these equations by multiplying by $\exp(iqz)$ and integrating from $z = -\infty$ to $z = +\infty$. Remembering the discontinuity at $z = 0$ we have:

$$qe_x(q) = -(\omega/c)b_y(q) = -(\omega/c)\mu(q)h_y(q) \qquad (2.63)$$
$$2h_0 + iqh_y(q) = (4\pi/c)j_x(q) = (4\pi/c)\sigma(q)e_x(q)$$

where $f(q) = \int_{-\infty}^{\infty}\exp(iqz)f(z)$ and h_0 is the value of the magnetic field at $z = 0+$. Combining these equations:

$$e_x(q) = \frac{-2i(\omega/c)\mu(q)}{q^2-(4\pi i\omega/c^2)\mu(q)\sigma(q)}\,h_0 \qquad (2.64)$$

Since:

$$e_x(z) = (1/2\pi)\int_{-\infty}^{\infty} dq\ \exp(-iqz)e_x(q) \qquad (2.65)$$

then:

$$e_x(0) = (1/2\pi)\int_{-\infty}^{\infty} dq\ e_x(q) \qquad (2.66)$$

and the surface impedance is:

$$Z_s = \frac{e_x(0)}{h_y(0)} = \frac{1}{2\pi} \int_{-\infty}^{\infty} \frac{-2i(\omega/c)\mu(q)}{q^2-(4\pi i\omega/c^2)\mu(q)\sigma(q)} dq \qquad (2.67)$$

The absorbed power is:

$$P_a/P_0 = 4\mathrm{Re}(Z_s)$$

Given expressions for the wavenumber dependent conductivity and permeability it is straightforward to carry out this integration numerically.

The integral may be evaluated analytically in the extreme anomalous limit, ($ql >> 1$), if the permeability is wavenumber independent, ie if a local damping parameter is used and exchange is neglected. In the extreme anomalous limit the conductivity is:

$$\sigma(q) = (3\pi/4)(\sigma_0/l)(1/q)$$

and the surface impedance becomes†:

$$Z_s = (1 - \sqrt{3}i)\left(\frac{l}{3\pi^2 c\sigma_0}\right)^{1/3}(\omega\mu)^{2/3} \qquad (2.68)$$

This expression may be combined with the permeability obtained with the calculation of Section 2.3 to obtain the absorption in the extreme anomalous limit with no exchange and a local damping. The computer program written to perform the calculation of the absorption assuming a wavenumber dependent conductivity and damping gave results in good agreement with those calculated using this expression for the surface impedance in the extreme anomalous limit.

We had two other checks on the program. The results of the program agreed with the results of the program which carried out the calculation of Section 2.2 in the local limit, $ql \ll 1$. The second check was to compare line positions and widths with the calculated line positions and widths quoted by Hirst and Prange[9] from their calculation of the absorption which assumed a non-local conductivity and diffuse scattering of electrons at the sample surface. Our results were in good agreement with theirs.

---

† A factor of $4\pi/c$ is often included in the definition of the surface impedance, see for example Hirst and Prange[9].

3. EXPERIMENTAL DETAILS

3.1 Introduction

The FMR linewidth, ΔH, increases with decreasing temperature and saturates at low temperatures if the resistivity ratio is greater than approximately 30(Bhagat and Hirst[1]). We wish to determine whether the linewidth, and hence the magnetic damping, is anisotropic at low temperatures. To do this we measure FMR with the external field parallel to each of the three principal axes, (100), (110) and (111). Ideally we would measure the temperature dependence of ΔH for each of these three axes from room temperature to 4.2 K where the linewidth saturates. The greatest interest is attached to the 4.2 K measurements where any dependence of ΔH on the direction of the external field with respect to the crystal axes should be most evident.

The FMR line becomes very broad on cooling: ΔH at a microwave frequency of 24 GHz increases from 320 Oe at room temperature to approximately 1600 Oe at 4.2 K. The peak absorption also becomes weaker as the specimen is cooled and at 4.2 K is approximately 7% that at room temperature (based on the calculations outlined in Chapter 2). The conventional method for measuring FMR uses a field modulation technique which

measures the derivative of the absorption with respect to the applied field. If a constant modulation amplitude is maintained the signal at 4.2 K is smaller than the room temperature signal by a factor greater than 50. In practice the modulation amplitude is reduced at low temperatures by screening due to eddy currents. Using this technique we were able to observe FMR at the lowest temperature accessible with liquid nitrogen (pumped liquid nitrogen $\simeq$ 60 K), but could not see any signal at 4.2 K. For the 4.2 K measurements the absorption of the sample was measured directly using a bolometer. Measurements of the linewidth were not made between 4.2 K and 60 K, however the resonance field could be measured over the entire temperature range by monitoring the dc voltage on the microwave diode.

In this chapter we discuss (i) the samples and their preparation; (ii) detection of the FMR signal; (iii) the 24 GHz microwave cavity and the sample mounting; (iv) the 24 GHz microwave system and (v) measurements at other frequencies.

Useful references for this chapter are "Technique of Microwave Measurements" by Montgomery[53] and "Microwave Measurements" by Ginzton[54] for the properties of microwave components and resonant cavities and "Electron Spin Resonance" by Poole[55] for information on all experimental aspects of magnetic resonance studies. Any unreferenced statements in this chapter may be traced to one of these three books.

3.2 Samples

The quality and preparation of a sample used in an FMR experiment is extremely important for obtaining reliable results. Strains, imperfections and deviations from flatness lead to broadening of the FMR line which obscures the intrinsic contribution to the linewidth. We cite for example the experience of Frait and MacFaden[26] with Nickel. Even with careful preparation of the sample they obtained linewidths some 200 Oe larger than the intrinsic linewidth (at 25 GHz).

The samples used for the present experiments were thin disks cut with a (110) direction normal to the plane of the disk. The (110) plane contains the three principal axes (100), (110) and (111) (see Figure 2.2). The starting material was a boule of single crystal Nickel, 3/4 inches in diameter, nominal purity 99.99%, purchased from Mono Crystals[†]. The residual resistivity ratio (RRR = ρ_{295}/ρ_4) of this material measured on one of the samples used for FMR measurements was 38. Bhagat and Hirst[1] found that the linewidth at 4.2 K was independent of the resistivity ratio if this ratio was greater than approximately 30.

The boule was oriented with x-rays using the Laue back reflection technique. The error in alignment (angle between the sample normal and a (110) axis) was less than 1.5 degrees. Slabs approximately 1 mm thick were spark cut from the boule,

[†]Mono Crystals, 1721 Sherwood Blvd., Cleveland, Ohio

then spark cut into circular disks 16 mm in diameter, the largest diameter consistent with the microwave cavity used. The disks were mechanically polished, on both sides, initially with 300 grit silicon carbide paper, followed by 600 grit paper, to a thickness of approximately 500 μm. Approximately 75 μm was removed from each side alternately to a thickness of approximately 300 μm. One side was polished with 9 μm diamond grit then electropolished. Electropolishing was done in a solution of 60% H_2SO_4, 40% distilled water at room temperature with a current density of approximately 1 amp/cm^2[56]. The other side of the sample was then diamond polished to within 50 μm of the final thickness and electropolished. Sample surfaces after electropolishing were smooth and mirror-like. The final thickness was approximately 150 μm. This was a convenient thickness to work with. The ratio of diameter to thickness was 100 so that the demagnetizing field (equation 2.3) was small, being approximately 30 Oe.

The samples were not annealed. Bhagat and Lubitz[13] found that the FMR linewidth at 22 GHz of well annealed samples was at most 20 Oe narrower than samples which had not been annealed. Also annealing usually causes the resistivity ratio to decrease, presumably because of incorporation of impurities(Dewar[57]).

3.3 Experimental Observation of FMR

The task is to measure the power absorbed by a sample from an incident microwave field polarized with the microwave magnetic field perpendicular to a static magnetic field. The simplest way to do this is to use the sample as a termination on the end of a piece of waveguide and monitor the reflected power. The microwave circuit for such a system would consist of a klystron, an isolator to match the klystron to the rest of the circuit, a directional coupler to intercept a portion of the microwaves reflected from the sample, and a diode to detect this signal.

If the steps outlined in Section 2.2 to obtain the equation (2.36) were repeated using boundary conditions appropriate for a sample in a waveguide the power reflected from the metal surface would be found to be:

$$P_r = \frac{|1 - Z_s/Z_w|^2}{|1 + Z_s/Z_w|} P_o \qquad (3.1)$$

where P_o is the incident power, Z_s is the surface impedance of the metal, if the conductivity is described by Ohm's law $Z_s=(\omega\delta/2c)\sqrt{-2i\mu}$, δ is the skin depth, $\delta^2=c^2/2\pi\sigma\omega$, and Z_w is the waveguide impedance, the ratio of the maximum amplitudes of e and h in the waveguide. The waveguide used in the 24 GHz experiments was WR42 or RG53/U waveguide (equivalent designations). The inside dimensions of this guide are

0.420 x 0.170 inches. The cutoff wavelength, λ_c, the guide wavelength, λ_g and the impedance for the TE_{10} waveguide mode are (for 24 GHz, λ = 1.25 cm):

$$\lambda_c = 2x(0.420 \text{ inches}) = 2.13 \text{ cm}$$

$$\lambda_g = \lambda/\sqrt{1-(\lambda/\lambda_c)^2} = 1.54 \text{ cm}$$

$$Z_w = \lambda_g/\lambda = 1.23$$

Since Z_w is close to 1 we will equate it to 1 in the essentially qualitative discussion that follows. For Nickel at room temperature and 24 GHz the surface impedance is:

$$Z_s \simeq 2.2x10^{-4}(1-i) \quad (\mu = 1)$$

$$Z_s \simeq 1.4x10^{-3} \quad (FMR, \mu \simeq 20i)$$

Since the surface impedance is small (see equations 2.38):

$$P_r \simeq (1 - 4Re(Z_s))P_o \tag{3.2}$$

$$P_a \simeq 4Re(Z_s)P_o$$

It is useful to write the absorbed power in terms of the magnetic field at the surface of the sample since it is the magnetic field at the surface that is known in a resonant cavity

(see below):

$$P_a = (1/4) f \delta \mathrm{Re}(\sqrt{-i\mu/2}) \int h_t^2 dS \qquad (3.3)$$

where f is the frequency and the integral is over the tangential components of the microwave magnetic field. The magnetic field at the surface is just twice the incident magnetic field.

The absorbed and reflected power vary as the external field is swept through FMR. The fraction of the incident power absorbed when $\mu = 1$ and the ratio of the change in reflected power on sweeping through FMR to the reflected power are (using the values of Z_s quoted above):

$$P_a/P_o \simeq 8.8 \times 10^{-4}$$

$$\Delta P_r/P_r \simeq \Delta P_r/P_o \simeq 4.8 \times 10^{-3}$$

The signal is small and is superimposed on a large background.

The signal to noise ratio may be improved by using field modulation. A small alternating magnetic field is applied parallel to the dc magnetic field. The component of the reflected signal at the frequency of the modulation field is detected and amplified by a lock-in amplifier. If the modulation amplitude is small compared with the FMR linewidth the resulting signal is the derivative of the absorption with respect to the dc field.

The choice of modulation frequency is governed by a number of factors. Since the noise contributed by the microwave detector (a diode in our experiments) decreases as the inverse of the frequency a higher modulation frequency usually results in a better signal to noise ratio. There are problems with high frequencies however which are discussed below.

The signal may be increased by placing the sample in a resonant cavity. For our experiments the sample formed part of the endwall of a cavity. The sensitivity of a cavity reflection system has been discussed by Feher[58]. A resonant cavity is the microwave analogue of a resonant LCR circuit. The cavity is characterized by a resonant frequency, f_o, and a quality factor, Q, which relates the energy stored in the cavity, E_{stored}, to the energy dissipated in one cycle:

$$Q = 2\pi\ E_{stored}/E \text{ dissipated in one cycle} \qquad (3.4)$$

Energy is dissipated in three ways: by resistive losses in the walls of the cavity, by absorption in the sample and by radiation through the hole used to couple microwaves into the cavity. The unloaded Q, Q_u, the external Q, Q_e and the loaded Q, Q_L are defined:

$$Q_u = 2\pi\ E_{stored}/(E_s + E_w) \qquad (3.5)$$

$$Q_e = 2\pi\, E_{stored}/E \text{ lost through coupling hole in one cycle}$$

$$1/Q_L = 1/Q_u + 1/Q_e$$

where E_w is the energy dissipated in the walls of the cavity in one cycle and E_s is the energy dissipated in the sample in one cycle. The loaded Q takes into consideration all the energy lost or dissipated. The energy stored in the cavity is:

$$E_{stored} = (1/8\pi)\int h^2 dV \tag{3.6}$$

where the integral is over the volume of the cavity and is evaluated at a time when the magnetic fields are at their maximum value (the electric fields are zero at this time). The energy absorbed in the walls of the cavity in one cycle is E_w:

$$E_w = (\delta_w/8)\int h_t^2 dS \tag{3.7}$$

where δ_w is the skin depth of the walls, the permeability of the walls is taken to be 1 and the integral is evaluated when the fields have their maximum value. In addition to the quality factors defined above it is convenient to define what may be called the sample Q, Q_s, and the filling factor, η:

$$Q_s = 2\pi\ E_{stored}/E \text{ dissipated in one cycle} \qquad (3.8)$$

$$= \int h^2 dV / \mathrm{Re}(\sqrt{-i\mu/2})\,\delta \int_{sample} h_t^2 dS$$

$$= 1/\mathrm{Re}(\sqrt{-i\mu/2})\,\eta$$

$$\eta = \delta \int_{sample} h_t^2 dS / \int h^2 dV$$

These integrals are straightforward to work out given the field distributions for the cavity mode of interest.

If microwave power P_o is incident on the cavity the power absorbed in the cavity, P_c, and the power reflected from the cavity, P_r, are determined by the coupling constant β:

$$\beta = Q_e/Q_u \qquad (3.9)$$

$$P_r/P_o = [(1-\beta)/(1+\beta)]^2$$

$$P_c/P_o = 4\beta/(1+\beta)^2$$

If β equals one the cavity is said to be 'critically coupled'. If the klystron frequency matches the resonant frequency of the cavity at critical coupling the reflected power is zero and all the incident power is dissipated in the sample and the cavity walls. If β is greater(less) than one the cavity is under(over)coupled.

Use of a cavity has two effects, the power absorbed by the sample may be increased, and the sensitivity, the ratio $\Delta P_r/P_r$,

is increased over that if no cavity is used.

The ratio of the energy absorbed in the sample to the total energy absorbed in the cavity (walls plus sample) is:

$$\frac{E_s}{E_w + E_s} = \frac{\delta \int_{sample} h_t^2 dS}{\delta_w \int_{walls} h_t^2 dS + \delta \int_{sample} h_t^2 dS} \qquad (3.10)$$

A very crude estimate of this ratio is the ratio of the area of the sample to the total wall area. Suppose the sample area was 1/30 the total wall area and that the coupling of the cavity was adjusted so that 2/3 of the incident power was absorbed in the cavity (a typical situation). The power absorbed by the sample would be approximately 1/45 of the incident power, a large increase over the power absorbed if the sample formed a short on the end of the waveguide (compare (3.2) above). If we wished to maximize the power absorbed by the sample we would use a critically coupled cavity, so that all the incident power was absorbed in the cavity, and make the area of the sample as large a fraction of the total wall area as possible. The Q of the cavity is irrelevant in maximizing the absorbed power.

The increase in sensitivity is a more important effect for reflection measurements. We assume for this discussion that the ratio of the energy dissipated in the sample to that dissipated in the walls is small. The change in absorption of the sample on sweeping through FMR has then only a small effect on the cavity Q. If the energy absorbed by the sample changes by an

amount ΔE_s the change in the unloaded Q is:

$$\Delta Q_u = (\partial Q_u/\partial E_s)\Delta E_s = -Q_u \Delta E_s/(E_w+E_s) \tag{3.11}$$

This change in Q produces a change in the power reflected from the cavity:

$$\begin{aligned} \Delta P_r &= (\partial P_r/\partial E_s)\Delta E_s \\ &= (\partial P_r/\partial \beta)\ (\partial \beta/\partial Q_u)\ (\partial Q_u/\partial E_s)\Delta E_s \\ &= -4\ \frac{(1-\beta)}{(1-\beta)^3}\ P_o\ \frac{-\beta}{Q_u}\ \frac{-Q_u}{E_w+E_s}\ \Delta E_s \end{aligned} \tag{3.12}$$

For a given ΔE_s the change in reflected power is a maximum if $\beta = 2\pm\sqrt{3}$, the plus(minus) sign corresponding to an under(over) coupled cavity. The sensitivity for the two couplings is the same. The maximum is fairly broad so that it is not necessary that β be exactly $2\pm\sqrt{3}$. It is clear that critical coupling ($\beta = 1$) must be avoided. With $\beta = 2\pm\sqrt{3}$ the power reflected from the cavity when $\Delta E_s = 0$ is 1/3 of the incident power. The change in reflected power if $\Delta E_s \neq 0$ is:

$$\Delta P_r = \pm 0.385 P_o (\Delta E_s)/(E_w+E_s) \tag{3.13}$$

The quantity $\Delta E_s/(E_w+E_s)$ may be related to the unloaded Q:

$$\frac{\Delta E_s}{E_w + E_s} \simeq \frac{\Delta E_s}{E_w} = \frac{1}{2\pi} \frac{\Delta E_s}{E_{stored}} \frac{2\pi E_{stored}}{E_w} = \frac{Q_u}{2\pi} \eta \mathrm{Re}(\sqrt{-i\mu/2}) \quad (3.14)$$

so that, at optimum coupling:

$$\Delta P_r/P_o = \pm(.385/2\pi) Q_u \eta \mathrm{Re}(\sqrt{-i\mu/2}) \quad (3.15)$$

where E_s has been neglected with respect to E_w. The sensitivity now involves a factor containing the unloaded Q of the cavity. Since values of the Q are typically several thousand this may provide a substantial increase in signal. Note that the filling factor, η, is important in determining the sensitivity. When comparing cavities resonating in different modes, for example a rectangular vs a cylindrical cavity, the filling factor must be considered. In other words the Q isn't everything. To maximize the sensitivity in reflection measurements we would choose a cavity with as high a combination of filling factor and Q as possible, coupled so that 1/3 of the incident power is reflected.

This analysis holds only if the fraction of the power absorbed by the sample is small in which case the power reflected from the cavity varies linearly with the change in absorption of the sample. If the change in power absorbed by the sample is an appreciable fraction of the total power absorbed in the cavity the reflected power no longer varies directly with the absorption of the sample. The sample is said

to load the cavity. If the loading is severe the FMR lineshape will be distorted.

The resonant frequency of the cavity is shifted by the absorption and by the reactive component of the surface impedance of the sample. In an absorption experiment we are interested in the changes in power reflected from the cavity due to the change in the cavity Q not those due to change in the cavity frequency relative to the klystron frequency. The klystron frequency is usually locked to the cavity resonant frequency. The klystron frequency can be modulated by applying a small alternating voltage on top of the dc klystron reflector voltage. The amplitude and phase of the component of the signal reflected from the cavity at the modulation frequency depend on the difference between the klystron center frequency and the cavity frequency because at resonance there is a decrease in the power reflected from the cavity. For small differences the amplitude is directly proportional to the difference. Using a lock-in amplifier this component may be detected and used to generate a dc voltage which is fed back to the klystron reflector so that the klystron frequency follows the cavity frequency.

The sample forms part of the cavity endwall. Since microwave currents flow across the junction between the cavity and the sample good electrical contact is essential to avoid distorting the cavity mode. Poor contact reduces the cavity Q and changes the resonant frequency and the coupling. These

changes may depend on the external field due to the changing surface impedance of the sample. Therefore when FMR is measured with a poor contact the lineshape may be badly distorted.

The energy dissipated in the cavity depends on the electrical conductivity of the walls. The conductivity increases with decreasing temperature leading to a higher Q, a higher resonant frequency and different coupling. Usually it is necessary to use a tuning rod, a piece of quartz for example, which lowers the resonant frequency when inserted into the cavity, to ensure that the cavity resonant frequency does not escape the frequency range of the klystron. The cavity frequency also shifts when the cavity is evacuated, due to the dielectric constant of air. In our experiments these shifts were of the order of a tenth of a gigahertz.

As stated above the field modulation technique yields the derivative of the absorption. For very broad lines, such as those for Nickel at low temperatures, the sensitivity of this technique is small. The amplitude of the extrema of the absorption derivative varies as $(\Delta H)^{-1.5}$ so for a constant modulation amplitude the signal would decrease in the same manner. In our case it became necessary to measure the absorption directly. We used a bolometer to measure the temperature of the sample. The use of a bolometer in magnetic resonance measurements has been discussed by Schmidt and Solomon[59] and by Cochran, Heinrich and Dewar[60]. The field modulation and bolometric systems used in our experiments are

described in Section 3.5.

3.4 The Cavity and the Sample Holder

The Cavity

The microwave resonant cavity which was used in these experiments is sketched in Figure 3.1(a). The cavity consisted of two parts: the main body, which was basically a metal bucket, and an endwall which was clamped over the open end of the cavity. The endwall is sketched in Figure 3.1(b) and is described below. The cavity dimensions were 14 mm deep and 16.3 mm inside diameter. The thickness of the upper end, the end with the coupling hole, was 0.020 inches.

The cavity resonated in the TE_{112} cylindrical cavity mode. The field distributions for this mode are shown in Figure 3.2. The cylindrical TE_{11} waveguide mode is the dominant mode for a cylindrical geometry, the cutoff wavelength being 3.413 times the cylinder radius. This mode is similar to the rectangular TE_{10} waveguide mode and may be derived from the rectangular mode by a distortion of the rectangular guide to a cylindrical shape.

The cavity was coupled to the waveguide through the upper endwall and the cavity was oriented so that the sample was in a horizontal plane. The angle between the sample normal and the vertical was less than 1°.

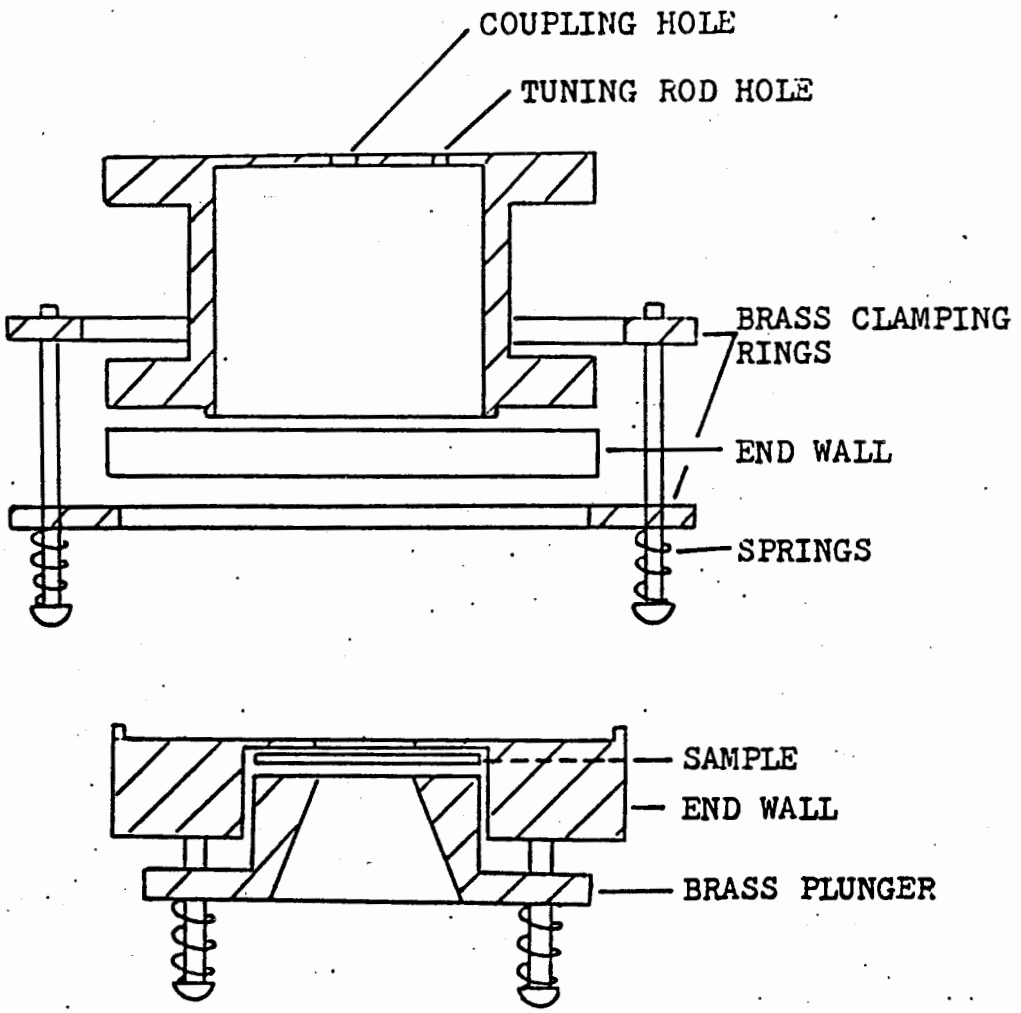

Figure 3.1 The 24 GHz microwave cavity (a) and the sample holder (b).

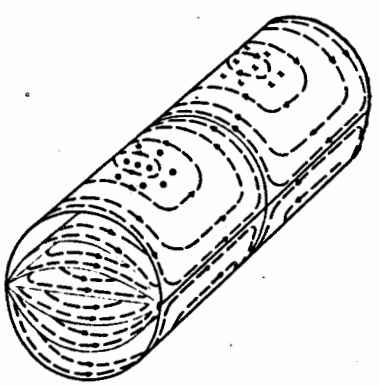

Figure 3.2 Field configurations for the TE_{112} cylindrical cavity mode. The dashed lines represent the microwave magnetic field and the dots and crosses represent the microwave electric field.

The cavity was designed for a high frequency modulation system. For this purpose it was desired to use a material with a poor electrical conductivity which would not shield the modulation field. The material used was a 30% Ni-70% Cu alloy which has a room temperature resistivity of approximately 40×10^{-6} Ωcm which is essentially temperature independent. To improve the Q the cavity was polished with diamond polish and plated with a layer of gold several microwave skin depths thick. Since the high frequency modulation did not work well, however, the use of a poor conductivity material for the cavity was not important.

The cavity coupling was adjusted to give nearly maximum sensitivity in reflection. As pointed out above this is not a critical adjustment. However care must be taken to avoid the condition corresponding to critical coupling. Critical coupling may accidentally occur if the cavity is undercoupled at room temperature and if the Q increases upon cooling. The resonant frequency at room temperature was near 23.95 GHz. The loaded Q was approximately 3500. All of these quantities depended on the quality of the contact established between the endwall and the cavity. Before making a measurement the clamping bolts were adjusted to obtain the maximum loaded Q. The cavity frequency could be varied by means of a quartz tuning rod driven vertically into the cavity by a micrometer drive mounted on the upper flange (see Figure 3.4).

The Sample Holder

To measure FMR it is necessary to hold the sample in a fixed orientation with respect to the applied field. The magnetocrystalline anisotropy becomes large in Nickel at low temperatures, the first MCA constant increasing from a room temperature value of -0.59×10^5 erg/cm^3 to -12.9×10^5 erg/cm^3 at 4.2 K. This corresponds to an effective field of approximately 2.5 kOe at 4.2 K. If the applied field is not parallel to an easy axis ((111) direction) large torques arise which tend to rotate the sample until an easy axis is parallel to the field. If the sample is prevented from rotating by being glued or soldered to a substrate the strain resulting from the differential thermal contraction of the sample and the substrate leads, through magnetostriction, to shifts in the position of FMR and may lead to broadening of the line. The mounting of the sample is thus of critical importance for low temperature measurements.

Our solution to this problem is shown in Figure 3.1(b). The sample was held in a demountable endwall assembly which was clamped over the open end of the cavity. The endwall was a circular piece of copper 1/4 inch thick. The surface forming part of the cavity was gold plated. The center of the endwall was machined to 0.020 inches thick to accommodate the sample. The center of the sample was exposed to the microwaves through a hole 7 mm in diameter. The sample was lightly pushed against

this wall by a brass plunger attached to the endwall. Springs were placed on the bolts holding the plunger to the endwall to avoid having the pressure on the sample vary with temperature due to the thermal contraction of the various pieces. These springs were wound from phosphor bronze wire. The plunger had a hole in it to allow access to the back of the sample for the measurements made with the bolometer (Section 3.5).

The endwall was clamped to the cavity using the two rings shown in the figure. The bolts used here were also spring loaded. The endwall assembly could be rotated on the cavity; thus rotating the sample in order to measure FMR along each of the three principal axes was straightforward and meant that the sample mounting remained unchanged between coolings to 4.2 K. The endwall also fitted a cavity which was part of a 9.5 GHz system so that measurements could be made at the two frequencies without having to remount the sample.

3.5 The 24 GHz Microwave System

A schematic drawing of the 24 GHz system is shown in Figure 3.3. The part of the system to the left of the vertical dashed line in the Figure was part of a microwave transmission system which has been described in detail[60], with the addition of the electronic switch. Apart from the klystron and the klystron power supply all the microwave components were the same as those described in that paper. The reader is referred to that paper

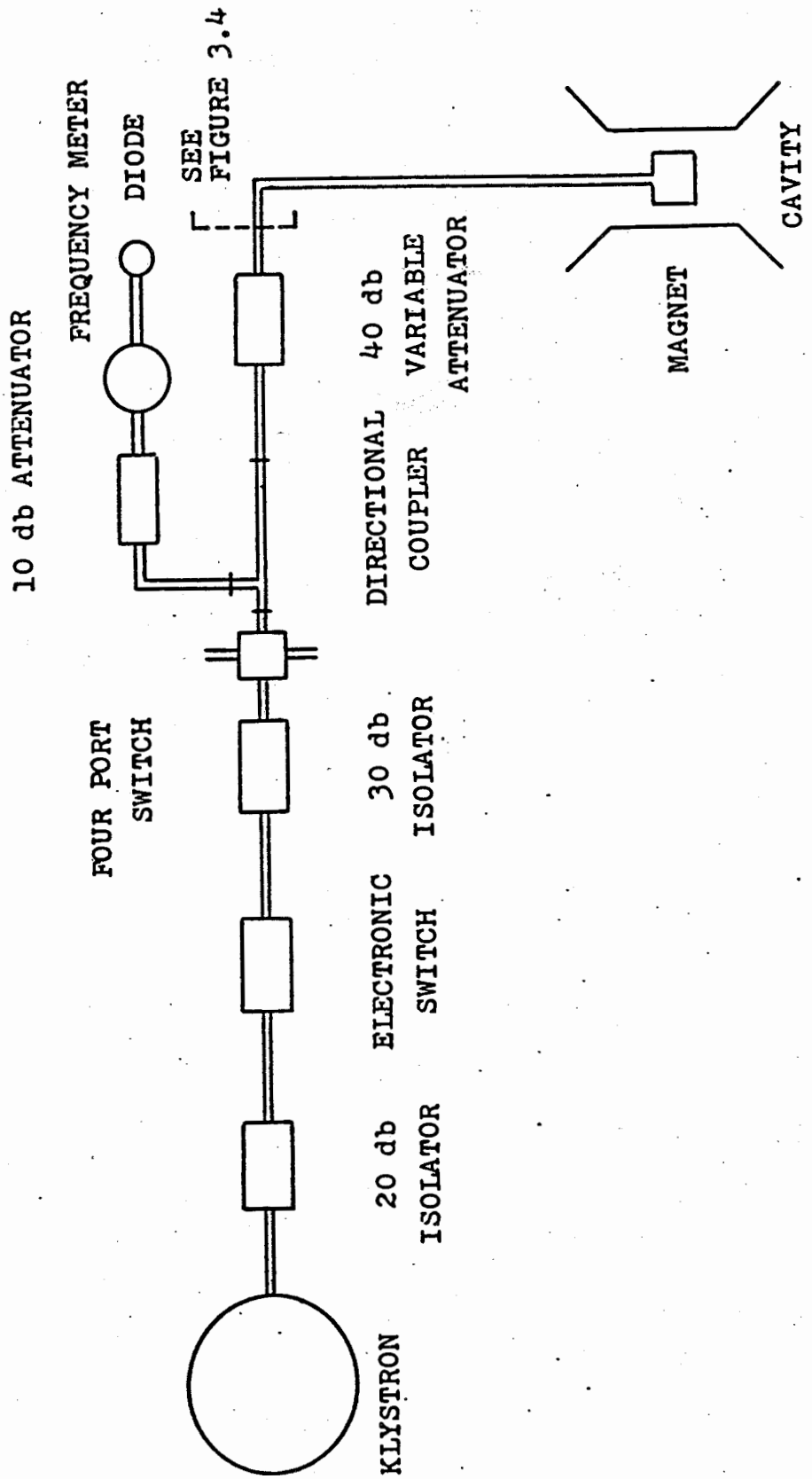

Figure 3.3 Schematic drawing of the 24 GHz microwave system.

if more information is required.

The components were mounted on a table approximately 2 m high from which the resonant cavity was suspended in the magnet gap. The magnet was mounted on rails and could be moved to allow easy access to the cavity. For low temperature measurements a stainless steel liquid helium dewar was placed around the cavity and bolted to a flange on the table.

The magnet was a Varian V-3800 electromagnet having a 3 1/2 inch gap. Fields up to 16 kOe could be obtained. A Bell 810 Field Meter was used to provide a signal proportional to the value of the field. The field values were calibrated with an NMR system[61]. In addition to being mounted on rails the magnet yoke could be rotated about a vertical axis.

Microwaves were generated by a Varian klystron (type VA 282 EY) driven by a PRD Electronics Inc Type 819-A Universal Klystron Power Supply. The klystron operated in a frequency range 23.8 to 24.0 GHz with an output power of 300 mW. The klystron frequency was locked to the resonant frequency of the microwave cavity as described above.

The electronic switch was used to amplitude modulate the microwave power for measurements made with the bolometer (see below). The four port switch was not essential for the FMR measurements but was useful for diverting the microwaves when changing the sample. The signal reflected from the cavity was detected by the microwave diode attached to the directional coupler. The diode mount was electrically isolated from the

microwave track by placing a mica gasket between the waveguide flanges and using nylon bolts. This overcame problems with ground loops. The microwave frequency could be measured with an accuracy of .005 GHz by means of a Hewlett Packard K532A frequency meter. The variable attenuator served to vary the power incident on the cavity.

The part of the system to the right of the dashed line in Figure 3.3 is shown in Figure 3.4. This part of the system was designed specifically for these experiments. A vacuum seal consisting of a mica gasket and a Viton O-ring was placed between the microwave flanges above the upper flange. A length of stainless steel waveguide between the upper flange and the cavity provided for thermal isolation of the cavity. The copper-stainless steel waveguide joint was made by milling out the inside of a portion of the copper waveguide and soldering the stainless guide to it.

The cavity was bolted to a flat flange at the end of the guide, and could be easily removed for changing samples and mounting the bolometer. A stainless steel can, 2 inches in diameter, could be attached to the lower flange to isolate the cavity for low temperature measurements. This can could be evacuated through the stainless steel tube shown in the figure. The tuning rod for the cavity and wires were brought into the can through this tube. Two additional vacuum feedthroughs were placed in the lower flange. A heater resistor was attached to the waveguide above the cavity to allow one to vary the

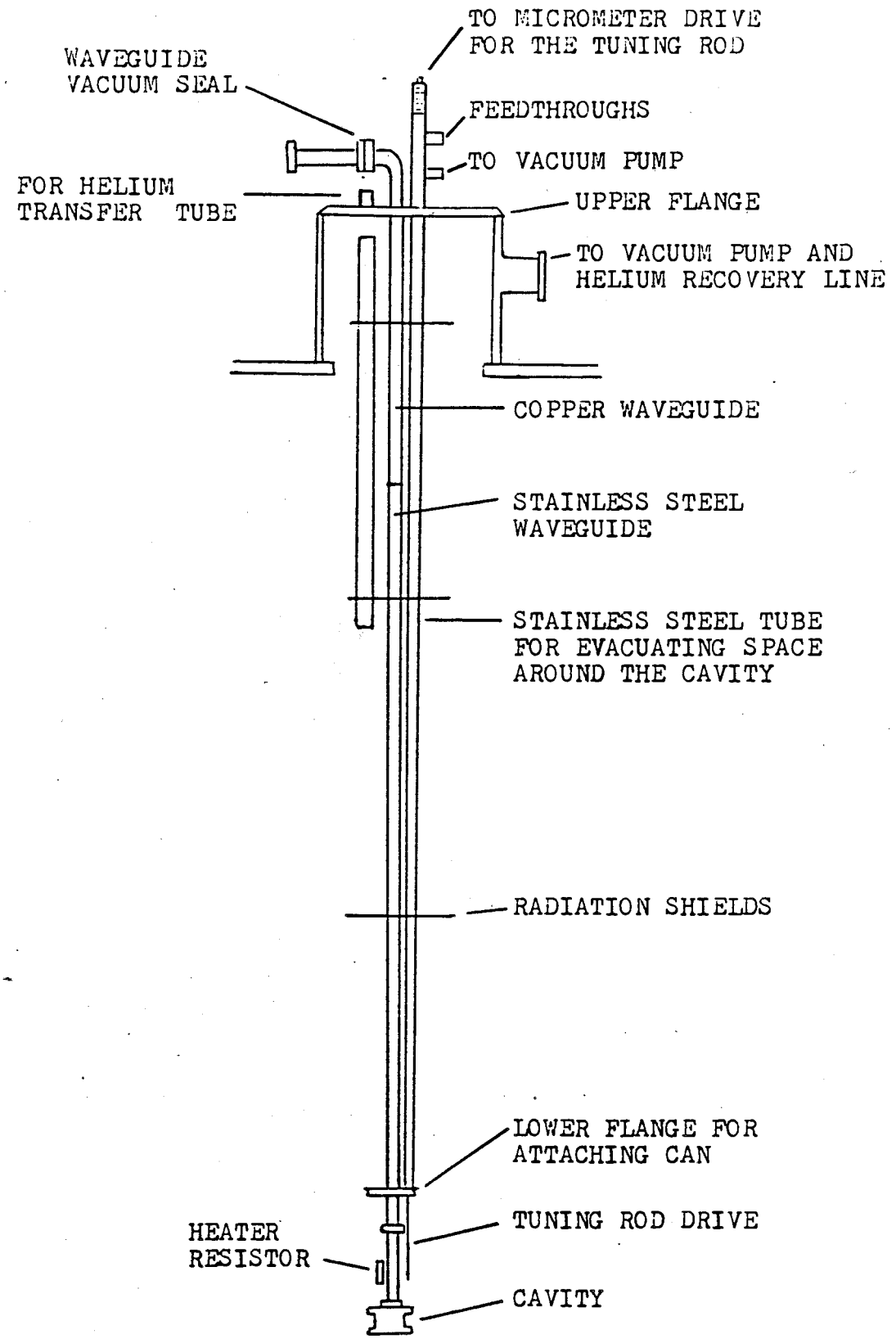

Figure 3.4 Part of the 24 GHz microwave system.

temperature of the cavity.

Temperatures were measured using a copper constantan thermocouple and using a carbon glass resistance thermometer attached to the cavity endwall. The resistance of the carbon glass thermometer was measured by means of a Keithley digital multimeter in four-wire mode or with an SHE Conductance Bridge. A calibration table was supplied by the manufacturer.

Measurements between 4.2 K and approximately 60 K were made on the fly as the system warmed from 4.2 K. At 60 K measurements were made by pumping on liquid nitrogen around the can. Temperatures above 77 K could be held constant by means of a controller which regulated the current through the heater resistor in order to maintain a constant signal from the thermocouple. The controller kept the temperature constant to better than 0.5 K. Since both the magnetocrystalline anisotropy, which shifts the position of the resonance, and the damping are strong functions of temperature between 4.2 K and room temperature it is essential that the temperature be held constant. For example the effective magnetocrystalline anisotropy field, $2|K1|/M_s$, changes by approximately 12 Oe per degree at 200 K and by approximately 24 Oe per degree at 100 K. The linewidth changes by approximately 12 Oe per degree at 77 K.

For temperatures accesible using liquid nitrogen, down to approximately 60 K by pumping on the liquid, low frequency ($\simeq$100 Hz) field modulation was used. No signal could be observed at 4.2 K using this technique. An attempt was made to

use high frequency modulation but this was unsuccessful (see below). For the 4.2 K measurements we used a bolometer to detect the absorption directly.

The dc voltage across the microwave diode was monitored in all measurements made. FMR was observed as a change in the dc level. The variation with the external field could be traced on an X-Y recorder and was used to determine whether the sample was loading the cavity. The signal could be used to find the resonance field H_{fmr}, but it was too noisy to yield reliable values of the FMR linewidth.

Low Frequency Modulation

A pair of Helmholtz coils, approximately 30 cm in diameter, were mounted on the pole pieces of the magnet. These were driven by the reference channel of a PAR 124 lock-in amplifier, amplified by a Kepco Bipolar Operational Power Supply/Amplifier. These coils produced a field of approximately 1 Oe per volt of driving at 100 Hz in an empty gap. The Kepco power supply could deliver 75 volts. The field amplitude at the sample was less than 1 Oe/volt because of screening of the field by eddy currents in the cavity walls and in the dewar. The dewar contained a liquid nitrogen cooled copper shield around the helium pot so the screening became appreciable at low temperatures, even at a frequency of 100 Hz.

The voltage from the microwave diode was fed to the lock-in amplifier. The output from the lock-in amplifier went to the Y-channel of an X-Y recorder. The input to the X-channel was obtained from a Hall probe which provided a voltage proportional to the external field. Since a field modulation technique yields the derivative of the absorption with respect to the external field the linewidth, defined as the field interval between extrema of the derivative, and the resonance field, the zero crossing of the derivative, could be read directly from the X-Y recorder trace. Traces were taken at least twice, sweeping in the direction of both increasing and decreasing values of the external field, in order to check reproducibility and in order to check that the field sweep rate was sufficiently slow compared with the lock-in amplifier time constant so that the absorption line was not distorted by too fast a sweep rate.

High Frequency Modulation

The signal to noise ratio in a field modulation system may be improved by using a higher modulation frequency as the noise contributed by the detector varies approximately inversely with the frequency. The use of high frequency modulation is attended with problems. The modulation field must penetrate to the inside of the cavity, however the penetration decreases with increasing frequency. The current must be increased,or the modulation coils placed close to the sample, to achieve the same

modulation amplitude at a high frequency as at low frequencies. Since the skin depth decreases with increasing conductivity the problem becomes more severe at low temperatures. Eddy currents are induced in the cavity walls and in the sample by the modulation field. The interaction between these eddy currents and the external field causes the walls and the sample to vibrate. Essentially, the resonant frequency of the cavity is modulated. This gives rise to a signal in the reflected microwaves at the modulation frequency proportional to the strength of the external field. This field dependent background may become large and obscure the FMR signal. Heating due to the eddy currents may result in the temperature of the sample drifting with time or it may result in excessive boil-off of liquid Helium. Due to these problems we were unable to construct a high frequency modulation system which worked as well as the low frequency modulation system.

The Bolometer

A bolometer is a chunk of material whose electrical resistivity depends in some known way on its temperature. The temperature of the sample increases slightly with the power absorbed. The change in temperature can be detected by measuring the resistance of a bolometer attached to the sample.

The bolometer which was used was purchased from Infrared

Laboratories Inc†. It is sketched in Figure 3.5. A piece of Germanium approximately 0.4 mm square was attached to Indium blobs on a sapphire substrate. Brass leads were attached to the Indium in order to measure the bolometer resistance. In operation the sapphire substrate was attached to the ferromagnetic sample (see below). The bolometer resistance was 15 Ω at room temperature, approximately 400 Ω at 12 K, 210 KΩ at 4.4 K and 250 KΩ at 4.2 K. The change in resistance on a sweep through FMR was approximately 1 KΩ, small enough so that the dependence of the resistance on temperature was essentially linear.

The bolometer was placed in series with a 9 volt battery and a 1.5 MΩ resistor. The microwave power was chopped with the electronic switch (see Figure 3.3). A chopping frequency of 80 Hz worked well. The chopper was driven by the reference channel of a PAR 124 lock-in amplifier and the voltage across the bolometer provided the input to the lock-in amplifier. The signal was observed at the chopping frequency. The amplifier output went to the Y-channel of an X-Y recorder and to a data-acquisition system where the data was stored in digital form. The data could be transferred to the main SFU computer for analysis (see Chapter 4). The program used in the data acquisition required a zero level for scaling the data. This was provided by shorting the input to the lock-in amplifier

---

†Infrared Laboratories Inc, 1808 E 17th St, Tucson Arizona, 85719

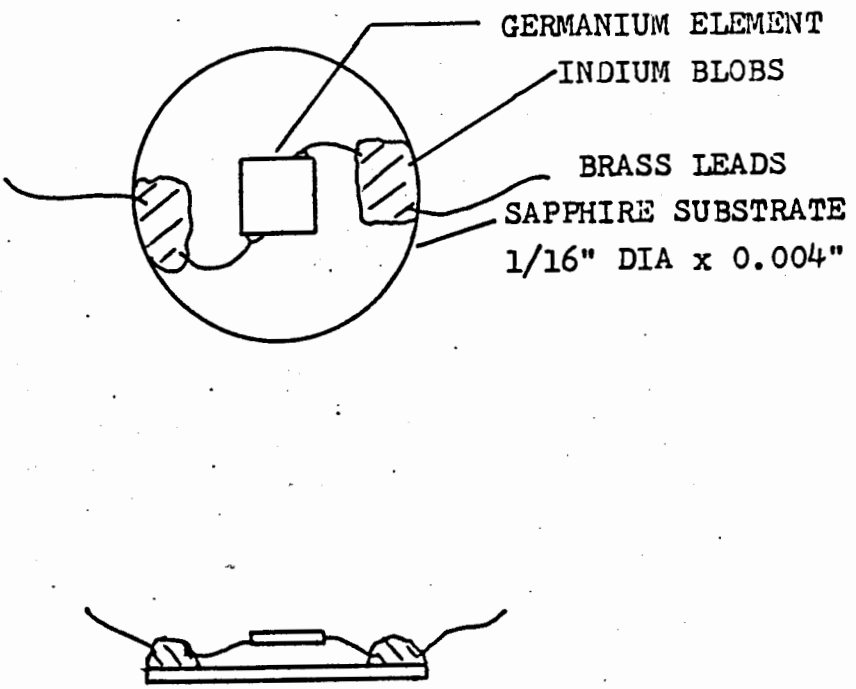

Figure 3.5 The bolometer which was used for the 4.2 K measurements, approximate scale 1 inch = 1 mm.

(equivalent to turning off the microwave power). The program then scaled the data so that the maximum signal was 1.

The power reflected from the cavity was monitored using the microwave diode to determine the variation of the power reflected from the cavity. The reflected power, and hence the power in the cavity, changed by less than 0.7% during a field sweep. Since this power variation was so small the differential technique of Cochran et al[60] using two bolometers was not needed.

The procedure for making a measurement was as follows. The sample was placed in the endwall assembly, the endwall attached to the cavity and the sample orientation determined by measuring the angular variation of the resonance field. When the desired crystal axis was located the endwall was rotated until that axis was parallel to the applied field when the applied and microwave magnetic fields were perpendicular. The cavity was removed from the waveguide and the bolometer attached to the back of the sample with dilute GE 7031 adhesive. The cavity was reattached to the waveguide, the stainless steel can flushed with Helium gas and attached to the the lower flange and precooling started. The can was not evacuated until the temperature fell to approximately 120 K in order to avoid drying out the adhesive. It was desirable that the adhesive remain semi-fluid during cooling so as not to strain the specimen. The Helium transfer was then started.

The pressure of Helium gas in the can while using the bolometer was critical for reproducible results. It appears that the thermal contact with the liquid Helium bath provided by the gas is an important effect. Best results were obtained with a pressure of approximately 1 torr. The system usually worked well although there were occasional drifts with time and sudden jumps in the signal level that remain unexplained. A sufficient length of time spent fiddling with the pressure in the can usually cured these problems. A second reference bolometer would have been of great help in order to extract the sample signal from these background noises.

Several field sweeps were made, in the direction of both increasing and decreasing field, to check reproducibility. When the system was working properly the reproducibility was good.

In the early experiments with the bolometer the bolometer was left attached to the sample(sample 1) for four successive coolings to 4.2 K. Upon removal of the sample from the endwall assembly a small dimple was noted where the bolometer had been attached. For all subsequent measurements the bolometer was removed and reattached between coolings. Measurements on the dimpled sample were in agreement with those on an undimpled sample(sample 2). For sample 2 measurements were made at room temperature and at 77 K before attaching the bolometer. The 4.2 K measurements were then made and the room temperature and 77 K measurements repeated. The results before and after cooling to 4.2 K were the same. We conclude that the attachment

of the bolometer to the sample did not produce any strain in the sample which would have led to shifts or broadening of the FMR line.

3.6 Measurements at other Frequencies

Measurements were made at 9.1, 34.7 and 73.0 GHz at room temperature and at 9.5 GHz at 4.2 K in addition to the measurements at 24 GHz. The 9.5 GHz system was identical to the 24 GHz system except that a circulator was used to separate the reflected microwaves from the incident microwave power instead of a directional coupler. The cavity was of the same construction as the 24 GHz cavity, although of a different size of course, and resonated in the same mode (TE_{112}). As mentioned in Section 3.3 the sample mount fitted both the 9.5 and 24 GHz cavities so that measurements could be made at both frequencies without having to remount the sample.

Room temperature measurements at frequencies other than 24 GHz were made without resonant cavities. The sample formed part of a termination at the end of a piece of waveguide. A circular area 3 mm in diameter was exposed through a 0.005 inch thick copper diaphragm for the 9.1 and 34.7 GHz measurements. The sample was placed directly across the waveguide (2 mm x 3.5 mm) at 73 GHz. Field modulation at a frequency near 20 KHz was provided by a wire passing directly underneath the sample.

4. EXPERIMENTAL RESULTS AND DISCUSSION

4.1 Introduction

In this chapter we present and discuss our experimental results. The measurements were made primarily to investigate the magnetic damping in Nickel at low temperatures. There are two main thrusts to our work. First, we wish to determine whether or not the FMR linewidth, ΔH, is different with the applied field parallel to each of the three principal crystal axes at low temperatures. Second, we are interested in the information about the damping processes that can be obtained by comparing the experimental FMR line widths, positions and shapes with widths, positions and shapes calculated using computer programs based on the calculations outlined in Chapter 2.

We have made measurements on two samples cut from the same boule of Nickel and prepared in the same way. FMR was measured with the applied field in the sample plane and along each of the three principal axes at 23.95 GHz at room temperature and from 4.2 to 200 K. As stated in Chapter 3 we were unable to obtain values for the FMR linewidth between 4.2 and approximately 60 K. The variation of the resonance field, H_{fmr}, with the direction of the applied field in the sample plane, for directions in addition to the three principal axes, was measured at room temperature, 77 K and 4.2 K. The angular variation of the

linewidth was measured at 77 K. Also, the frequency dependence of FMR was measured at room temperature for Sample 2. A measurement was made at 9.5 GHz at 4.2 K, but no other measurements were made at other frequencies at temperatures other than room temperature. Low temperature systems were not available for frequencies other than 9.5 and 23.95 GHz. At 9.5 GHz the magnetocrystalline anisotropy shifts mean that FMR can be observed only for the (100) direction. The results are presented in the following Sections: room temperature results in Section 4.2; 77 K results in Section 4.3; 4.2 K results in Section 4.4; and in Section 4.5 the measurements made at intermediate temperatures. We discuss the results briefly in each Section but postpone a more comprehensive discussion until Section 4.6.

Before presenting the results it is worthwhile to summarize the calculations available for comparison with experiment. If damping and exchange are neglected FMR occurs at the field where the permeability becomes infinite. From Chapter 2 this is when:

$$(\omega/\gamma)^2 = (H_0+H_d+a)(H_0+H_d+4\pi M_s+\gamma) \qquad (4.1)$$

where a and γ are effective MCA fields, see Table 2-1 and equations (2.57). H_0 is the applied field and H_d is the demagnetizing field. The value of the applied field which satisfies this relation will be referred to as the 'no-exchange no-damping' value of the resonance field. The experimental

value of the resonance field will differ from this value of course, because of the shifts due to damping and exchange. We will be interested in comparing the experimental resonance fields with calculated resonance fields and in such a comparison this no-exchange no-damping value forms a useful reference point.

Three computer programs incorporating different options were used for calculating the absorption and the absorption derivative. The first program, to be referred to as program I, used a local conductivity, exchange, wavenumber independent Gilbert damping and magnetocrystalline anisotropy (MCA). In this program it was assumed that the applied field was parallel to a crystal axis and that the magnetization was parallel to the applied field. This calculation was outlined in Section 2.2. The second program, which will be referred to as program II, used a local conductivity, Gilbert damping and neglected exchange. The absorption was calculated for arbitrary orientation of the applied field with respect to the sample plane and the crystal axes and allowed for the lack of alignment between the magnetization and the applied field. Exchange was neglected because the calculation becomes quite complicated and exchange is a comparatively small effect in Nickel. This program was used primarily to determine the effect on the resonance line of misalignment between the applied field and a crystal axis. It was also useful for calculating the variation of the resonance field with the direction of the applied field

in the sample plane. This calculation was outlined in Section 2.3. The third program, which will be referred to as program III, assumed, as in program I, that the applied field was parallel to a crystal axis and that the magnetization was parallel to the applied field. Exchange and MCA were included. The program incorporated the option of a local or a non-local conductivity and a wavenumber dependent or independent Gilbert damping. This calculation was outlined in Section 2.4. The program used a Fourier sum to evaluate the absorption and absorption derivative. The results of this program agreed with those of programs I and II in the limits where they could be compared of course. This is the program which was used for most of the discussion which follows.

Material Parameters for Nickel

A large number of factors enter these calculations which serve to determine the experimentally observed quantities. These include the saturation magnetization, the g-factor, the exchange constant, the dc conductivity and its dependence on wavenumber, the damping parameter and its dependence on wavenumber, and the magnetocrystalline anisotropy constants. In addition the microwave frequency, the sample size and shape, the direction of the applied field with respect to the crystal axes, and the temperature all have profound effects. In principle it is possible to obtain values for many of the material parameters

entering FMR from the FMR measurements. Our interest is primarily in the damping and so we take values for most of the parameters from the literature. It is convenient to collect the parameters which we will use in our discussion in one place. The parameters used in the calculations at room temperature, 77 and 4.2 K are listed in Table 4-1. The values of the saturation magnetization were taken from the work of Kaul and Thompson[62] and Danan, Herr and Meyer[63]. The resistivity ratio at 4.2 K was measured on Sample 1, and was found to be ρ_{295}/ρ_4=38. The resistivity at any temperature was assumed to be given by the sum of a constant residual resistivity and the resistivity that would be observed in an ideally pure Nickel sample[64,65,66]. The values of the conduction electron relaxation time τ enter the calculations made using a non-local conductivity. Following Cochran and Heinrich[37] we have assumed a room temperature value of 10^{-14} sec and a value for the Fermi velocity v_F = 2.5×10^7 cm/sec. These correspond to a room temperature mean free path, $l = v_F\tau$, of 25 A. These values were extracted from the low temperature cyclotron resonance data for s-p band belly orbits as reported by Goy and Grimes[68]. This relaxation time varied with temperature in the same way as the dc electrical conductivity. The values of the damping parameter are listed for comparison purposes as we will vary the damping parameter when comparing calculations with experiment. The room temperature value is that of Dewar, Heinrich and Cochran[38] while the low temperature values are taken from the work of

TABLE 4-1

Nickel Parameters

	295 K	77 K	4.2 K
$4\pi M_s$(kG)[62,63]	6.16	6.60	6.60
$\rho(\Omega cm)$[64,65,66]	7.2×10^{-6}	$.72\times10^{-6}$	$.19\times10^{-6}$
ρ_{295}/ρ_4	1	10	38
τ(sec)[37]	10^{-14}	10^{-13}	3.8×10^{-13}
G(sec^{-1})[38,13]	2.45×10^{8}	6.3×10^{8}	14×10^{8}
K1(erg/cm^3)[67,21]	-0.59×10^{5}	-8.45×10^{5}	-12.92×10^{5}
K2(erg/cm^3)[67,21]	-0.25×10^{5}	0.96×10^{5}	4.79×10^{5}
K3(erg/cm^3)[67,21]	0	-1.43×10^{5}	0.80×10^{5}

$B = 7.4\times10^{5}$ erg/cm^3; $\phi_o = 17°$; $5B\phi_o^3/M_s = 180$ Oe

$K1' = K1 + 5B\phi_o^3/2 = -12.44\times10^{5}$ erg/cm^3[21]

Temperature Independent Parameters:

$g = 2.187$[38]

$\omega/\gamma = 7.82$ kOe at f = 23.95 GHz

$A = 1.0\times10^{-6}$ erg/cm[38,13]

$v_F = 2.5\times10^{7}$ cm/sec[37]

Demagnetizing field $H_d = 30$ Oe

Bhagat and Lubitz[13]. The numbers were taken from Figure 16 of [13](an enlarged version of Figure 6 of [12]). These are actually values of the Landau-Lifshitz damping parameter, but, as pointed out in Chapter 2, the difference between the Landau-Lifshitz and Gilbert damping parameters is small.

The value of the g-factor is due to Dewar, Heinrich and Cochran[38] and was derived from FMAR transmission measurements. The values of g quoted by different authors[24,38] are independent of temperature. The exchange constant is that used by Cochran, Heinrich and Dewar[48] and Bhagat and Lubitz[13]. The Fermi velocity was discussed above. The demagnetizing field was calculated using the formula of Kraus and Frait[42], equation (2.5). A temperature independent value of 30 Oe was used. The demagnetizing field shifts the resonance but has no effect on the FMR lineshape if the applied field is in the sample plane.

The MCA constants listed in the Table are those of Tokunaga[67] at room temperature and Tung, Said and Everett[21] at 77 and 4.2 K. The room temperature MCA constants of Tokunaga are in good agreement with those of Franse[28]. In the past there has been wild disagreement about the values of the MCA constants, particularly the higher order constants K2 and K3 at low temperatures[28]. However some accord seems to have been reached. The constants of Tung et al at 4.2 K are in good agreement with those obtained by Gersdorf[44] from the torque measurements of Aubert et al[43]. The constants of Tung et al at 77 K are in good agreement with those of Franse[28]. However Tokunaga's constants at these two temperatures do not agree with these values. For example at 77 K Tokunaga has $K2 = -1.4 \times 10^5$ erg/cm^3 and $K3 = .28 \times 10^5$ erg/cm^3 which are of the same order of magnitude but have opposite signs to the constants

of Tung et al and of Franse. At 4.2 K Tokunaga has $K2 = 2.0 \times 10^5$ erg/cm^3 and $K3 = 3.3 \times 10^5$ erg/cm^3 which have the same sign as the constants of Tung et al. These differences are important because the calculated values of the resonance field will be shifted depending on which MCA constants are used.

At intermediate temperatures the only data available is that of Tokunaga[67]. Since these constants do not agree with those of Tung et al at 77 K we will be careful in the conclusions we draw from their use.

At 4.2 K there is an additional contribution to the MCA which has been ascribed to the presence of a small piece of Fermi surface, the X_2 hole pocket, which exists only when the magnetization is within an angle ϕ_0 of a (100) direction. Gersdorf[44] has suggested that the extra free energy contributed by this piece of Fermi surface is:

$$E(\phi) = -B(\phi_0^2 - \phi^2)^{5/2}$$

if the angle, between the magnetization and a (100) direction, ϕ, is less than ϕ_0 and zero otherwise. This additional energy produces a torque which enters the effective MCA fields a and γ. If the magnetization is parallel to a (100) direction the effective MCA fields are (compare Table 2-1):

$$a = \gamma = 2K1/M_S + 5B\phi_0^3/M_S = 2K1'/M_S$$

where $K1' = K1 + 5B\phi_0^3/2$. This result is obtained by taking the second derivative $\partial^2 E/\partial\phi^2$ evaluated at $\phi = 0$. The effective MCA fields for the (111) and (110) directions are not changed since the X_2 pocket does not exist if the magnetization points along a (111) or a (110) direction. The values of $K1'$ and $5B\phi_0^3/M_s$ are listed in the Table using the values of Tung et al for B and ϕ_0. These are in good agreement with Gersdorf's values for these parameters. The effect of this extra MCA torque is to shift the position of the (100) resonance some 200 Oe to lower fields. Although the suggested presence of the X_2 pocket has resolved problems with the description of MCA in Nickel at 4.2 K, the actual existence of the pocket is still not a certainty. For example it has not been observed in de Haas van Alphen experiments[69]. It should be pointed out that the MCA torques for the three principal axes at 4.2 K may be calculated directly from the Fourier coefficients of the torque curves given by Aubert et al[43]. The values of α and γ obtained in this manner agree closely with those obtained using the MCA constants of Tung et al and of Gersdorf, as they should since Gersdorf used Aubert's numbers to obtain his MCA constants.

Gersdorf and Tung et al quote values for K4 at 4.2 K which do not agree at all. Since K4 has only a small effect on the position of FMR we have neglected it in our calculations.

4.2 Room Temperature Results

For measurements at temperatures above 60 K FMR was measured using a field modulation technique, see Chapter 3. The result of an experiment was an X-Y recorder trace of a signal proportional to the derivative of the power absorbed by the sample as a function of the applied field. The linewidth, ΔH, was measured directly from the recorder trace as the field interval between the extrema of the derivative. The resonance field, H_{fmr}, was measured as the zero crossing of the derivative. FMR was also measured by monitoring the dc voltage across the microwave diode which provided a signal proportional to the absorbed power. The resonance field could be obtained from the maximum of this absorption signal.

The experimental values of the resonance field and the linewidth for the two samples at room temperature and at 23.95 GHz are listed in Table 4-2, along with the no-exchange no-damping values of H_{fmr}. The results for the two samples are generally in good agreement although the (110) linewidth for sample 2 is larger than the other measured linewidths.

The Frequency Dependence of FMR

The linewidth calculated using program I with $G = 2.45 \times 10^8$ sec^{-1} at 23.95 GHz is 320 Oe. This is the linewidth expected for a sample in which the linewidth was due

TABLE 4-2

Results for room temperature, 23.95 GHz.

		[100]	[110]	[111]
H_{fmr}(kOe)	Sample 1	5.58±0.02	5.35	5.14
	Sample 2	5.58	5.34	5.14
	Calc.	5.60	5.38	5.17
ΔH(Oe)	Sample 1	350±30	365	360
	Sample 2	340	380	360

Calc: No-exchange, no-damping value of H_{fmr}.
In this and all subsequent Tables the quoted experimental uncertainties apply to all entries in the Table.

---

only to the intrinsic damping and the exchange conductivity with no surface anisotropy. The average linewidth we have measured at this frequency is 360 Oe which is 40 Oe larger than the 'ideal linewidth' of 320 Oe. The linewidth measured in an FMR experiment may be increased over the ideal linewidth because of, for example, strain in the sample, inhomogeneities, impurities, surface roughness or polycrystallinity. The mechanism may be spin-pinning, described by a surface anisotropy energy, two-magnon scattering, or the sample may see an inhomogeneous applied field because of, say, surface irregularities. Measurement of the frequency dependence of the linewidth provides a way of sorting out some of these non-intrinsic contributions to the linewidth. We have measured FMR at frequencies of 9.115, 34.7 and 73 GHz in addition to 23.95 GHz,

at room temperature. These measurements were made only on sample 2 because sample 1 was damaged slightly after the measurement of the resistivity ratio. The measurements at 73 GHz were difficult because the signal was very small. As a result we were able to measure only the resonance for the (100) direction at this frequency. The resonance fields and linewidths obtained from experiment and those calculated using program I are listed in Table 4-3, and the frequency dependence of the linewidth is shown in Figure 4.1. The agreement between the experimental and calculated values of H_{fmr} is generally good. The experimental linewidths are larger than the calculated linewidths at 9.115 and 23.95 GHz. It is somewhat disturbing that the (110) linewidth is consistently larger than the (100) and (111) linewidths. The differences are roughly equal to the experimental uncertainty at each frequency. It was demonstrated by Anderson, Bhagat and Cheng[30] that the in-plane linewidth in Nickel at 22 GHz at room temperature was isotropic, within their experimental uncertainty of ±10 Oe.

From calculations carried out with program I the frequency dependence of the linewidth at room temperature and in the frequency range of interest, ≥ 9 GHz,is:

$$\Delta H(f) = 25\ \text{Oe} + 5\times10^{-8}G(\text{sec}^{-1})f(\text{GHz}) \qquad (4.2)$$

where f is the frequency and G is the Gilbert damping parameter. This expression has been verified for values of G between 1 and

TABLE 4-3

Frequency dependence of H_{fmr} and ΔH at room temperature, Sample 2.

F(GHz)	H_{fmr} (kOe)			ΔH(Oe)		
	[100]	[110]	[111]	[100]	[110]	[111]
9.115						
Expt.	1.48±.02	1.28	1.07	160±20	190	160
Calc.	1.46	1.31	1.03	140	140	140
23.95						
Expt.	5.58±.02	5.34	5.14	340±30	380	360
Calc.	5.58	5.37	5.16	320	320	320
34.7						
Expt.	8.92±.03	8.69	8.57	420±40	475	430
Calc.	8.92	8.69	8.50	450	450	450
73.0						
Expt.	21.1±.1	–	–	900±100	–	–
Calc.	21.2	21.0	20.8	920	920	920

Calc: Program I, local conductivity, exchange, local damping, $G = 2.45 \times 10^8$ sec^{-1}, no surface anisotropy.

$4x10^8$ sec^{-1}. The zero frequency intercept is a result of the exchange conductivity broadening.

The frequency dependence of the (100) linewidth is shown in Figure 4.1. The (100) data is shown because we have values for the linewidth at four frequencies. The solid lines on the figure are a least squares fit of this data to a straight line (a), and the frequency dependence expected using program I with $G = 2.45x10^8$ sec^{-1}(b). The slopes and intercepts of these two lines are listed in the figure caption. Comparing the experimental slope with (4.2) we see that our data are consistent with a Gilbert damping parameter $G = 2.3\pm0.3x10^8$ sec^{-1}. The uncertainty in this value is large but it agrees well with the values of other authors[38,24,27,17] (see the numbers quoted in Section 1.2). The zero frequency intercept is 50 Oe which is some 25 Oe larger than the 25 Oe expected from the calculations made with program I from which equation (4.2) was obtained. A possible explanation for this difference would be the presence of some surface spin-pinning. If a surface anisotropy $K_s = -0.1$ erg/cm^2 with the anisotropy axis parallel to the static magnetization was assumed, the frequency dependence of the linewidth would be linear with the same slope as (4.2) but having a zero frequency intercept of 50 Oe. This surface anisotropy would neatly explain our (100) linewidth data.

In addition to broadening the FMR line spin pinning produces a shift in the position of the resonance. A surface

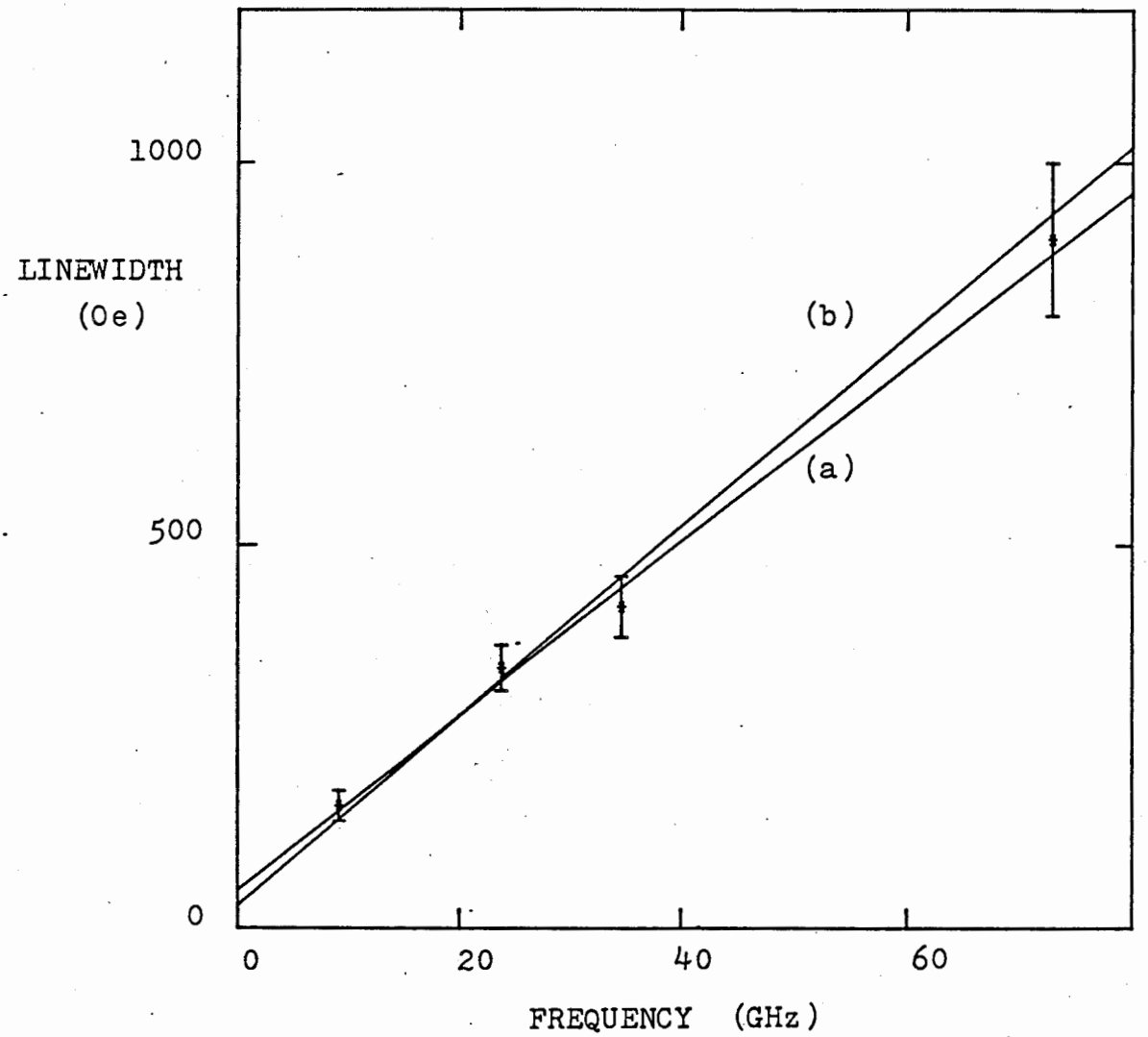

Figure 4.1 Frequency dependence of the FMR linewidth at room temperature, sample 2. The applied field was parallel to the [001] axis. (a) Linear fit to the data, slope = 11.6 Oe/GHz, intercept = 50 Oe. (b) Calculated dependence using program I, with the parameters of Table 4-1 and no spin-pinning, slope = 12.3 Oe/GHz, intercept = 25 Oe.

anisotropy of this magnitude would shift FMR to lower fields by approximately 25 Oe at 9 GHz, approximately 30 Oe at 23.95 GHz, and by approximately 35 Oe at 34.7 GHz. These shifts are roughly equal to the uncertainty in the experimental values of H_{fmr}. We note that Bhagat and Lubitz[13] used a surface anisotropy of 0.1 erg/cm^2 in their analysis.

Comparison of Experimental and Calculated Lineshapes

A typical FMR derivative curve at 23.95 GHz is shown in Figure 4.2. This curve was measured on sample 2 with the applied field parallel to the (100) axis. The solid line on the figure is the absorption derivative calculated using program I, with a Gilbert damping of 2.6×10^8 sec^{-1} and no surface anisotropy. This value of the damping parameter was chosen to reproduce the linewidth of 340 Oe. The other parameters used in the calculation are those listed in Table 4-1. If we assumed a Gilbert damping of $G = 2.45 \times 10^8$ sec^{-1} and a surface anisotropy $K_s = -0.1$ erg/cm^2 the calculated linewidth would equal the experimental linewidth and the match between the lineshapes would be comparable to that shown in the figure. The peaks in the experimental curve near zero field are associated with domain wall motion during saturation of the sample. The low field zero crossing of the derivative occurs at Ferromagnetic Antiresonance (FMAR). The asymmetry of the experimental derivative, the ratio of the low field derivative peak amplitude

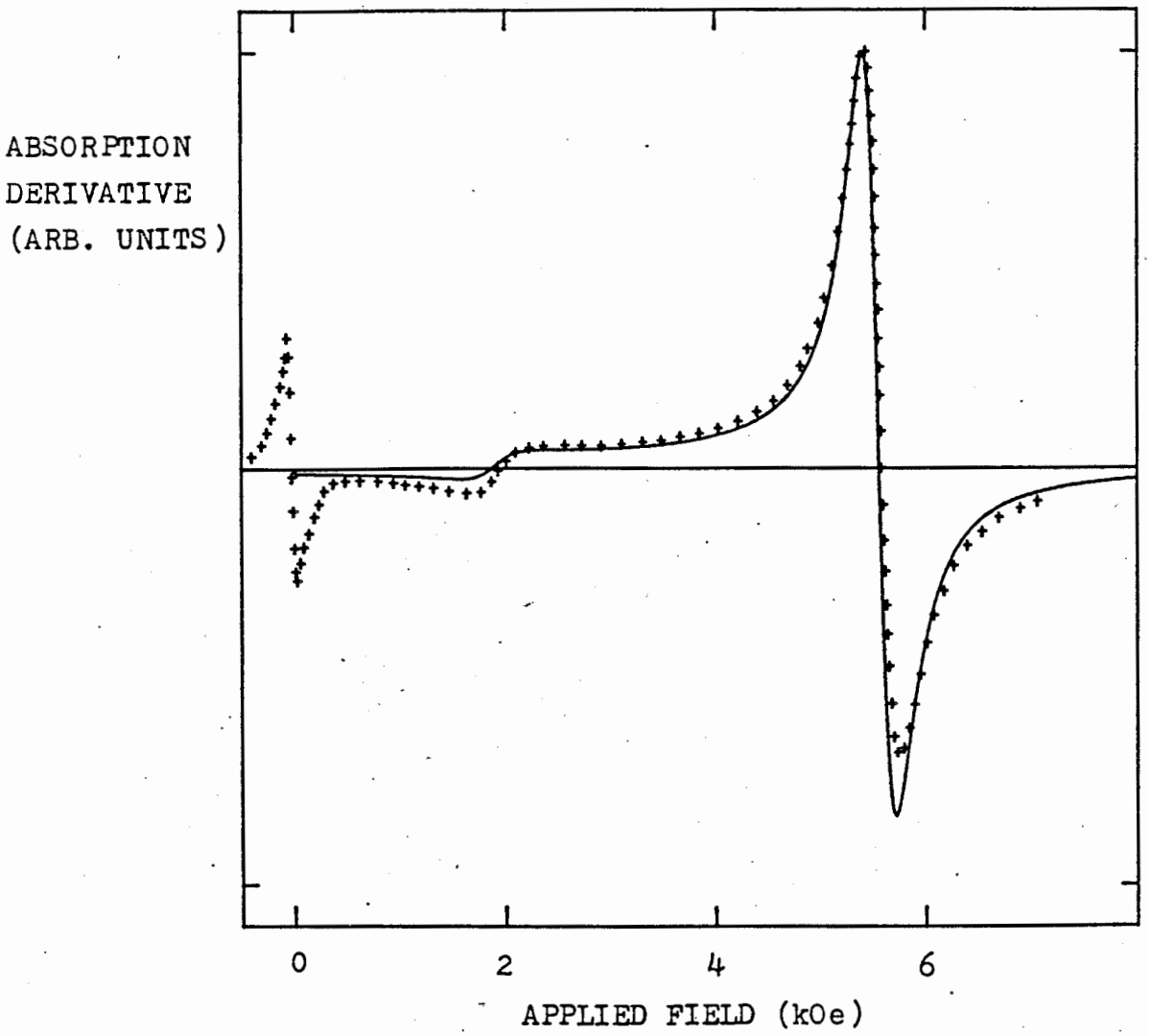

Figure 4.2 Experimental FMR absorption derivative at room temperature, 23.95 GHz, with the applied field parallel to [001]. The solid line is the absorption derivative calculated using program I, with a Gilbert damping parameter $G = 2.6 \times 10^8$ sec^{-1}. The other parameters used in the calculation are listed in Table 4-1.

to the high field derivative peak amplitude, does not agree with the calculated asymmetry. This is a common observation. For example Bhagat, Hirst and Anderson[27] quote experimental asymmetries in Nickel of 1.32 to 1.40 at 22 GHz which may be compared with their calculated asymmetry of 1.18. Our asymmetries are similar in magnitude to those of Bhagat, Hirst and Anderson.

The Angular Variation of H_{fmr}

The variation of the resonance field with the direction of the applied field in the sample plane is shown in Figure 4.3. The data was collected by measuring FMR with the magnet rotated from a position where the applied field was parallel to a principal axis and perpendicular to the microwave magnetic field. The signal becomes small, and the lineshape may be distorted, if the angle between the applied and microwave magnetic fields becomes small so data may be taken only in a limited range of angles about each principal axis. The solid line in the figure is the no-exchange no-damping value of the resonance field calculated using the MCA fields $a(\phi)$ and $\gamma(\phi)$, see equations (2.57). The agreement between the calculation and experiment is splendid. This plot is useful primarily because it indicates that the sample plane does indeed coincide closely with a (110) normal crystal plane.

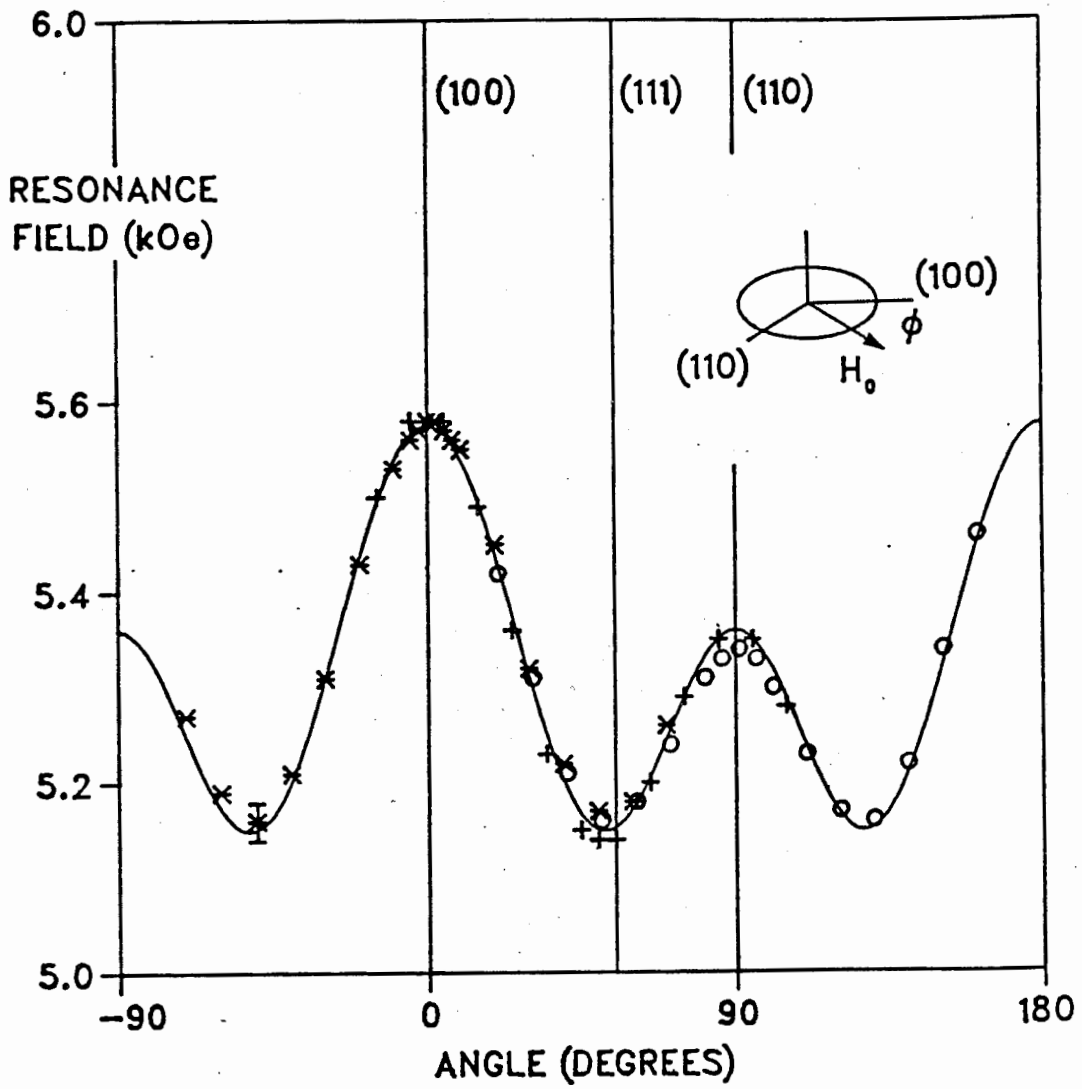

Figure 4.3 Variation of the resonance field, H_{fmr}, with the direction of the applied field in the sample plane, room temperature, 23.95 GHz. The data was taken by rotating the magnet about: (100) * ; (111) + ; (110) o . The experimental uncertainty is indicated by the single error bar at -50°. The solid line is the no-exchange no-damping value of H_{fmr}.

As was pointed out in Section 2.3 the angular variation of H_{fmr} should follow the no-exchange no-damping variation if $2|K1|/M_s << H_{fmr}$, that is, if the magnetization is parallel to the applied field at FMR. This is certainly true here where $2|K1|/M_s$ = 240 Oe. Of course the experimental values of H_{fmr} will not equal the calculated values because the damping and exchange shifts are not considered in the calculation. The angular variation of H_{fmr} obtained using equations (2.57) is the same as that which would be obtained from calculations using program II, the only program which could be used for calculating FMR when the applied field was not parallel to a principal axis. Program II did not include exchange so that the values of H_{fmr} calculated with that program would not equal the experimental values because of the neglect of the exchange shift.

The damping and exchange shift, the difference between the experimental and the no-exchange no-damping values of H_{fmr}, is approximately 30 Oe to lower fields in Nickel at room temperature at 23.95 GHz, from the calculations listed in Table 4-2. This is roughly the experimental uncertainty in H_{fmr}. It is not reasonable to compare the resonance field values on the scale of Oersteds as the parameters entering a calculation are not known with this precision. For example a change in K1 from $-.59 \times 10^5$ erg/cm^3 to $-.57 \times 10^5$ erg/cm^3, corresponding to a change in the temperature of the sample of approximately 2°[67], produces a shift in H_{fmr} of approximately 10 Oe.

4.3 Results at 77 K

The experimental values of the resonance field and the linewidth for the two samples at 77 K at 23.95 GHz are listed in Table 4-4. The results for the two samples were in good agreement with each other. We found that the linewidth at 77 K was anisotropic. The linewidths measured with the applied field parallel to the (100) and (111) axes were identical within experimental uncertainty. The (110) linewidth was approximately 160 Oe, or 16% larger, for both samples.

Also listed in Table 4-4 are the no-exchange, no-damping values of H_{fmr}, and the values of H_{fmr} calculated using a local conductivity and wavenumber independent Gilbert damping with and without exchange (programs I and II) and the damping parameter required to reproduce the experimental linewidth using program I, assuming no pinning of the spins. If we assume a surface anisotropy of $K_s = -0.1$ erg/cm^2 the calculated linewidths are approximately 50 Oe larger and the resonance fields are approximately 50 Oe lower than if $K_s = 0$. The value of the Gilbert damping parameter required to reproduce the (100) linewidth with $K_s = -0.1$ erg/cm^2 was $G = 6.6 \times 10^8$ sec^{-1} as opposed to $G = 7.0 \times 10^8$ sec^{-1} for $K_s = 0$. The calculated resonance fields are discussed in Section 4.6.

Experimental absorption derivative curves are shown in Figure 4.4 for the three principal axes. These curves have been

TABLE 4-4

Results for 77 K, 23.95 GHz.

		[100]	[110]	[111]
H_{fmr}(kOe)	Sample 1	8.39±0.04	5.51	2.81
	Sample 2	8.45	5.47	2.80
	Calc. A	8.44	5.59	2.91
	Calc. B	8.49	5.64	2.96
	Calc. C	8.42	5.58	2.91
ΔH(Oe)	Sample 1	880±50	1020	860
	Sample 2	860	1020	840
G(sec^{-1})		$7.0x10^8$	$8.2x10^8$	$7.0x10^8$

Calc. A: No-exchange, no-damping value of H_{fmr}.

Calc. B: Local conductivity, no exchange, local damping with the value of G listed in the Table, program II.

Calc. C: Local conductivity, exchange, no surface anisotropy, local damping with the value of G listed in the Table, program I.

---

normalized to the same low field derivative peak amplitude. The large shifts in the resonance due to MCA are evident by comparing the field at which resonance occurs for the three axes. The sharp spikes near zero field are due to domain wall motion as at room temperature. The field values, $2|K1|/M_s$ and $|K1|/M_s$, at which the magnetization becomes parallel to the applied field if the applied field is parallel to the (100) or (110) axes respectively have been indicated on the figures.

Recall the calculated variation of the angle between the magnetization and the applied field shown in Figure 2.7. The irregular absorption below these field values is due to absorption during rotation of the magnetization, see below.

Comparison of Experimental and Calculated Lineshapes

In Figure 4.5 we show a comparison of the experimental (100) absorption derivative with calculated curves. The curve in (a) was calculated with program I, using a value of $G = 7.0 \times 10^8$ sec^{-1}, and no spin-pinning. The curve in (b) was calculated using program II and the same value of G as was used for the calculation shown in (a). The experimental asymmetry differs from the calculated asymmetry, curve (a): however the difference between calculation and experiment is smaller than at room temperature. If we assumed a Gilbert damping of $G = 6.6 \times 10^8$ sec^{-1} and a surface anisotropy $K_s = -0.1$ erg/cm^2 instead of $G = 7.0 \times 10^8$ sec^{-1}, the calculated lineshape was the same as that shown in (a). Absorption derivatives were also calculated using program III, with a non-local conductivity and a wavenumber independent damping. The lineshape obtained using a non-local conductivity was almost indistinguishable from that obtained using a local conductivity so the non-local line is not reproduced here. Based on this comparison it appears that the local conductivity theory may be used to describe the absorption in Nickel at 77 K. From a comparison of the calculated

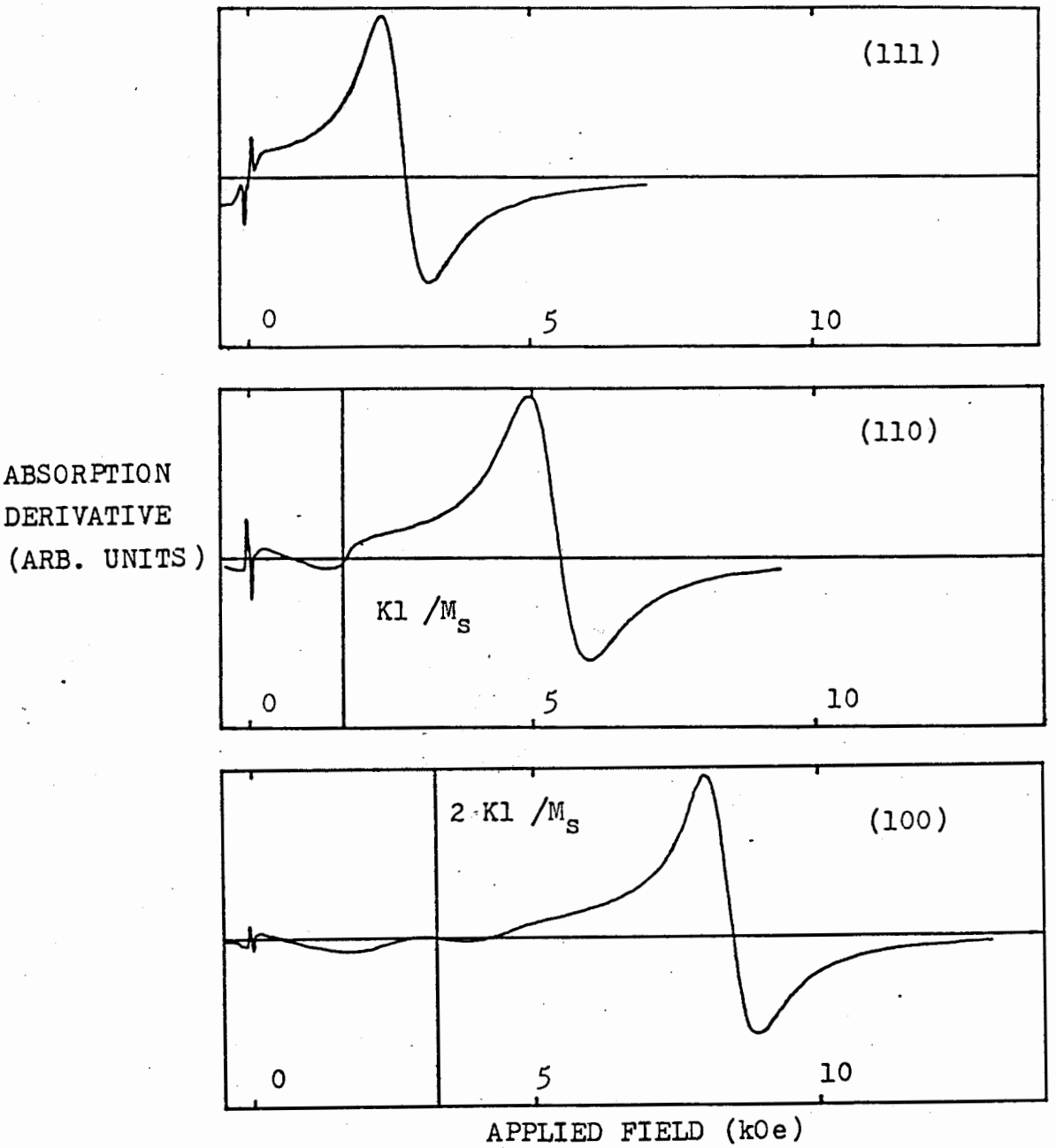

Figure 4.4 Absorption derivatives vs applied field at 77 K, 23.95 GHz, Sample 2 for the three principal axes. The fields $|K1|/M_s$ and $2|K1|/M_s$ at which the magnetization becomes parallel to the applied field if the applied field were parallel to the (110) or (100) axes respectively are indicated on the appropriate figure. $2|K1|/M_s$=3.22 kOe at 77 K.

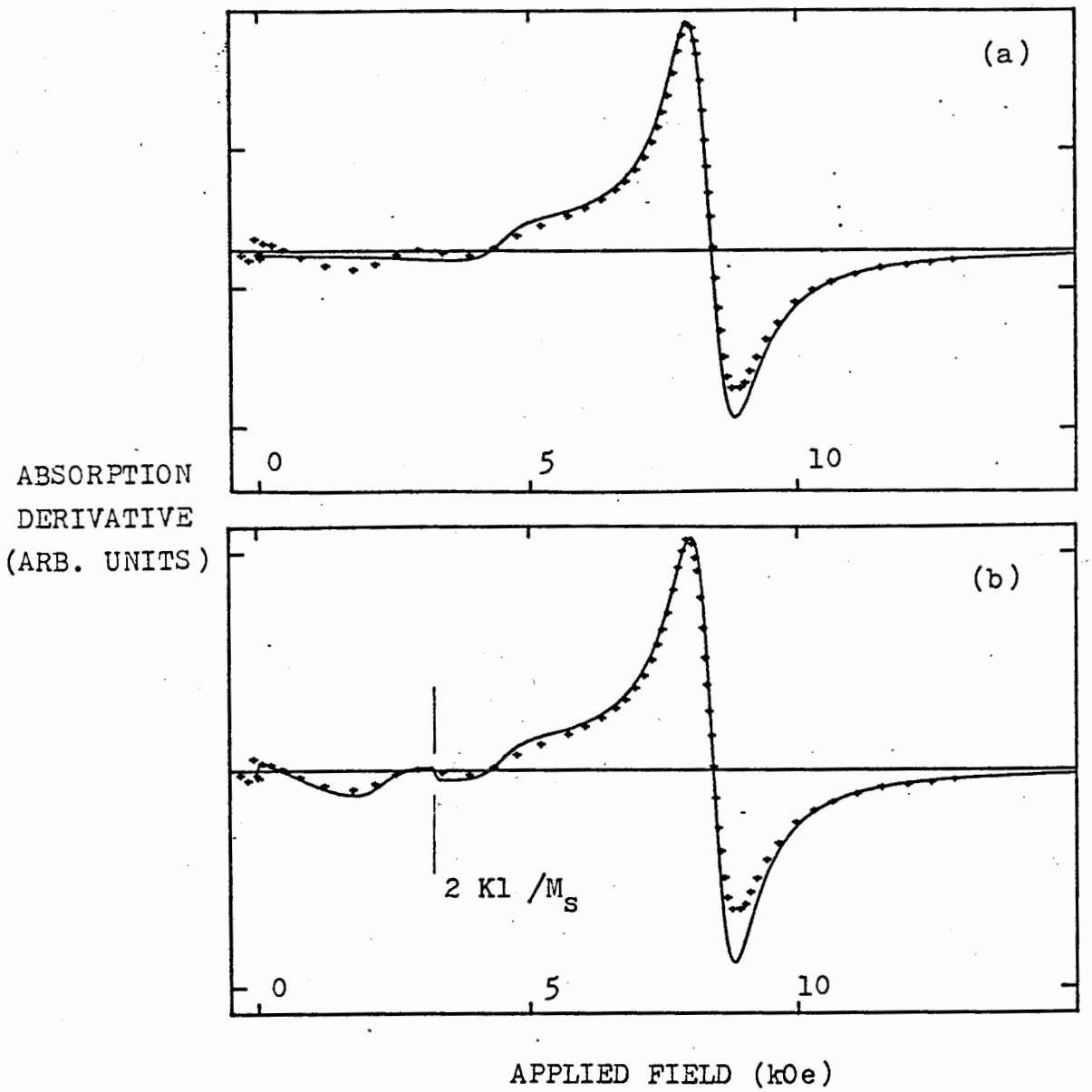

Figure 4.5 Comparison of calculated absorption derivatives with experiment, 77 K, 23.95 GHz, Sample 2. The applied field was parallel to a (100) axis. (a) Calculation using program I, local conductivity, exchange, no surface anisotropy. A damping parameter G = $7.0 \times 10^8 sec^{-1}$ was used. Other parameters are listed in Table 4-1. (b) Calculation using program II, local conductivity, no exchange, dragging. The parameters used in (a) were used for this calculation.

linewidths for (a) and (b) it appears that exchange, with no spin pinning, contributes approximately 80 Oe to the linewidth at 77 K. Curve (b) demonstrates that the absorption at low fields, ($H_o<2|K1|/M_s$), is due to dragging of the magnetization. It is remarkable how well the simple model used for the dragging processes describes the data. It is interesting to note the discontinuity in the calculated derivative at 3.22 kOe where the external field equals $2|K1|/M_s$.

The Angular Variation of H_{fmr}

The variation of the resonance field with the orientation of the applied field in the sample plane is shown in Figure 4.6. for sample 2. As was pointed out in Section 4.2 data can be taken by rotating the magnet through only a limited range of angles about the position where the applied field is parallel to a principal axis and perpendicular to the microwave magnetic field. As a result collecting the data shown in Figure 4.6 required cooling to 77 K three times, once for each axis, with a return to room temperature to rotate the endwall assembly holding the sample between each cooling. The solid line on the figure represents the variation with angle expected on the basis of program II, which allows for arbitrary orientation of the applied field with respect to the crystal axes. Dragging of the magnetization must be taken into account when considering the

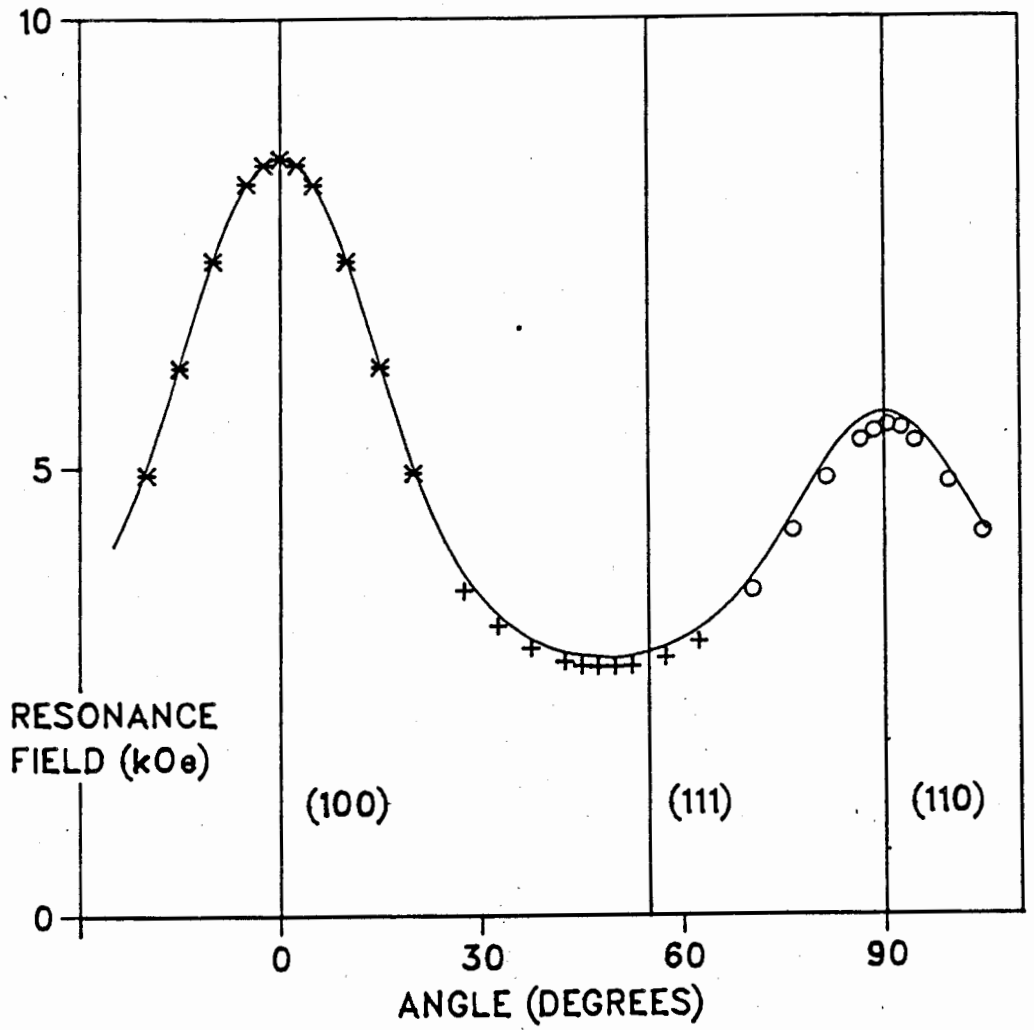

Figure 4.6 Variation of the resonance field, H_{fmr}, with the angle of the applied field in the sample plane, 77 K, 23.95 GHz. Data taken by rotating about (100): * ; (111): + ; (110): o . Experimental uncertainty (≃±40 Oe) is approximately the symbol size. The solid line is the result of calculations made with program II, which allows for the lack of alignment between the magnetization and the applied field.

angular variation of H_{fmr} and the linewidth since $2|K1|/M_s$ is of the order of H_{fmr}. To obtain these curves the absorption derivative was calculated for each angle of the applied field and the resonance field determined from the calculated curves. Since this calculation did not include exchange we used a value of $G = 7.7 \times 10^8$ sec^{-1} in order to reproduce the experimental linewidth for the (100) direction. The experimental and calculated variations of H_{fmr} agree well.

Since the calculations were made using a value of G larger than required by experiment, and neglecting exchange, the calculated values of H_{fmr} will be larger than if the correct value of G was used and exchange included, compare calculations B and C in Table 4-4 for example. Because of the neglect of exchange we would not expect the numerical values of the calculated resonance fields to equal the experimental values, however we would expect an approximately constant offset between the experimental and the calculated values. The damping is anisotropic so that the damping shift in H_{fmr} will be anisotropic, but, as can be seen from Table 4-4, the anisotropy in the shift is no greater than 10 Oe. Although the experimental and calculated angular variations agree well there is a systematic difference between the offset for data taken by rotating the magnet about the (100) axis and the data taken by rotating about the (111) and (110) axes. I have no explanation for this difference. It is clearly an experimental problem because it does not show up in the room temperature (Figure 4.3)

or the 4.2 K (Figure 4.13) angular variations. The difference is too large to be explained by a difference in the microwave frequency used for the different sets of measurements. A difference in the microwave frequency of 0.1 GHz (half of the tuning range of the klystron) would shift the resonance field by only 30 Oe.

The Angular Variation of ΔH

The variation of the linewidth with the direction of the applied field in the sample plane is shown in Figure 4.7. The linewidths plotted here were measured at the same time as the resonance fields shown in Figure 4.6. The solid line in the figure was calculated using the procedure outlined above for the calculation of the angular variation of the resonance field. This calculated angular variation of the linewidth demonstrates clearly the effects of dragging on the FMR linewidth. Note especially the large increase in the linewidth at angles near the (100) and (111) directions. We do not expect the calculated variation of the linewidth to reproduce the experimental variation since an isotropic damping parameter was assumed for the calculation with the result that the calculated linewidths for the (100), (111) and (110) directions were the same. The discrepancy between experiment and calculation near the (110) direction is certainly because the damping is not isotropic. The discrepancy at angles between the (100) and (111) directions

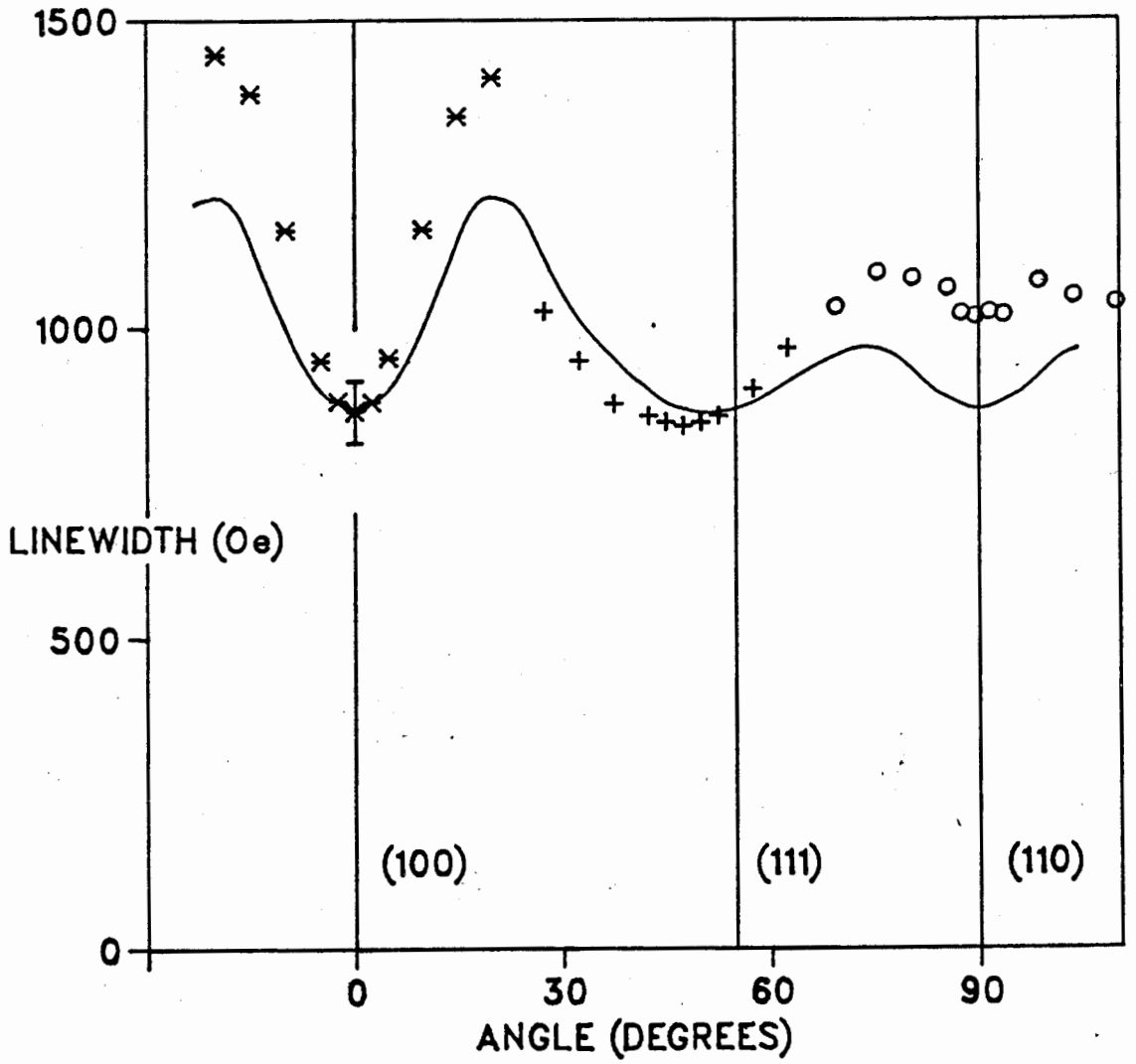

Figure 4.7 Variation of the FMR linewidth, ΔH, with the angle of the applied field in the sample plane, 77 K, 23.95 GHz. Data taken by rotating about (100): * ; (111): + ; (110): o . The solid line is the result of calculations made with program II, which allows for the lack of alignment between the magnetization and the applied field. An isotropic damping parameter $G = 7.7 \times 10^{8} sec^{-1}$ was assumed for the calculation.

is possibly due to an anisotropy of the damping parameter.

4.4 Results at 4.2 K

Data at 4.2 K were collected using a bolometer to measure the absorption rather than the absorption derivative as was measured with the field modulation technique used at higher temperatures. It was necessary to use the bolometer because the FMR line becomes very broad and the field modulation system lacked the sensitivity required to detect the FMR signal. The result of an experiment was a signal proportional to the power absorbed by the sample as a function of the applied field. This data was stored on a computer and could be handled numerically. For analysis the data was differentiated numerically and the linewidth and resonance field obtained from the derivative.

The experimental values of the resonance field and the linewidth for the two samples at 4.2 K, at 23.95 GHz are listed in Table 4-5. The results for the two samples agree within the experimental uncertainty. Our results indicate that the linewidth is anisotropic at 4.2 K. As at 77 K the (110) linewidth was greater than the (111) and (100) linewidths. The difference between the (110) and the (111) linewidths was approximately 200 Oe or 10%. At 77 K we found that the (100) and (111) linewidths were the same, however at 4.2 K the (111) linewidth was greater than the (100) linewidth, by approximately 200 Oe. The differences between the linewidths

TABLE 4-5

Results for 4.2 K, 23.95 GHz.

		[100]	[110]	[111]
H_{fmr}(kOe)	Sample 1	9.56±0.05	5.17	2.15
	Sample 2	9.65	5.23	2.22
	Calc. A	9.96	5.58	2.48
	Calc. B	10.09	5.78	2.53
	Calc. C	9.99	5.63	2.56
	Calc. D	9.97	5.61	2.53
	Calc. E	9.62	5.22	2.15
ΔH(Oe)	Sample 1	1600±50	2000	1800
	Sample 2	1640	2100	1830
G(sec^{-1})		$14x10^8$	$18x10^8$	$16x10^8$

Calc. A: No-exchange, no-damping values of H_{fmr}.

Calc. B: Local conductivity, no exchange, local damping, values of G as listed above, program II.

Calc. C: Local conductivity, exchange, local damping, values of G as listed above, program III.

Calc. D: Non-local conductivity, exchange, local damping, values of G as listed above, program III.

Calc. E: Non-local conductivity, exchange, isotropic non-local damping, values of $a=1.19x10^8 sec^{-1}$, $b=1.07x10^8 sec^{-1}$, l_D=620 A at 4.2 K (calculated linewidth at 4.2 K=1610 Oe), program III.

for the three axes are four times the experimental uncertainty in the linewidth, ±50 Oe.

Also listed in Table 4-5 are values of H_{fmr} calculated with a number of combinations of damping, exchange and conductivity: the resonance fields for the (100) direction were calculated using the value of K1′ which includes the MCA torque ascribed to the X_2 pocket[44]. If this contribution were neglected the calculated resonance fields for the (100) direction would be shifted 180 Oe to higher fields. The calculated values listed in Table 4-5 will be discussed in Section 4.6, but it is worth noting here the wide variations between them. In particular the difference between the calculated resonance fields for the wavenumber dependent and the wavenumber independent damping, E and D respectively in the Table, is approximately 400 Oe. The values of the damping parameter, G, listed in the Table are those required to reproduce the experimental linewidths using program III with a non-local conductivity and a wavenumber independent damping. The surface anisotropy was assumed to be zero in all of these calculations. The difference between the linewidth calculated using program II with $G = 14 \times 10^8$ sec^{-1} and that calculated using program III with a non-local conductivity and $G = 14 \times 10^8$ sec^{-1} was 30 Oe, so that exchange, with no spin pinning, contributes approximately 30 Oe to the linewidth at 4.2 K. A surface anisotropy $K_s = -0.1$ erg/cm^2 changes the calculated linewidth by less than 10 Oe and shifts the resonance by approximately 25 Oe to lower fields. We may safely neglect

spin pinning in the discussion of our 4.2 K results which follows.

The experimental absorption curves for the two samples at 23.95 GHz are shown in Figure 4.8. As at 77 K the irregular absorption at fields below $2|K1|/M_s$ or $|K1|/M_s$ for the (100) and (110) axes respectively occurs during rotation of the magnetization. These field values have been indicated on the figures. The experimental zero has been suppressed on these figures, but except for the (100) trace of sample 2, the curves have not been scaled relative to each other. The zero for the (100) trace of sample 2 was mistakenly taken without shorting the input to the lock-in amplifier, see Chapter 3, and so the scaling of the data by the data acquisition program was different to that of the other curves shown. By analogy with Figure 4.8(a) this curve has been scaled to give the same absorption at the peak and at the saturation field $2|K1|/M_s$ as the (110) absorption curve for this sample.

In Figure 4.9(a) we show a comparison of the absorption curves for the two samples. Since the experimental zero is not meaningful the curves have been scaled vertically to the same absorption at 200 Oe and at the peak for this comparison. The agreement between the absorption lineshapes for the two samples for the two other crystal axes was of similar quality. In Figure 4.9(b) is a comparison of the absorption measured with the bolometer and the absorption measured by monitoring the microwave power reflected from the cavity with the microwave

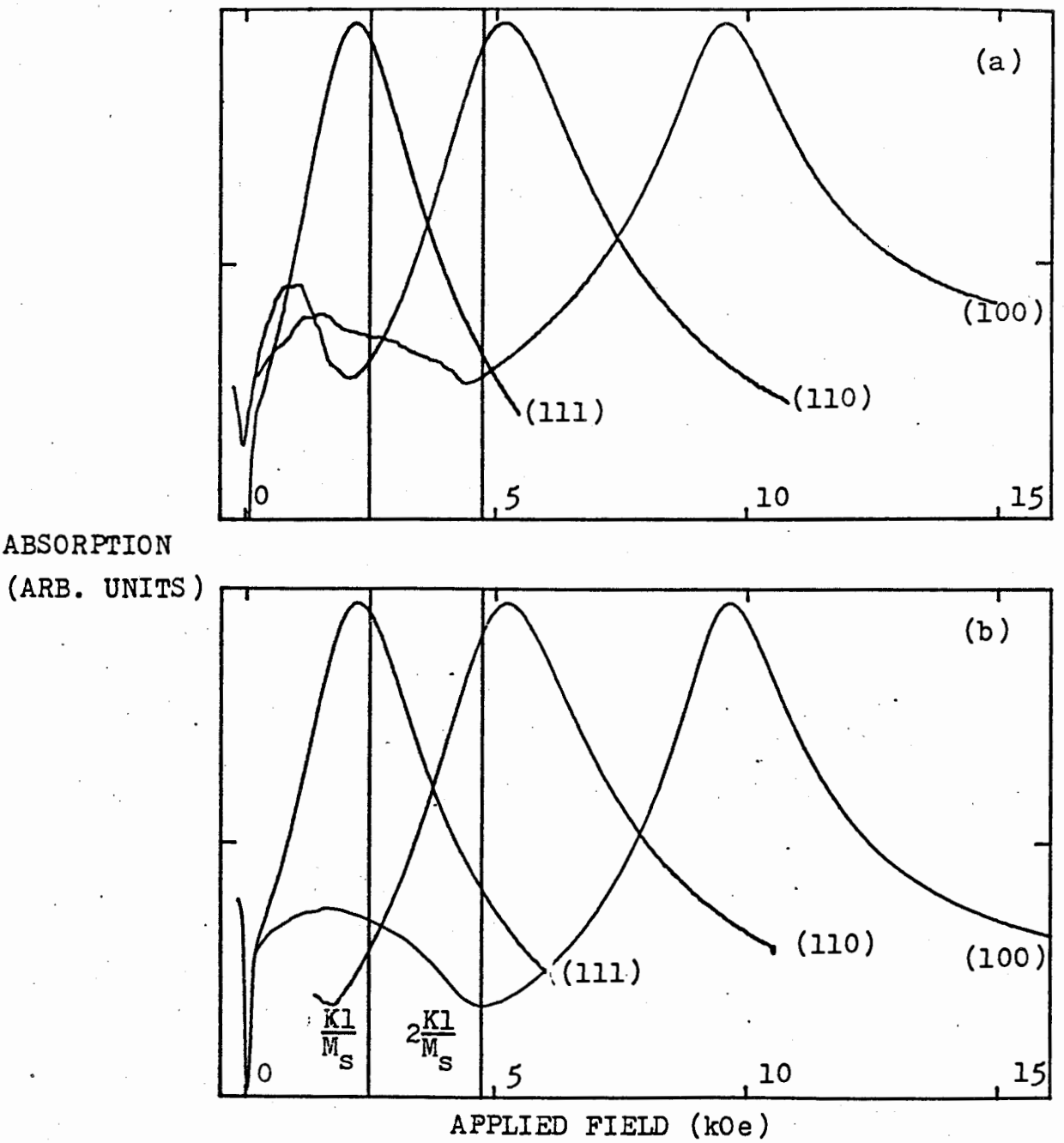

Figure 4.8 Absorption curves at 4.2 K, 23.95 GHz for the three crystal axes, (a) Sample 1; (b) Sample 2; The fields $|K1|/M_s$ and $2|K1|/M_s$ at which the magnetization becomes parallel to the applied field if the applied field is parallel to the (110) or (100) axes respectively are indicated on the appropriate figure. $2|K1|/M_s$=4.92 kOe at 4.2 K.

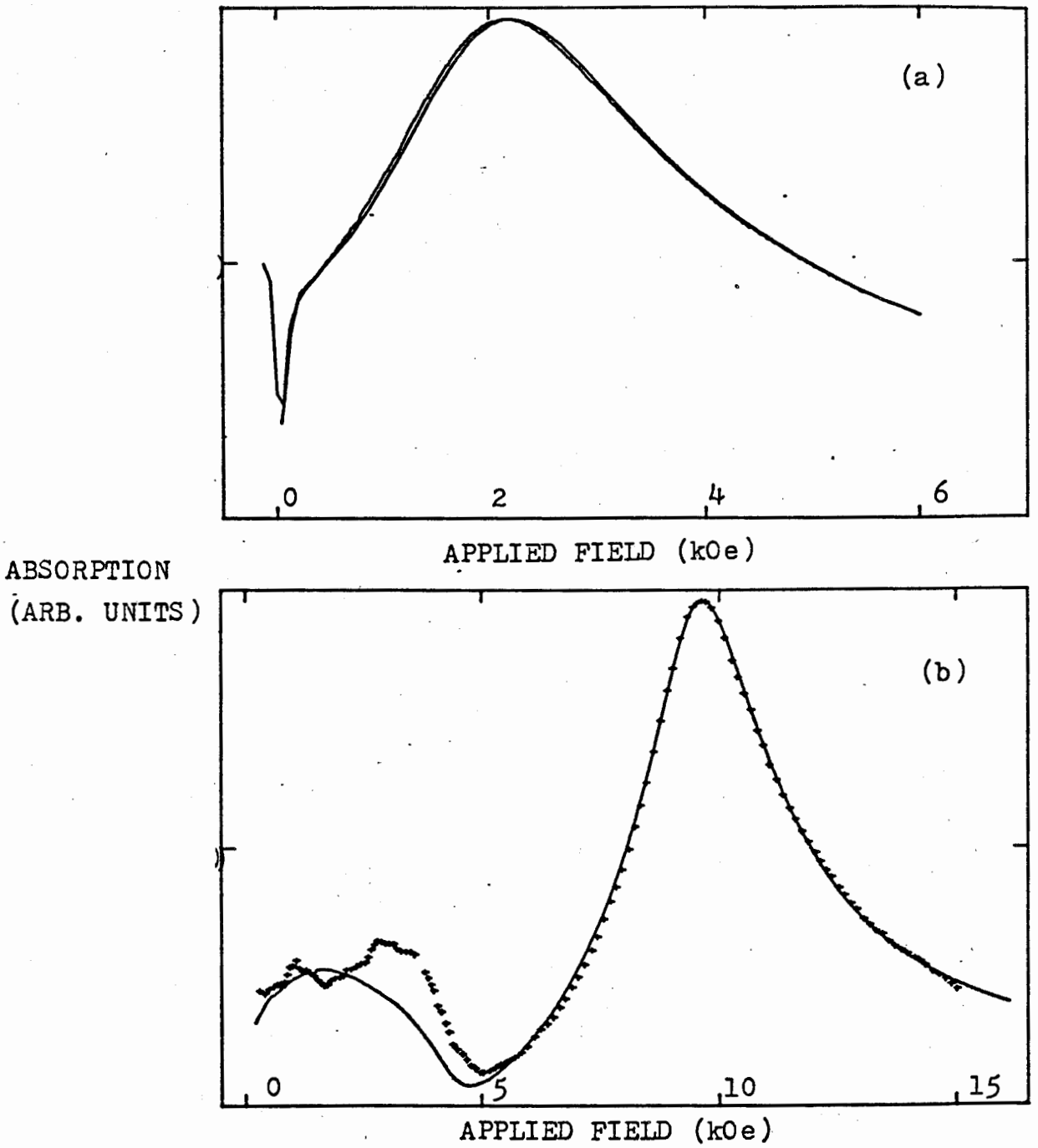

Figure 4.9 (a) Comparison of the absorption for sample 1 and sample 2. The applied field was parallel to (111). The curves have been scaled vertically to match at 200 Oe and at the peak. (b) Comparison of the absorption measured using the bolometer (solid line), and the microwave diode (+), sample 2. The applied field was parallel to (100).

diode. The diode data was taken by sweeping the applied field in the direction of increasing and decreasing field and averaging the two curves to compensate for an approximately linear drift with time in the diode voltage. The lineshapes measured with the two techniques agree well which gives some confidence in the data obtained with the bolometer. Although the diode data appears smooth in the figure we were unable to obtain a reliable value of the linewidth by differentiating the data numerically, even with considerable massaging before differentiation.

In Figure 4.10 we show an absorption curve measured using the bolometer, with the numerically calculated derivative superimposed. The linewidth has been indicated on the figure to indicate the position of the inflection points relative to the absorption peak.

Comparison of Experimental and Calculated Lineshapes

In Figures 4.11 and 4.12 we show comparisons of calculated curves with the experimental curves. The calculations shown were made using program III with a non-local conductivity. Since $q\ell > 1$ at FMR at 4.2 K, see Table 2-3, the wavenumber dependence of the conductivity is important and must be considered when calculating the absorption for comparison with experiment. A wavenumber dependent (non-local) damping was assumed for the calculation shown in Figure 4.11, and a

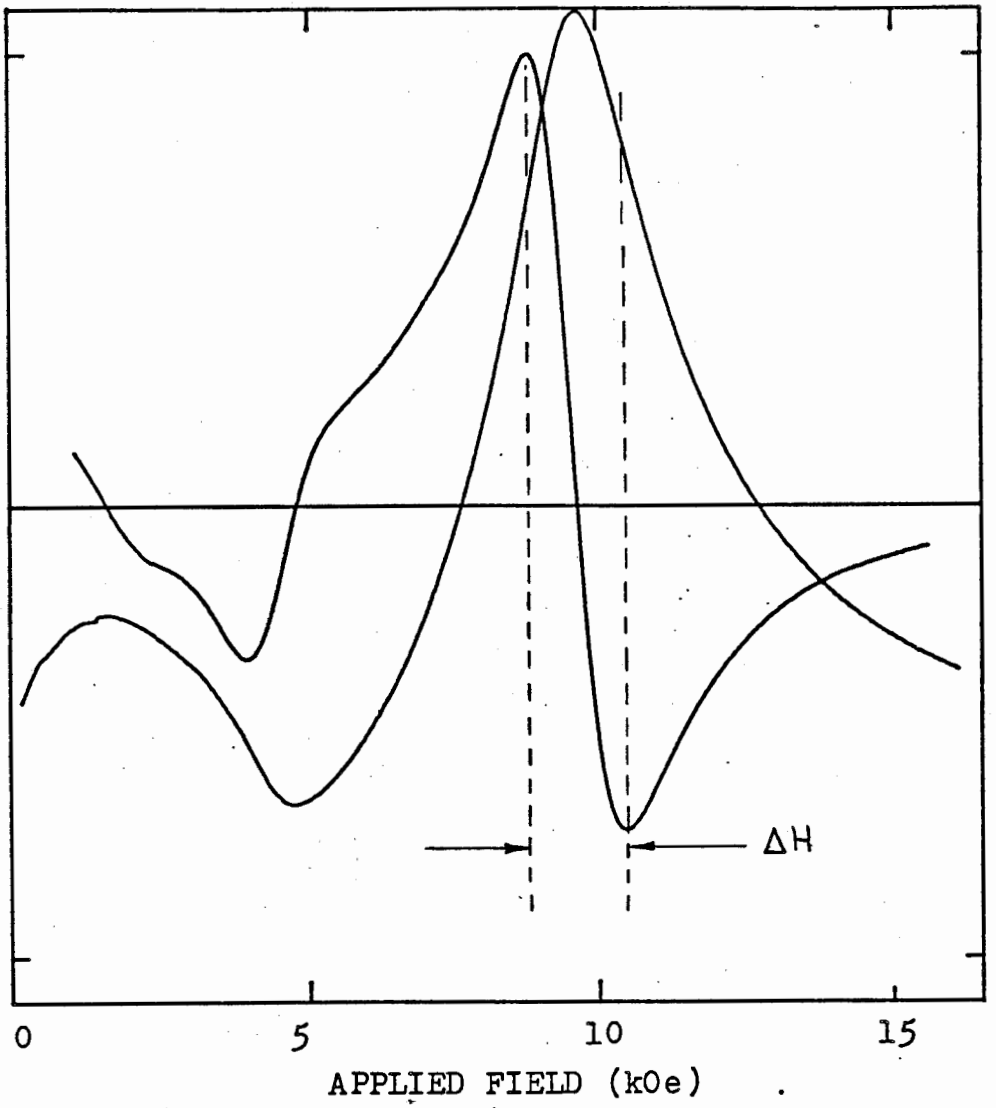

Figure 4.10 The absorption and the absorption derivative at 4.2 K, 23.95 GHz for sample 2. The applied field was parallel to (100). The FMR linewidth is indicated on the figure.

wavenumber independent damping for the calculation shown in Figure 4.12. The experimental data is the resonance for the (100) direction of sample 2. The absorption was calculated ignoring MCA and the resulting curves were shifted along the field axis until the peak position matched that of experiment. This is valid since MCA shifts the position of the resonance but has no effect on the lineshape, at least for the (100) and (111) directions where the effective MCA fields, a and γ, are equal. We consider in Section 4.6 the effect of the form of the damping on the resonance field, but for the moment we consider only the lineshape. The comparison between calculation and experiment is shown for both the absorption and the absorption derivative. In a comparison between the calculated and experimental derivatives the attention is drawn to the field region around the FMR peak, while in a comparison of the absorption attention is focussed on the tails. It is worthwhile to examine both cases. The results of the calculations are shown only for fields greater than $2|K1|/M_s$ as the calculation is not valid if the magnetization is not parallel to the applied field.

The form of the wavenumber dependent damping assumed in the calculation was:

$$G(q,T) = a(\sigma_0(T)/\sigma_0(295))\arctan(ql_D)/ql_D + b\rho(T)/\rho(295) \qquad (4.3)$$

The curve shown in Figure 4.11 was calculated using the values

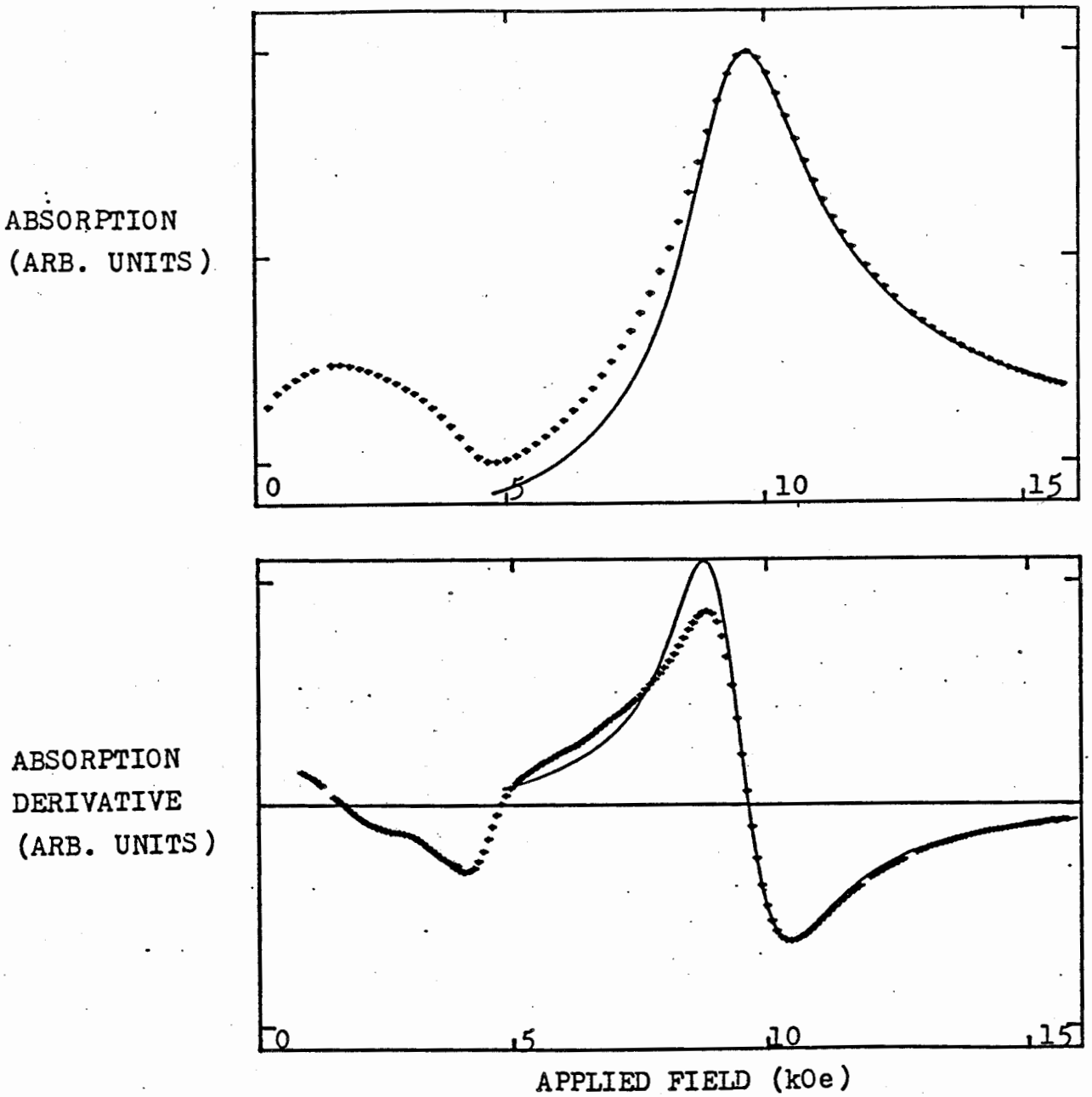

Figure 4.11 Comparison of calculated absorption and absorption derivative with experiment, 4.2 K, 23.95 GHz, sample 2. The applied field was parallel to (100). The calculation assumed a non-local conductivity and a wavenumber dependent damping with $a = 1.07 \times 10^8$ sec^{-1} $b = 1.19 \times 10^8$ sec^{-1} and $l_D = 620$ A. The calculated curves have been shifted along the field axis so that the FMR peak positions coincide.

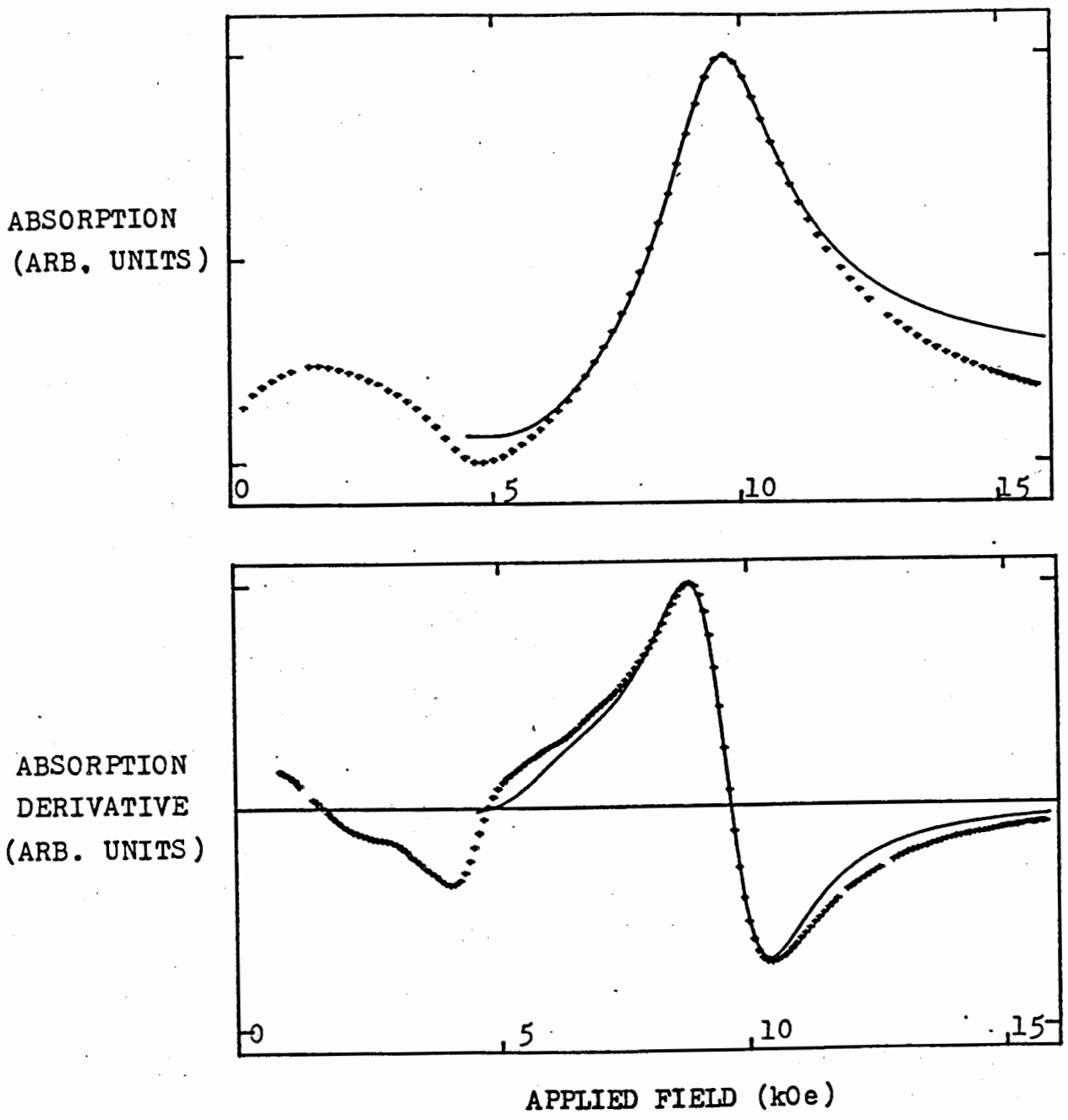

Figure 4.12 Comparison of calculated absorption and absorption derivative with experiment, 4.2 K, 23.95 GHz, sample 2. The applied field was parallel to (100). The calculation assumed a non-local conductivity and a wavenumber independent damping $G = 14 \times 10^8$ sec^{-1}. The calculated curves have been shifted along the field axis so that the FMR peak positions coincide.

$a = 1.07 \times 10^8$ sec^{-1} and $b = 1.19 \times 10^8$ sec^{-1} suggested by Cochran and Heinrich[37], using the experimental resistivity ratio of 38, and the value of the d-electron mean free path, $l_D = 620$ A at 4.2 K, adjusted to reproduce the experimental linewidth of 1640 Oe. This 4.2 K mean free path corresponds to a room temperature mean free path $l_D \simeq 16$ A. Calculations were made with a variety of values of a, b and l_D, subject to the constraints that the room temperature damping parameter, essentially (a + b), be 2.45×10^8 sec^{-1}, and that the 4.2 K linewidth be 1640 Oe. The lineshapes calculated using a = 0.8, 1.2 and 2.0×10^8 sec^{-1} with corresponding values of b and l_D, were virtually identical. The positions however were different, see Section 4.6. The agreement between the calculated and experimental lineshapes is superb if one looks only at the high field side of the resonance, $H_o > H_{fmr}$. The lineshapes on the low field side, $H_o < H_{fmr}$, do not agree at all.

In Figure 4.12 the comparison is made for a wavenumber independent damping $G = 14 \times 10^8$ sec^{-1}. Again the calculated curve has been shifted along the field axis to match the experimental peak position. The agreement between the calculated lineshape and the experimental lineshape is good in the peak region but not so good in the tails. The agreement between the experimental and calculated asymmetries is excellent. This match is equivalent to that shown by Bhagat and Hirst[1] in their Figure 3. If fits to the lineshape were the only consideration it would appear that the data was better

described by a wavenumber independent damping than by a wavenumber dependent damping.

The Angular Variation of H_{fmr}

In Figure 4.13 we show the angular variation of the resonance field. The solid line is the result of calculations made using program II, which neglects exchange, using an isotropic wavenumber independent damping parameter $G = 14 \times 10^8$ sec^{-1} to reproduce the (100) linewidth. The experimental and calculated angular variations agree well although there is an offset of approximately 400 Oe between them. This is simply because the damping and exchange shifts are not treated correctly in the theory.

FMR at 9.495 GHz at 4.2 K

Finally we present the results of measurements on sample 1 at 9.495 GHz at 4.2 K. The data is shown in Figure 4.14 for the applied field along (100). The field $2|K1|/M_s$ is indicated on the figure. The subsidiary peak is a result of dragging. As a result of MCA shifts and dragging FMR can be observed only when the applied field is within a small angle of a (100) direction. The signal amplitude decreased rapidly as the field was tilted away from the (100) direction and disappeared entirely at an

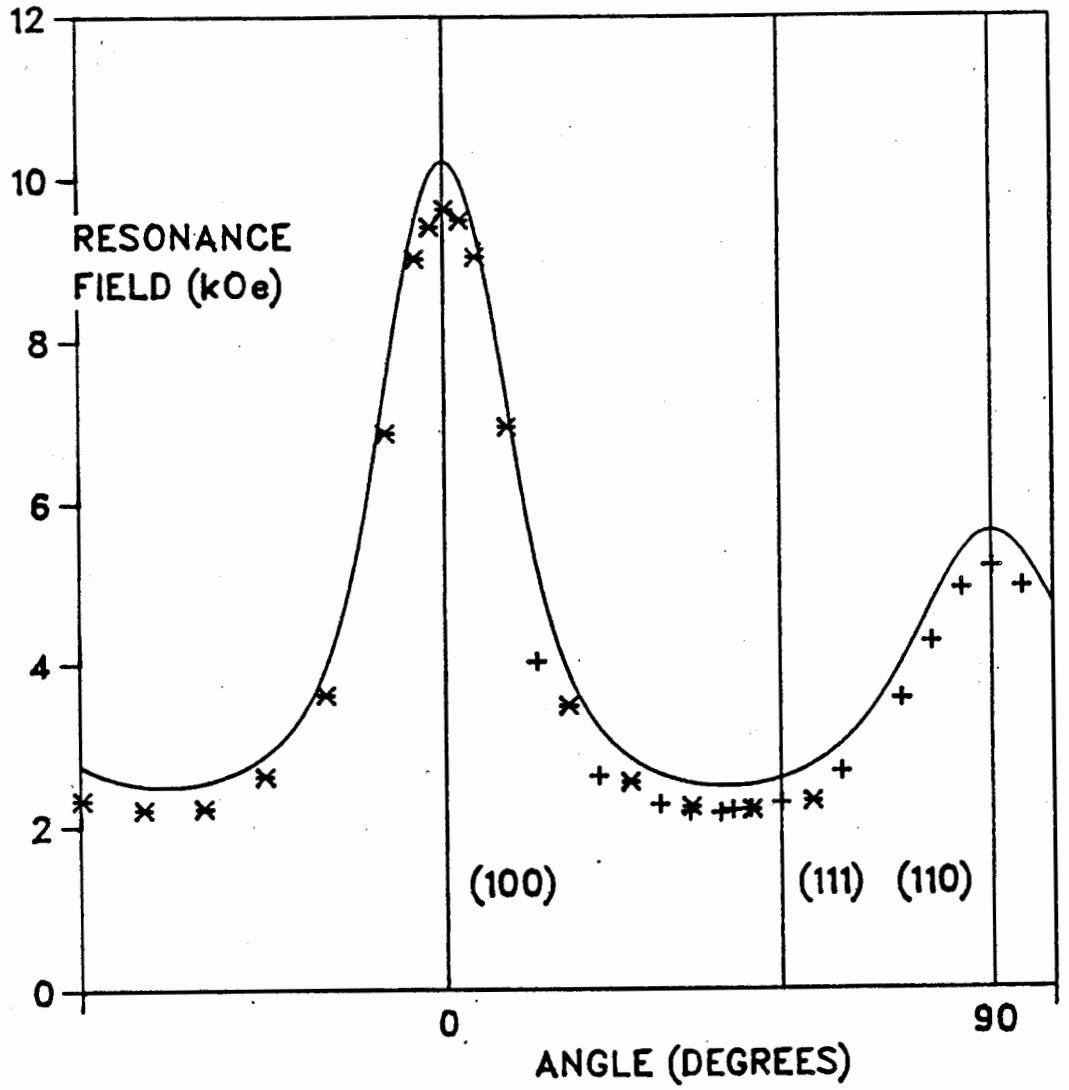

Figure 4.13 Variation of the resonance field, H_{fmr}, with the direction of the applied field in the sample plane, 4.2 K, 23.95 GHz. The data was taken by rotating the magnet about: (100) * ; (111) + . The experimental uncertainty is less than the symbol size. The solid line is calculated using program II with an isotropic damping parameter, $G = 14 \times 10^8$ sec^{-1}.

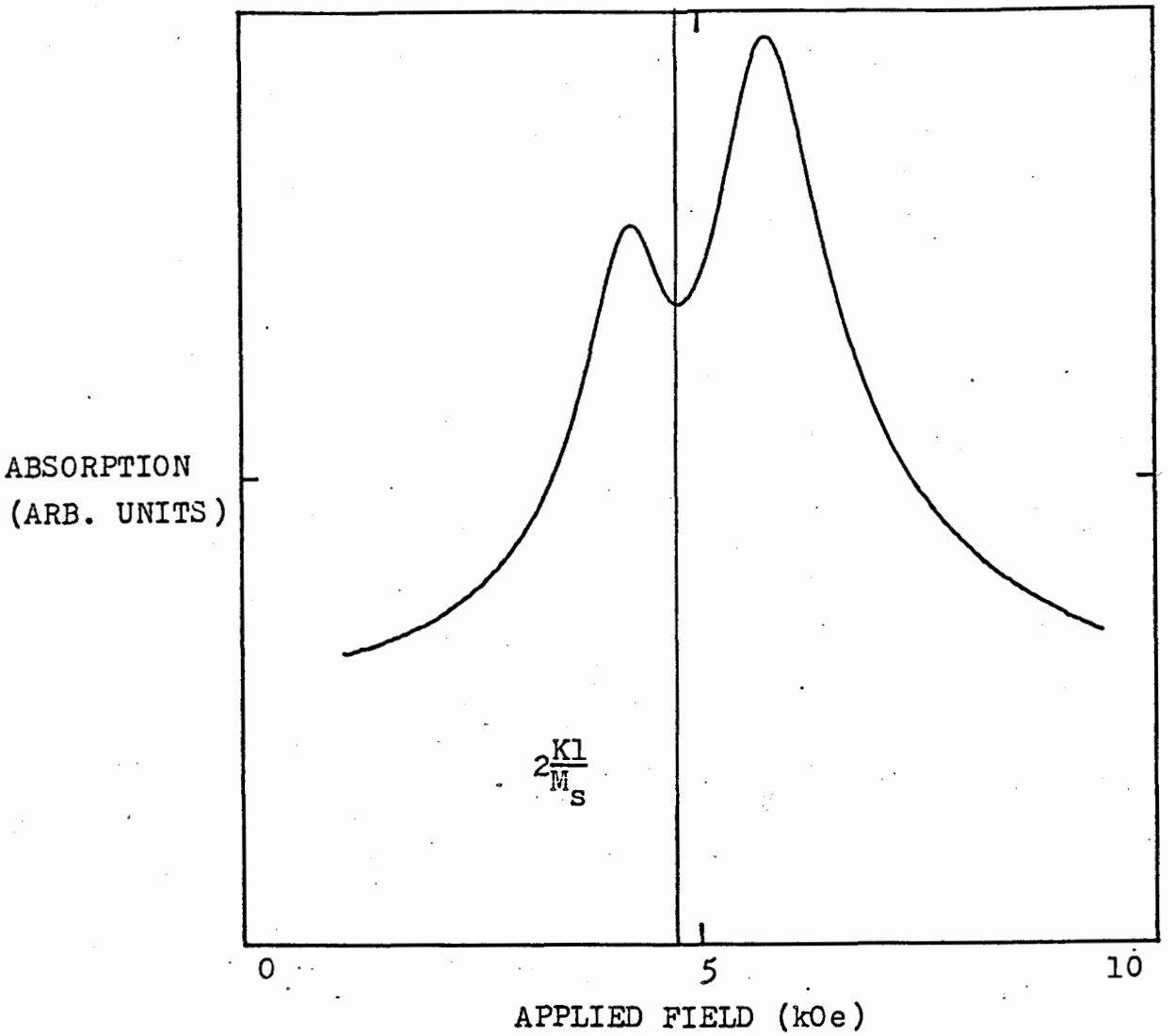

Figure 4.14 Absorption curve at 9.495 GHz, at 4.2 K, sample 1. The applied field was parallel to the (100) axis. The field $2|K1|/M_s$ at which the magnetization becomes parallel to the applied field is indicated on the figure. The double peak is an effect of dragging of the magnetization.

angle of, very approximately, 10° between the field and the (100) direction. This is also a result of the dragging of the magnetization due to MCA, see the discussion in Section 2.3.

The resonance field and the linewidth for the main peak were H_{fmr} = 5.76±0.05 kOe and ΔH = 790±50 Oe. The values of the resonance field and linewidth calculated using program III with a non-local conductivity and a wavenumber dependent damping using the parameters which described the 23.95 GHz linewidth, a = 1.07×10^8 sec^{-1}, b = 1.19×10^8 sec^{-1} and l_D = 620 A, were 5.80 kOe and 830 Oe respectively. These values are in good agreement with the experimental values. The agreement between lineshapes calculated assuming a wavenumber dependent or a wavenumber independent damping and the main peak was similar to that of the comparisons with the 23.95 GHz data shown in Figures 4.11 and 4.12.

4.5 Results at Intermediate Temperatures

The Temperature Dependence of the Linewidth

The temperature dependence of the FMR linewidth for sample 1 for the three axes is shown in Figure 4.15. We found that the linewidths for the (100) and (111) directions for temperatures greater than approximately 60 K were the same within experimental uncertainty. As discussed in Section 4.4 the (111) linewidth at 4.2 K was larger than the (100)

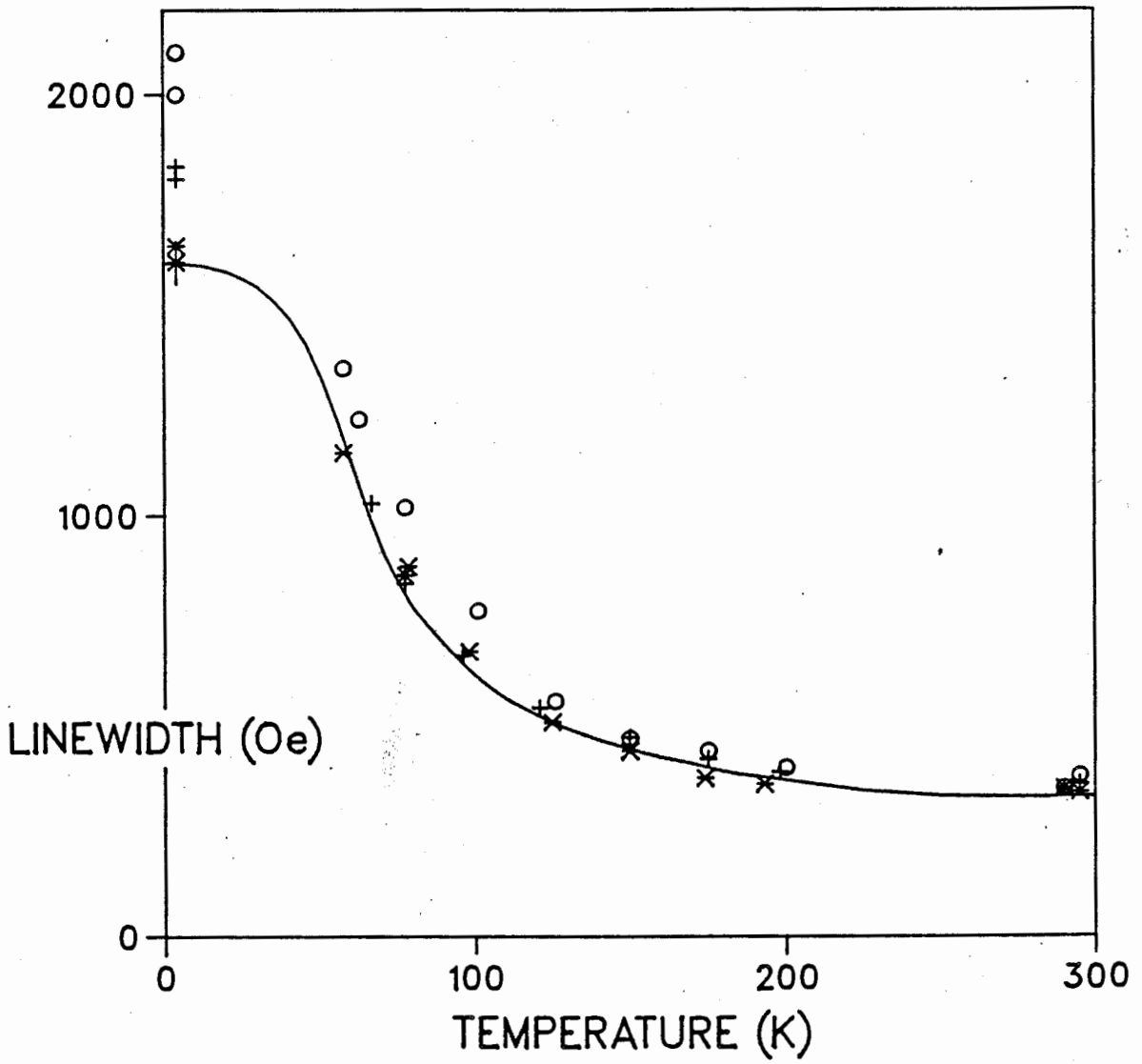

Figure 4.15 The variation of the FMR linewidth, ΔH, with temperature for the three principal crystal axes, 23.95 GHz, (100) ; (111) ; (110) . The uncertainty in the linewidth for temperatures below 100 K was ±50 Oe. To avoid confusion in the plot a single error bar is shown at 4.2 K. The solid line is the data of Bhagat and Lubitz[13] scaled by the ratio of the microwave frequencies, 23.95/22.

linewidth. The linewidth for the (110) direction was the same as the (100) and (111) linewidths at room temperature but was larger than the (100) and (111) linewidths at 200 K and below for this sample.

The solid line in Figure 4.15 is the data of Bhagat and Lubitz[13] at 22 GHz, scaled by the ratio of our microwave frequency to theirs, 23.95/22. The validity of this scaling is discussed in Section 4.6. This data was taken from Figure 15 of [13] (a larger version of Figure 5 of [12]). The data of Bhagat and Lubitz matches our (100) and (111) data quite well at temperatures above 60 K, and our (100) linewidth at 4.2 K, if the difference in the microwave frequency is considered. We are unable to say anything about the saturation of the linewidth from our data, however the close correspondence with the data of Bhagat and Lubitz is suggestive. The temperature variation of the linewidth is discussed in Section 4.6 below.

The Temperature Dependence of H_{fmr}

The variation with temperature of the resonance field for the three principal axes is shown in Figure 4.16. The solid lines are the no-exchange no-damping values of H_{fmr} calculated using the MCA constants of Tokunaga[67]. The inset to Figure 4.16 is included to demonstrate the effect of the higher order MCA constants on the resonance position. Curves are shown in the inset for a calculation made using only K1 and a

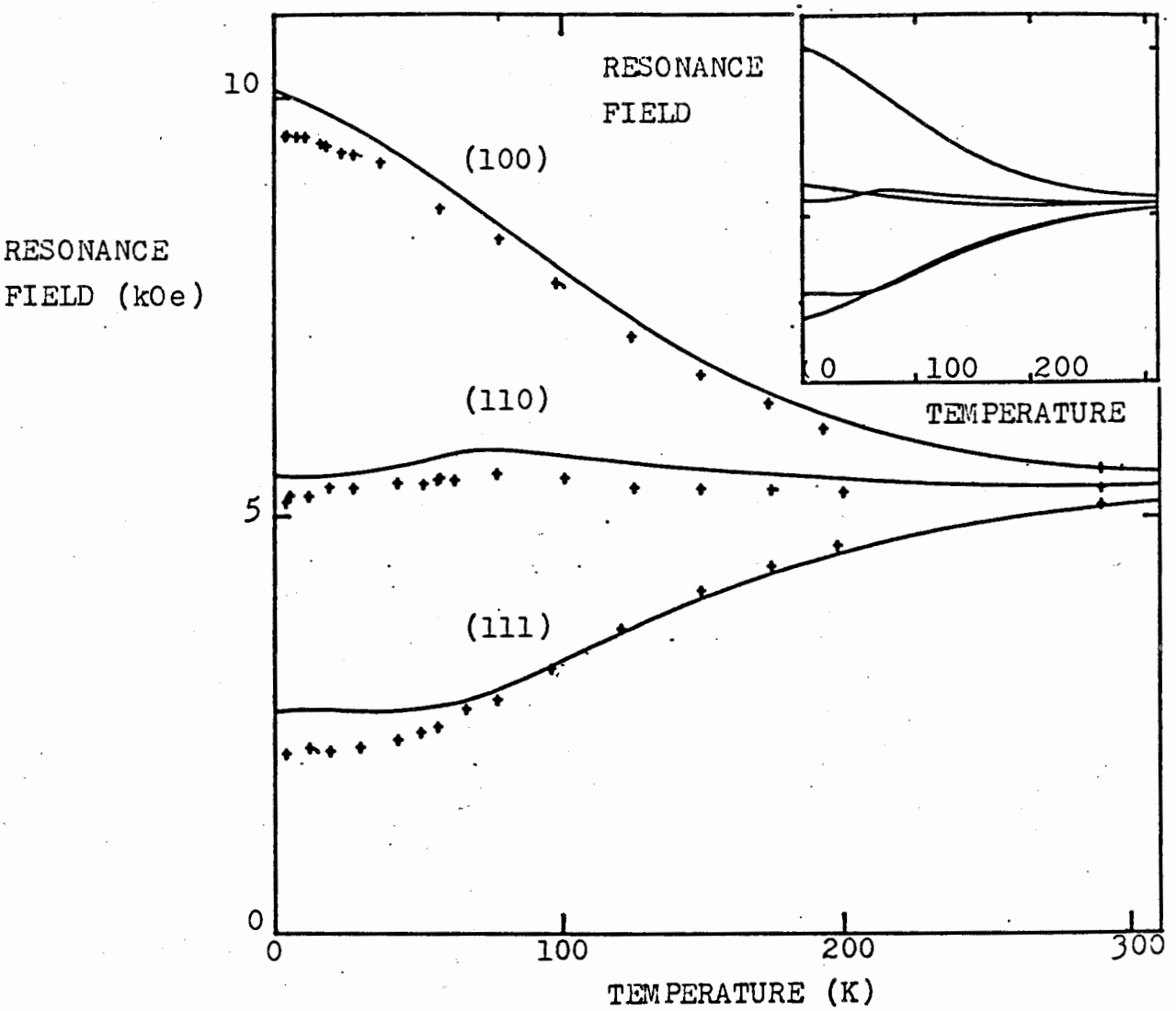

Figure 4.16 The variation of the resonance field, H_{fmr}, with temperature for the three principal crystal axes, 23.95 GHz. The experimental uncertainty is indicated approximately by the symbol size. The solid lines represent the no-exchange no-damping values of H_{fmr} calculated using K1, K2 and K3. The inset shows the no-exchange no-damping values of H_{fmr} calculated using K1 only compared with the calculation using K1, K2 and K3 to demonstrate the effect of the higher order MCA constants on the resonance position.

calculation which used K1, K2 and K3. It is clear from this plot that the higher order MCA constants are important in determining H_{fmr} in Nickel at low temperatures. These calculated lines are shown because they are simple to calculate and because they demonstrate, in a qualitative manner, the temperature dependence which may be expected for H_{fmr}. Tokunaga's MCA constants are used because they are available for the whole temperature range, room temperature to 4.2 K. As pointed out in Section 4.1 there is a discrepancy between the higher order MCA constants of Tokunaga and those of Tung et al[21] at the temperatures at which they can be compared. Because of the uncertainty in the values of the MCA constants it is difficult to extract any information from this data. If we wished to determine values for the MCA constants from this data we would have to know the damping and exchange shifts. Conversely if we wished to determine the damping and exchange shift we would need to know the MCA constants accurately. We know the MCA constants at 77 and 4.2 K well and so are restricted to those temperatures for an analysis of the damping and exchange shifts. These are discussed in Section 4.6.

4.6 Discussion

In this Section we discuss the results which have been presented thus far in this Chapter. First we discuss our linewidth data, how it compares with that of other workers and the implications of our measurements. Then we discuss the consequences of a wavenumber dependent damping of the form of equation (4.3) for the temperature dependence of the linewidth and the resonance field.

Let us start by summarizing our linewidth results. At room temperature and for 23.95 GHz we found that the linewidths were an average of 40 Oe larger than the ideal linewidth of 320 Oe. The linewidth for sample 1 was isotropic within 15 Oe, while there was a 40 Oe spread in the linewidths for the different crystal axes for sample 2. The frequency dependence of the linewidth for this sample showed that the (110) linewidths were consistently larger than the (100) and (111) linewidths by an amount roughly equal to the experimental uncertainty. The frequency dependence of the linewidth was consistent with a surface anisotropy of $K_s = -0.1$ erg/cm^2.

The (110) linewidth for sample 1 was larger than the (100) and (111) linewidths for this sample at 200 K, the highest temperature measured below room temperature. The (100) and (111) linewidths were the same at all temperatures above 60 K. At 77 K the (110) linewidth for both samples was approximately 16% larger than the (100) and (111) linewidths at that

temperature. At 4.2 K the (110) linewidth was 2050±50 Oe, the (111) linewidth was 1815±50 Oe and the (100) linewidth was 1620±50 Oe. The linewidths for the two samples were in good agreement at all temperatures.

The low temperature data available for comparison includes the measurement of Franse[28] at 77 K, the measurements of Anders, Bastian and Biller[17] at temperatures from 77 K to 630 K and the measurements of Bhagat and Hirst[1] and Bhagat and Lubitz[12,13] at temperatures from 4.2 K to room temperature.

Franse[28] measured a linewidth of 1200 Oe at 23.3 GHz at 77 K. He does not state the orientation of the magnetic field for this measurement. Franse's room temperature linewidth was 600 Oe or approximately twice the linewidth due to the intrinsic damping and exchange conductivity. Presumably part of his large 77 K linewidth was due to the increase in the intrinsic damping and part was due to whatever was responsible for the extra linewidth at room temperature. This linewidth is larger than our (110) linewidths at this temperature, 1020 Oe, and our (100) and (111) linewidths, 860 Oe.

Anders et al[17] made measurements on carefully annealed and electropolished (110) Nickel disks. They measured the linewidth for the three principal crystal directions at 9.19, 19.67 and 26.2 GHz at temperatures from 77 K to 630 K. Their room temperature lines were narrow, being 350 Oe at 26.2 GHz, the ideal linewidth at this frequency. The room temperature linewidths were isotropic within a spread of approximately 50 Oe

at 26.2 GHz. They found that the (110) linewidth became larger than the (100) and the (111) linewidths at temperatures below 273 K, and that the difference in the linewidths increased with decreasing temperature. At 77 K they had the (110) linewidth equal to 820 Oe, and the (111) linewidth equal to 640 Oe at 26.2 GHz. No value for the (100) linewidth is quoted at this frequency but it appears from the data for the other frequencies that there was no significant difference between the (111) and (100) linewidths. Our observations as to the anisotropy of the linewidth are in agreement with Anders et al. Their 77 K linewidths are much narrower than those measured by us and by Bhagat and Lubitz[12,13]. They do not quote a resistivity ratio for their samples. It is likely that their Nickel was less pure than ours or that of Bhagat and Lubitz. Since the linewidth increases with increasing resistivity ratio the linewidth for a lower purity sample should increase less rapidly with decreasing temperature than the linewidth for a pure sample. Recall that Lloyd and Bhagat[14] found no increase with decreasing temperature in a 5.4% Copper in Nickel alloy.

Bhagat and Hirst report measurements made on cylinders oriented with a (100) or a (111) direction parallel to the cylinder axis and on (110) disks. The orientation of the applied field in the sample plane for the disk measurements is not stated. Presumably these authors did not make any measurements with the applied field along the (110) direction and so make no comment as to an anisotropy of the linewidth for

this direction as compared with the (100) or (111) directions. They make no mention either of a difference between the (100) and the (111) linewidths at 4.2 K.

Bhagat and Lubitz report measurements on (111) cylinders. To compare our data with that of Bhagat and Lubitz the simplest thing to do is to simply multiply their linewidths by the ratio of the microwave frequencies, 23.95/22. In doing this we ignore the zero frequency intercept in the frequency dependence due to exchange. The exchange contribution to the linewidth is small, and the frequencies are quite close, so the error introduced thereby is negligible. For example at 77 K the error is less than 10 Oe. At 77 K and 4.2 K Bhagat and Lubitz have linewidths of 780 Oe and 1480 Oe respectively. When scaled by the ratio of the frequencies these linewidths become 850 Oe and 1610 Oe respectively, which are in good agreement with our (100) and (111) linewidths at 77 K, 860 Oe, and with our (100) linewidth at 4.2 K, 1620 Oe. Our (111) linewidth at 4.2 K, 1815 Oe, is larger than that of Bhagat and Lubitz.

We need to ask what else besides an anisotropy in the intrinsic damping could produce the observed anisotropy in the linewidth, especially the difference between the (100) and (111) linewidths at 4.2 K. It is unlikely that it could be due to any strain in the surface due to the surface preparation or to strain in the sample induced by the mounting used since the anisotropy for the (111) and (100) directions appears only at temperatures below 60 K. If the anisotropy were produced by

strain it would be expected that the (100) axis, being the hard MCA axis, would be affected more than the (111) axis, which is the easy MCA axis, with the result that the (100) linewidth would be greater than the (111) linewidth because of effects due to the misalignment between the magnetization and the applied field. I can think of no experimental factors which would produce a temperature dependence of the (100) and (111) linewidths similar to that which we have observed.

With the qualification that the measurements were made on samples cut from the same boule, so that the effect may be a result of a peculiarity of the sample, we conclude that the effect is real and is due to an anisotropy of the damping parameter. The disagreement between our (111) linewidths and those of Bhagat and Lubitz remains unexplained. It would be worthwhile to repeat our measurements on samples cut from a different single crystal to be absolutely sure that the difference between the (100) and (111) linewidths at 4.2 K is not a sample dependent effect. In any event the anisotropy for the (110) linewidth appears well established since it has been observed by both Anders, Bastian and Biller and by us.

The Wavenumber Dependent Damping

We now wish to examine the consequences of a wavenumber dependent damping of the form:

$$G(q,T) = a(\sigma_0(T)/\sigma_0(295))\arctan(ql_D)/ql_D + b\rho(T)/\rho(295) \qquad (4.3)$$

We will discuss the temperature dependence of the linewidth, ΔH, and the shift in the position of the resonance, δH, defined as the difference between the value of H_{fmr} expected using (4.3) and the no-exchange no-damping value of H_{fmr}. It is straightforward to compare the calculated temperature dependence of the linewidth with experiment, however it is difficult to compare the shift, δH, because the resonance is also shifted by MCA. The MCA shifts are much larger than the damping and exchange shifts, δH. For example at 4.2 K the MCA shift for the (100) direction, $2|K1|/M_s$, is 4.92 kOe while the damping and exchange shift is of the order of 300 Oe, from the numbers in Table 4-5. To compare the calculated shifts with experiment we would need to know the MCA shifts accurately. Conversely, to determine the MCA constants from our data we would need to know the damping and exchange shift.

Cochran and Heinrich[37] fitted the temperature dependence of the damping parameter deduced from FMAR transmission experiments with the limiting form of (4.3) for small q:

$$G(T) = a(\sigma_0(T)/\sigma_0(295)) + b\rho(T)/\rho(295)$$

Their values of a and b were $a = 1.07\times10^8$ sec^{-1} and $b = 1.19\times10^8$ sec^{-1}. Rather than trying to fit the temperature

dependence of our linewidths we will display some representative possible calculated temperature dependences. At room temperature (295 K) $ql << 1$ so that:

$$G(q,295) = a + b$$

Taking the value of $G = 2.45 \times 10^8$ sec^{-1} at room temperature, we have a constraint on the values of a and b which may be used in (4.3), i.e. $(a + b) = 2.45 \times 10^8$ sec^{-1}. We impose as a second constraint on the parameters entering (4.3) that the calculated linewidth equal the average of our (100) linewidth at 4.2 K, 1620 Oe. So for a given value of a the values of b and of l_D at any temperature are fixed. We have chosen values of $a = 0.8$, 1.2, and 2.0×10^8 sec^{-1} as covering a wide range of ratios of intra-band to inter-band scattering at room temperature. The values of b, and of l_D at room temperature, corresponding to these values of a were $b = 1.65$, 1.25, and 0.45×10^8 sec^{-1}, and $l_D = 10$, 16, and 28 A respectively.

In figure 4.17 the linewidth calculated using program III with a non-local conductivity and a wavenumber dependent damping with the three sets of parameters a, b, and l_D is plotted as a function of the logarithm of the resistivity ratio $\rho(T)/\rho(295)$. This is a convenient way of displaying the results since it is the resistivity ratio which enters the damping (4.3). Also shown on the figure is our data for the temperature dependence of the (100) linewidth. Resistivity ratios of 10 and 38 are

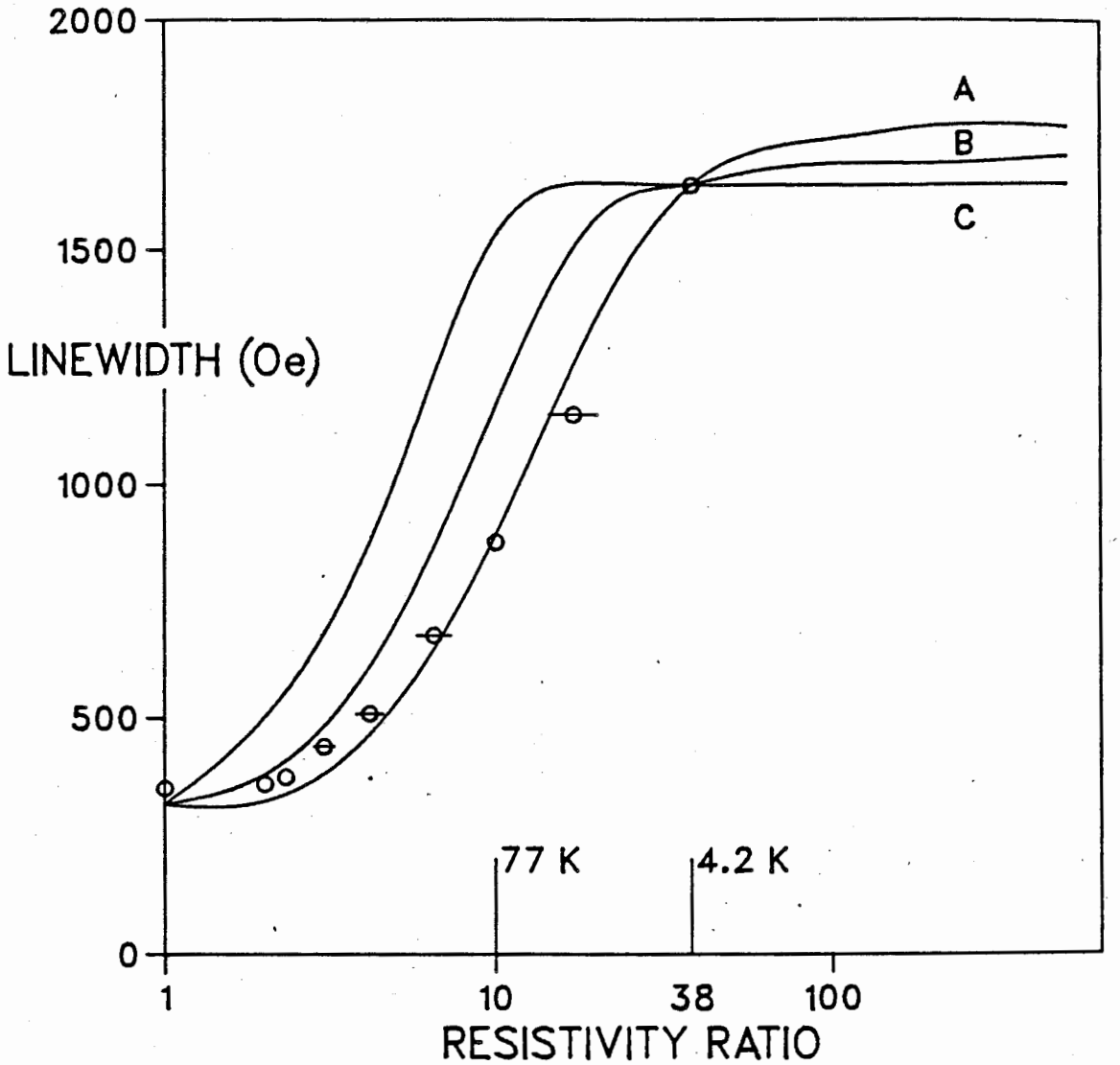

Figure 4.17 The variation of the FMR linewidth with the logarithm of the resistivity ratio. The solid lines were calculated with program III with a non-local conductivity and a wavenumber dependent damping with (A)a = 0.8×10^{8} sec^{-1}, b = 1.65×10^{8} sec^{-1}; (B)a = 1.2×10^{8} sec^{-1}, b = 1.25×10^{8} sec^{-1}; (C)a = 2.0×10^{8} sec^{-1}, b = 0.45×10^{8} sec^{-1}; The circles are the experimental data. Resistivity ratios of 10 and 38 correspond to temperatures of 77 and 4.2 K respectively for our samples.

indicated on the figure, corresponding to 77 and 4.2 K respectively for our samples. A temperature was associated with each resistivity ratio using the resistivity ratios of our samples. The value of the magnetization corresponding to that temperature was used in the calculations. The magnetization is not a strong function of temperature in the temperature range we are considering so the effects of a small inaccuracy in relating the temperature to the resistivity ratio should be negligible.

The calculated variation of ΔH with temperature (resistivity ratio) exhibits the increase with decreasing temperature (increasing resistivity ratio) observed experimentally and the saturation at large resistivity ratios discussed by Bhagat and Hirst[1]. As expected the linewidth saturates at higher temperatures for larger values of a, that is for a larger contribution of the intra-band damping to the total damping at room temperature. For the smallest value of a shown the linewidth had not saturated at a resistivity ratio of 38. The values of ΔH at saturation were ΔH = 1770, 1700 and 1630 Oe respectively for a = 0.8, 1.2, and 2.0×10^8 sec^{-1}.

Comparing our data with these calculated curves it appears that the data follows the temperature dependence calculated assuming a = 0.8×10^8 sec^{-1} reasonably well. Of course there is the problem of the extra linebroadening in our experimental results, but this would not affect our linewidths by more than approximately 40 Oe at any temperature, see the discussions in Sections 4.2, 4.3 and 4.4. The values of a and b which would be

chosen to match the experimental temperature dependence would be close to $a = 0.8 \times 10^8$ sec^{-1} and $b = 1.65 \times 10^8$ sec^{-1}. It would be possible to better define the best values of a and b, but it is probably not worth the large effort.

In Figure 4.18 the damping and exchange shift δH, is plotted as a function of the logarithm of the resistivity ratio for the three sets of a, b and l_D. As in Figure 4.17 resistivity ratios of 10 and 38 have been indicated on the figure. The variation of δH for the three sets of parameters are quite similar, the damping and exchange shift being to lower fields (δH is negative). At a resistivity ratio of 38 the shifts are $\delta H = -200$, -280, and -340 Oe for $a = 0.8$, 1.2, and 2.0×10^8 sec^{-1} respectively.

Before attempting to compare these calculated temperature variations with experiment it is instructive to examine the temperature variation of δH to be expected for a wavenumber independent damping. In Figure 4.19 we have assembled the results of calculations for the following combinations of damping and conductivity:

(a) non-local conductivity, wavenumber dependent damping. For this plot we have used the parameters of Cochran and Heinrich with $l_D = 16$ A at room temperature as in Section 4.4. The variation of δH is similar to that calculated assuming $a = 1.2 \times 10^8$ sec^{-1} in Figure 4.18.

(b) non-local conductivity, wavenumber independent damping $G = 2.45 \times 10^8$ sec^{-1}. This is the variation of δH which would be

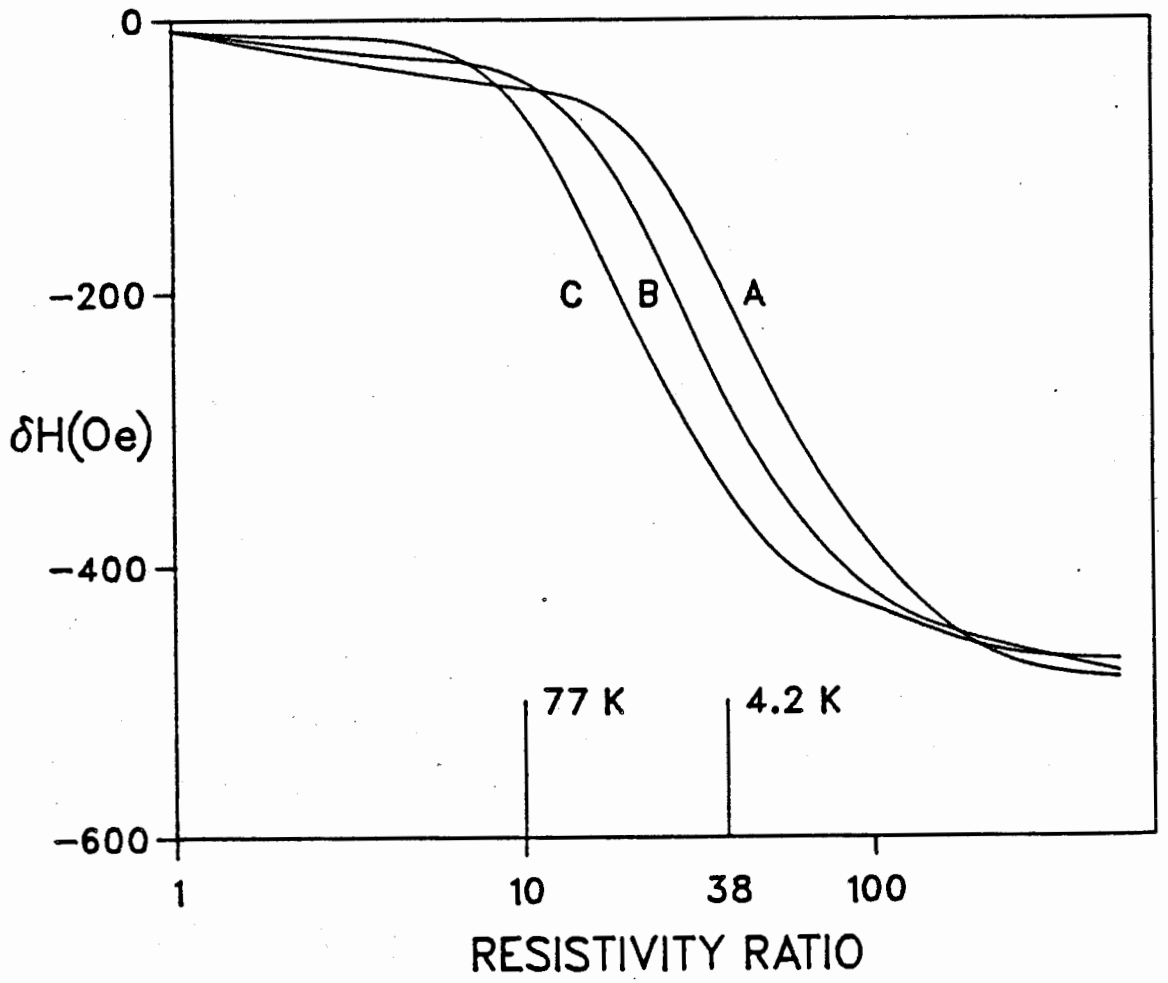

Figure 4.18 The variation of the shift, δH, with the logarithm of the resistivity ratio. The shift is defined as the difference between the no-exchange no-damping value of H_{fmr} and that calculated with program III. A non-local conductivity and a wavenumber independent damping was assumed, with (A)a = 0.8×10^8 sec^{-1}, b = 1.65×10^8 sec^{-1}; (B)a = 1.2×10^8 sec^{-1}, b = 1.25×10^8 sec^{-1}; (C)a = 2.0×10^8 sec^{-1}, b = 0.45×10^8 sec^{-1}; Resistivity ratios of 10 and 38 correspond to temperatures of 77 and 4.2 K respectively for our samples.

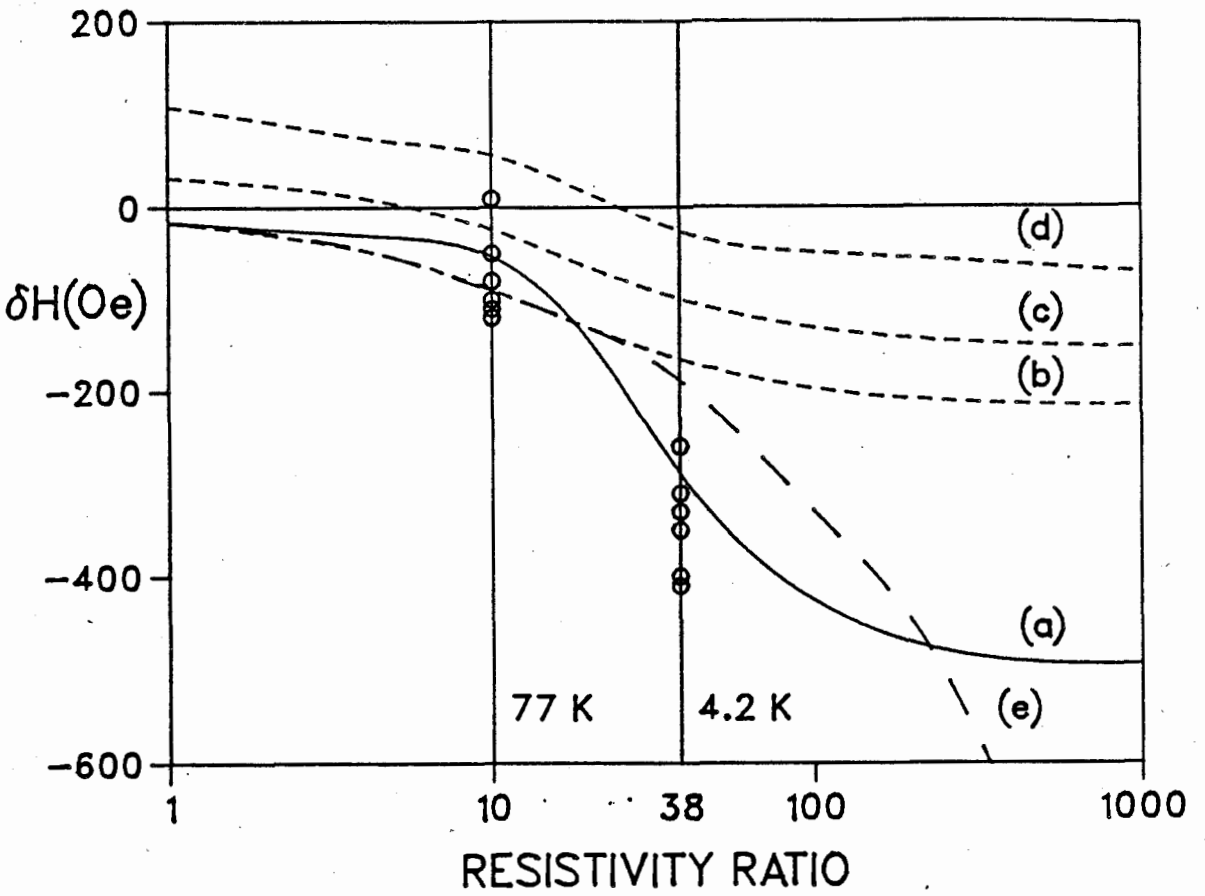

Figure 4.19 The variation of the shift, δH, with the logarithm of the resistivity ratio. The curves were calculated assuming: (a) non-local conductivity, wavenumber dependent damping; (b) non-local conductivity, wavenumber independent damping $G = 2.45 \times 10^8$ sec^{-1}; (c) non-local conductivity, wavenumber independent damping $G = 8.0 \times 10^8$ sec^{-1}; (d) non-local conductivity, wavenumber independent damping $G = 14 \times 10^8$ sec^{-1}; (e) local conductivity, wavenumber independent damping $G = 2.45 \times 10^8$ sec^{-1}. The circles are the experimental data at 77 and 4.2 K. Resistivity ratios of 10 and 38 correspond to temperatures of 77 and 4.2 K respectively for our samples.

expected for a material having a temperature independent damping equal to that of Nickel at room temperature.

(c) the same as (b) except that $G = 8.0 \times 10^8$ sec^{-1}, approximately the damping parameter required to reproduce the linewidth in Nickel at 77 K.

(d) The same as (b) except that $G = 14 \times 10^8$ sec^{-1}, the damping parameter required to reproduce the (100) linewidth in Nickel at 4.2 K.

(e) to demonstrate the effect of a local vs a non-local conductivity curve (e) has been calculated assuming a local conductivity with $G = 2.45 \times 10^8$ sec^{-1}. This curve is useful because it gives a rough idea of the temperature at which the effects of a non-local conductivity become important, curves (b) and (e) diverge at a resistivity ratio of approximately 20. The crosses on the Figure are the experimental shifts at 77 and 4.2 K calculated using the MCA constants of Tung et al[21]. These shifts were obtained by subtracting Calc. A in Tables 4-4 and 4-5 from the experimental values of H_{fmr}.

The magnetic damping in Nickel is temperature dependent. A feeling for the temperature variation of δH if a wavenumber independent damping were assumed can be obtained by looking at curve (b) at room temperature, curve (c) at 77 K (resistivity ratio = 10) and curve (d) at 4.2 K (resistivity ratio = 38). The shift is small and not strongly dependent on temperature. On the other hand the shift due to the wavenumber dependent damping, curve (a), is strongly temperature dependent and much

larger than for a wavenumber independent damping. We may compare these calculated shifts with experiment at 77 K and 4.2 K where the MCA shifts are known with reasonable certainty. From Table 4-4 the shift δH at 77 K varies from +10 to -120 Oe. From Table 4-5 the shift at 4.2 K varies from -260 to -430 Oe. At 77 K the difference between the calculated shifts for a wavenumber dependent and a wavenumber independent damping are small so that it is not possible to choose between the two forms of the damping from the experimental values. However at 4.2 K the wavenumber dependent damping shift is in much better agreement with experiment than the wavenumber independent damping shift, as evidenced by the data on the figure.

Rather than comparing the calculated shifts with experiment we may approach the problem from a different direction and ask how the values of the MCA constants deduced from experiment assuming the two different forms of the damping compare with accepted values. If a wavenumber dependent damping was assumed the value of $K1'$ obtained from the position of the resonance for the (100) direction would be in good agreement with the value of Tung, Said and Everett[21], $K1' = -12.44 \times 10^5$ erg.cm^3. If a wavenumber independent damping was assumed the value of $K1'$ would be $K1' = -11.5 \times 10^5$ erg.cm^3. To demonstrate that our results are not a peculiarity of our samples we cite the value of $|K1|/M_s$ of 2150 G quoted by Lloyd and Bhagat[14] at 4.2 K. This corresponds to a value $K1' = -11.3 \times 10^5$ erg/cm^3, in good agreement with our wavenumber independent damping value of $K1'$.

To summarize, the temperature variation of the (100) linewidth was consistent with a wavenumber dependent damping of the form (4.3) with $a = 0.8 \times 10^8$ sec^{-1}, $b = 1.65 \times 10^8$ sec^{-1} and $l_D = 28$ A at room temperature. The damping and exchange shift, δH, also appears consistent with this form of the damping. However the experimental lineshapes and those calculated assuming a wavenumber dependent damping are only in partial agreement, see Figure 4.11.

5. CALCULATION OF THE DAMPING PARAMETER

5.1 Introduction

We now turn from experiment to a consideration of the microscopic origins of magnetic damping. The first part of this chapter contains a qualitative discussion of the effects of spin-orbit coupling on electron states and how spin-orbit coupling may lead to magnetic damping. This is followed by presentation of a calculation of the damping parameter using a simple model of electrons and spin waves coupled through the spin-orbit interaction. The ideas discussed here are largely due to Kambersky[2,70,71,72]. The low temperature damping mechanism has been discussed by Korenman and Prange[3,4,73]. Berger[74] has also presented a theory of magnetic damping applicable to Nickel.

Spin-orbit coupling has two effects on the electron states in a solid, it mixes the spin and it shifts the energy. These two effects lead to two magnetic damping mechanisms with different temperature dependences.

In the absence of spin-orbit coupling a band state is either spin-up or spin-down. In the presence of spin-orbit coupling the band states are not spin eigenstates. A state $|k,n,+\rangle$ where k is the momentum, n the band index and + the spin

index, becomes (following Elliott[10]) ($a_{kn+}|+> + b_{kn+}|->$) and a state $|k,n,->$ becomes ($a_{kn-}|-> + b_{kn-}|+>$) where $|a|$ is >> $|b|$. The constants a and b depend on both k and n. Scattering of an electron by a phonon or impurity results in a change of the spin of the system. Three types of scattering may be distinguished depending on whether the band and spin indices change: (i) an electron in state $|k,n,+>$ scatters to $|k',n,+>$ (intraband scattering), (ii)$|k,n,+>$ scatters to $|k',n',+>$ (interband scattering with no change of spin index), and (iii)$|k,n,+>$ scatters to $|k',n',->$. The third type of scattering (spin-flip scattering) is not possible in the absence of spin-orbit coupling. Since the spin of the system is not conserved it is clear that scattering may lead to magnetic damping. Apparently spin-flip scattering gives the largest contribution to the magnetic damping. The magnitude of the damping depends on the relative magnitudes of the gap between the bands (ΔE) and the reciprocal lifetime of the electrons $\hbar/\tau$. If a single gap is present the damping varies as:

$$G \quad (\hbar/\tau)/((\Delta E - \hbar\omega)^2 + (\hbar/\tau)^2) \qquad (5.1)$$

If $\hbar/\tau$ is << ΔE the damping varies as $1/\tau$. This has been demonstrated by Heinrich, Fraitova and Kambersky[75] who considered the damping introduced by the s-electron d-electron exchange interaction. In a real metal there is a spectrum of energy gaps present ranging from zero at accidental degeneracies

to the full exchange splitting. The damping will consist of a sum of terms like (5.1). It is thought that this mechanism is responsible for the flat temperature dependence of the damping in Nickel between approximately 200 K and 600 K. This mechanism was considered in the damping used in Chapter 4 by the term that varied as the resistivity. For pure metals τ becomes large at low temperatures so that the damping due to this mechanism becomes small.

The other effect of spin-orbit coupling is to shift the energy of an electronic state. This leads to a magnetic damping responsible for a linewidth which has a temperature dependence similar to that observed in Nickel at low temperatures, namely an increase with decreasing temperature leading to saturation at very low temperatures. In a ferromagnetic metal the shifts depend on the direction of the magnetization. Generally the shifts are small, being second order in the spin-orbit coupling parameter ξ[2] which is small (ξ for Nickel is of the order of 0.1 eV[16]). The situation may be quite different if there are degenerate states whose degeneracy is lifted by spin-orbit coupling. The splitting of the bands then depends on the direction of the magnetization with respect to the crystal axes. If the degeneracy is near the Fermi surface the shifts in the energy levels lead to changes in the size and shape of the Fermi surface. The effect of spin orbit coupling on the band structure when degeneracies are present has been discussed by Elliott[10]. His Figures 3-6 demonstrate the effects which may

occur.

A useful picture, and the one which will be used in the calculation of the damping parameter, is to consider the metal as containing collective magnetic excitations (spin waves) and single particle excitations (electrons). Precessional motion of the magnetization may be described in terms of spin wave amplitudes. FMR consists of exciting spin waves by the microwave magnetic field. The spin waves may be described in terms of electron states but such a description need not concern us. The electron and spin wave systems are coupled by spin orbit coupling because the electron energy depends on the direction of the magnetization of the magnetization. Magnetic damping occurs when a spin wave is annihilated in a collision with an electron and the electron is excited into a higher energy state. Energy and momentum must be conserved in such a collision. An estimate of the spin wave energy, momentum and velocity is:

$$E_{sw} = \hbar\omega \simeq 10^{-4} \text{ eV}$$

$$q \simeq 1/\delta \simeq 10^{5} \text{cm}^{-1}$$

$$V_{sw} = \omega/q \simeq 10^{11}/10^{5} = 10^{6} \text{ cm/sec}$$

where ω is the spin wave frequency (the microwave frequency) and δ is the microwave skin depth (see Chapter 2). An estimate of the electron energy, momentum and velocity is:

$$E = E_F \simeq \hbar^2 k_F^2/2m \simeq 4 \text{ eV}$$

$$k = k_F \simeq 2\pi/a \simeq 10^8 \text{cm}^{-1}$$

$$v_F = \hbar k_F/m \simeq 10^8 \text{ cm/sec}$$

where a is the lattice spacing. Clearly $E_{sw} << E$, $q << k$ and $v_{sw} << v_F$. If an electron is excited from a state $\bar{k}$ to a state $\bar{k}'$ in a collision with a spin wave, then, by conservation of energy and momentum we have:

$$\bar{k}' = \bar{k} + \bar{q}$$

$$E' = E + \hbar\omega$$

Combining these two equations:

$$E' - E = (\hbar^2/2m)(2\bar{k}\cdot\bar{q} + q^2) = \hbar\omega$$

or:

$$(\hbar/m)\bar{k}\cdot\bar{q} = \omega$$

$$\bar{v}_F\cdot\bar{q} = \omega$$

where $E = \hbar^2k^2/2m$, and q^2 has been neglected compared with $2\bar{k}\cdot\bar{q}$. v_Fq is approximately 10^{13} while ω is approximately 10^{11} so that:

$$\bar{v}_F \cdot \bar{q} \simeq 0$$

In other words only those electrons whose velocity is approximately perpendicular to that of the spin wave interact with the spin wave. More precisely the component of the electron's velocity parallel to $\bar{q}$ must equal the spin wave phase velocity for an electron spin wave collision to occur. If the electron lifetime τ, due to phonon and impurity scattering, is short the electron momentum is not well defined and the momentum conservation condition is not stringent. The number of electrons which may interact with the spin wave is large but the interaction time is short so that the damping is small. At low temperatures where the lifetime increases the momentum conservation condition is stringent and restricts the number of electrons which may interact with the spin wave. However because the lifetime is long the interaction is much more effective and the total effect becomes large. We may think of the electrons as 'surf-riding' on the spin wave. The energy which the electrons may absorb from the spin waves is limited only by the time of the ride. This leads to a damping which increases with the electron relaxation time as is observed in Nickel.

The calculation which is carried out in this chapter is based on this idea. The X_5 hole pockets in the Fermi surface of Nickel are known to change size and shape with the direction of the magnetization. We consider only those electrons in states

near these pockets. These are minority spin electrons so we consider only electrons of a single spin. We use the Fermi surface of Hodges, Stone and Gold[16], the description of spin waves given by Sparks[6] and the variation of energy levels with the direction of the magnetization given by Gold[76]. These are described in Section 5.2. The approach is to calculate the response of the spin wave system to a magnetic field which varies as $\exp(i(qy-\omega t))$ using the method of Green's functions. This gives the frequency and wavenumber dependent susceptibilty. The imaginary part of this susceptibility is related to the damping parameter. This calculation is presented in Section 5.3. The integrals over the Fermi surface which enter the damping parameter have been evaluated. The results are compared with the calculations of Kambersky and with the experimental results presented in Chapter 4 in Section 5.4. Our calculation is similar to that carried out by Heinrich, Fraitova and Kambersky[75].

5.2 The Model

The Fermi Surface of Nickel

The band structure and Fermi surface of Nickel have been calculated by a number of workers. The calculations of Zornberg[77] are useful for the complete Fermi surface including the effects of spin-orbit coupling. A recent reference is the

work of Weling and Callaway[78]. A schematic sketch of the band structure of Nickel as presented by Gold[69] is shown in Figure 5.1, as well as the band structure near the X points, see below.

Most people in the field seem to agree as to the large features of the Fermi surface although there are a few small areas whose existence is still a matter of discussion. The large features include six distinct sheets. There are two sheets of predominantly s-character, a majority spin sheet and a minority spin sheet. The two sheets are similar in shape having pronounced 'bulges' in the (111) directions. The majority spin sheet contacts the Brillouin zone edge in the (111) directions with the formation of 'necks' similar to those of the Fermi surface of copper. There is a predominantly d-character minority spin sheet with 'bulges' in the (110) directions. These three sheets are centered in the Brillouin zone. There are three minority spin sheets centered about the X-points of the Brillouin zone (the X-points are located at $2\pi/a(\pm1,0,0)$, $2\pi/a(0,\pm1,0)$ and $2\pi/a(0,0,\pm1)$). These sheets arise from the X_5 d-band. They are much smaller than the other three sheets above, they are approximately ellipsoidal in shape and have hole-like character. These are the X_5 hole pockets which form the focus of this chapter. There is a possibility that small hole pockets at the X-points arising from the minority spin X_2 level may exist. The X_2 level is close to the Fermi level and may be shifted, in a calculation, above or below with small

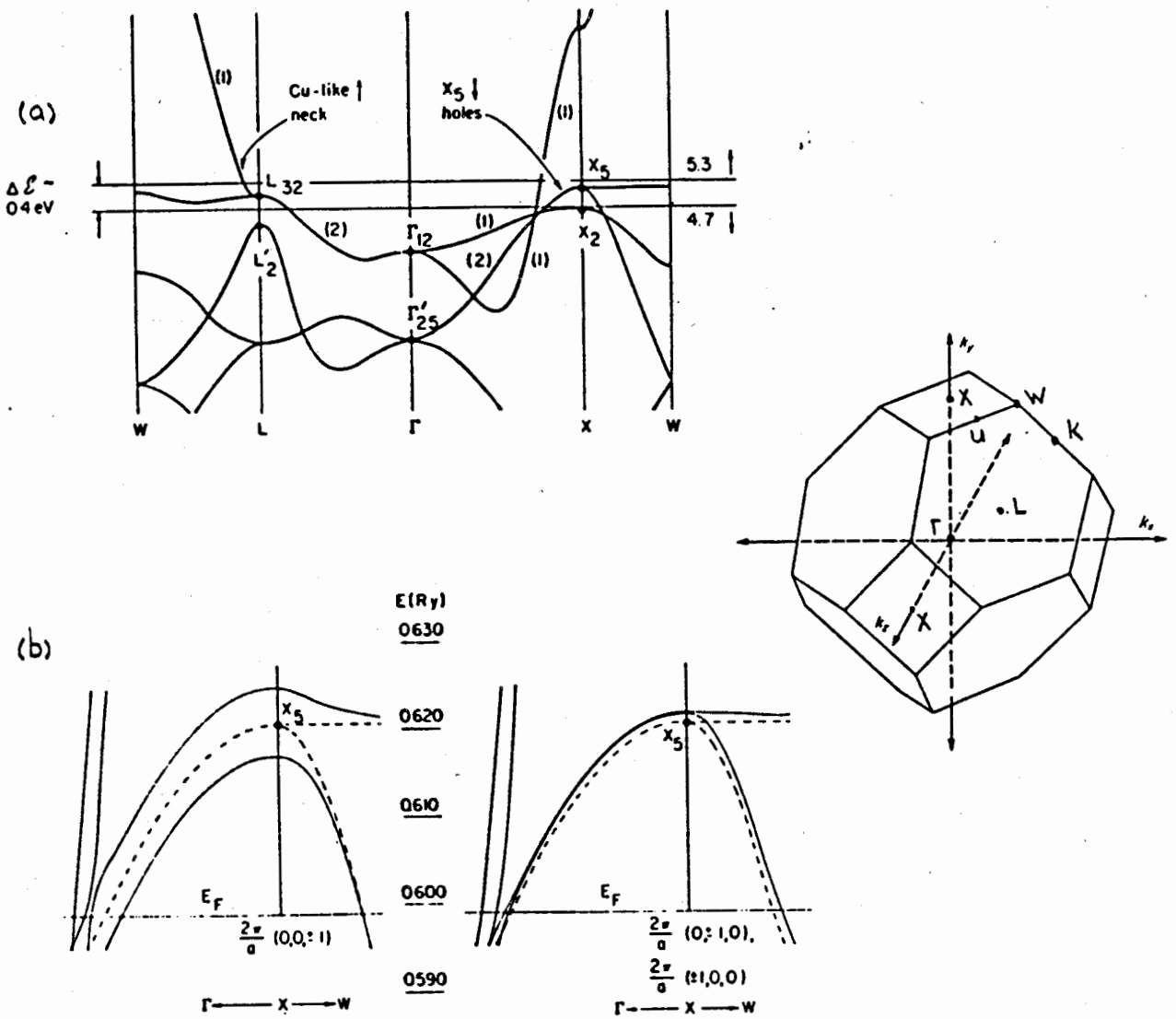

Figure 5.1 (a)A schematic sketch of the energy bands of Nickel as presented by Gold[69].

(b)The band structure at the Fermi level near the X points as given by Hodges, Stone and Gold[16]. The magnetization is parallel to [001]. Solid curve: ξ = 0.1 eV; Dashed curve: ξ = 0.

Inset Directions in the reciprocal lattice of a face centered cubic lattice.

changes in parameters, see Figure 5.1 where the X_2 level appears just below the minority spin Fermi energy. The only experimental evidence for the existence of these pockets is the torque measurements of Gersdorf[44] and Tung et al[21].

According to Zornberg degeneracies in the band structure occur near the L-points ((111) directions), along Λ (Γ - L), along Δ (Γ - X) and at accidental degeneracies due to band crossings which occur when the exchange splitting is added to the band calculation. The band structure in the rest of the Brillouin zone is largely independent of magnetic field direction.

In the absence of spin-orbit coupling the X_5 level is doubly degenerate. The degeneracy is lifted by spin-orbit coupling, the splitting of the levels depending on the angle between the magnetization and the (100) axis of interest. Since the position in k-space where the band crosses the Fermi level changes with the direction of the magnetization, the dimensions of the Fermi surface change.

This change in size and shape of the Fermi surface with the direction of the magnetization was first invoked to explain unusual de Haas-van Alphen results (Hodges,Stone and Gold[16], this paper will be referred to as HSG). These authors produced a band structure and a Fermi surface using the interpolation scheme of Hodges, Ehrenreich and Lang[79] which fitted the dHvA data from the pockets well. The calculated band structure did not fit the results for the rest of the Brillouin zone well.

However since we are interested only in the hole pockets we will use the Fermi surface parameters of HSG.

Dimensions of the hole pockets at the different X-points for the magnetization along [001], [111] and [110] are listed in Table 5-1. These numbers are taken from Table 1 of HSG. Also listed in Table 5-1 are values of the spin-orbit coupling parameter ξ, the Fermi energy E_F and the energy of the X_5 level at the X-point in the absence of spin-orbit coupling, E_X, quoted by HSG. Effective masses m_1^* for the direction k_{XW} and m_2^* for the direction $k_{X\Gamma}$ in the absence of spin-orbit coupling are listed, as well as the Fermi velocity appropriate for E_F and m_1^*. The band structure at the Fermi energy near the X-points is shown in Figure 5.1 and the X_5 pockets are illustrated in Figure 5.2 when M_S points along [001]. The pockets are shown in the presence and absence of spin-orbit coupling. Different authors quote different dimensions for the pockets. For example Weling and Callaway quote values of $k_{X\Gamma}$ ranging from 0.195 to 0.256 times $2\pi/a$ in the absence of spin-orbit coupling. A comprehensive discussion of the pockets is given by Zornberg[77].

To calculate the damping parameter we need to know the dimensions of the Fermi surface and how the energies depend on the direction of the magnetization. Gold[76] has given a simple analysis of the dependence of the energy levels on the direction of the magnetization. By considering only the degenerate levels and neglecting any mixing from other states at the X-points and

TABLE 5-1

Distances from X to the surface of the hole pocket in units of $2\pi/a$, where a=3.5166 A (Hodges, Stone and Gold)

ξ = 0.1 eV

Field Direction	Location of pockets	$k_{X\Gamma}$	k_{XW}	k_{XU}
[001]	(0,0,±1)	0.195	0.100	0.094
	(±1,0,0)	0.220	0.112	0.108
	(0,±1,0)			
[111]	(0,0,±1)	0.208	0.107	0.098
	(±1,0,0)			
	(0,±1,0)			
[110]	(0,0,±1)	0.219	0.109	0.103
	(±1,0,0)	0.205	0.106	0.102
	(0,±1,0)			
ξ=0		0.215	0.102	0.095

Band Parameters for ξ = 0

E_X = 8.45 eV $\quad$ E_F = 8.15 eV

$m_1^*(k_{XW})$ = 0.42 m $\quad$ $m_2^*(k_{X\Gamma})$ = 1.86 m

m = free electron mass

$v_F(m_1^*) = 5.6 \times 10^7$ cm/sec

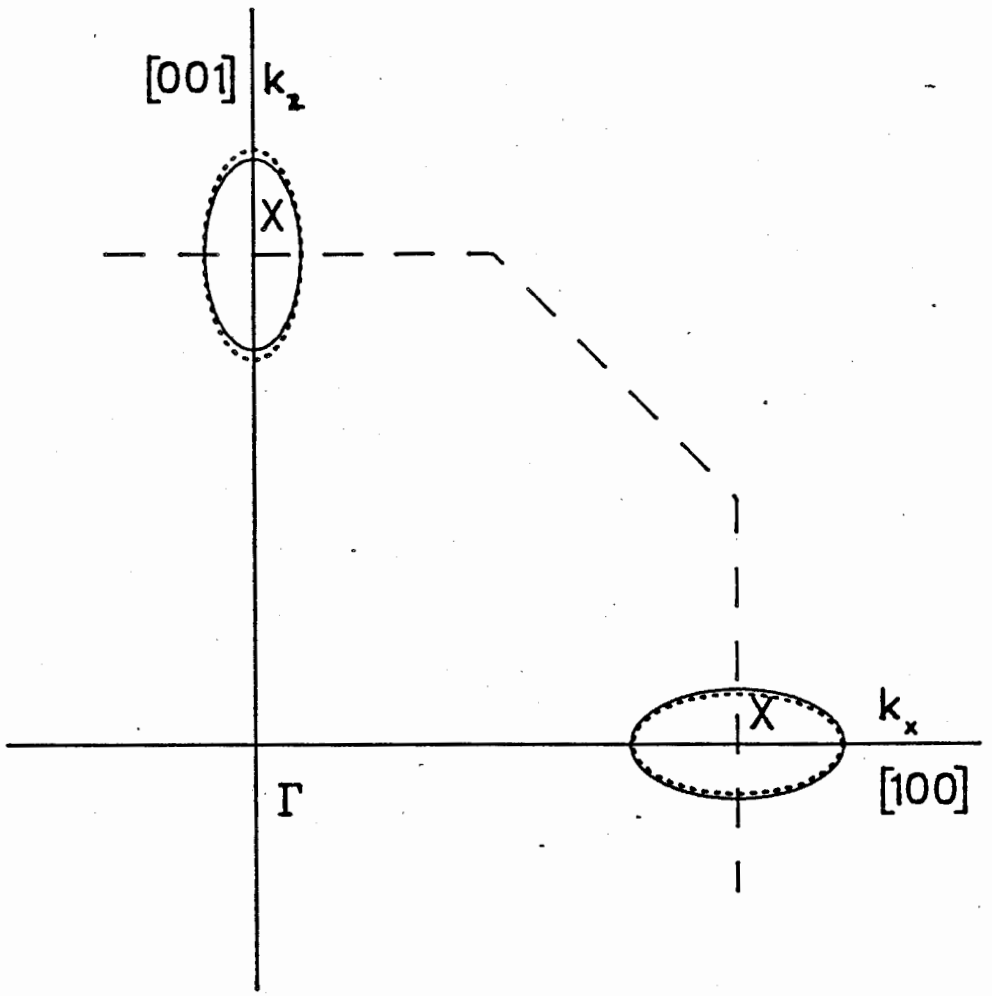

Figure 5.2 The X_5 hole pockets in the Fermi Surface of Nickel, based on the parameters of HSG. In this plot the pockets at $2\pi/a(1,0,0)$ and $2\pi/a(0,0,1)$ are shown. The magnetization points along [001]. The dotted curves represent the Fermi Surface in the absence of spin-orbit coupling. The solid curves represent the Fermi Surface with ξ = 0.1 eV. The boundary of the Brillouin zone is shown.

treating spin-orbit coupling as a perturbation he found that:

$$E(k) = E_0(k) - (\xi/2)\cos(\theta_M) \qquad (5.2)$$

where $E_0(k)$ is the energy in the absence of spin-orbit coupling, ξ is the spin-orbit coupling parameter and θ_M is the angle between the magnetization and the (100) axis being considered. According to this picture if the magnetization is along [001] the levels at [100] and [010] should not be shifted. This is not true as can be seen from Table 5-1 and Figure 5.2. The difference is small however and the expression (5.2) will be used in the discussion which follows.

Neglecting the light fluting of the hole pockets, ie considering them as ellipsoids with major axis $k_{X\Gamma}$, and minor axis k_{XW}, the energy of electrons near the X-points may be written:

$$E(k) = E_X - (\xi/2)\cos(\theta_M) - \hbar^2/2(k_x^2/m_1^* + k_y^2/m_1^* + k_z^2/m_2^*) \qquad (5.3)$$

where k is measured from the X-point and the k_z axis is along the Γ-X axis of the pocket being considered. These simplified pockets change size, but not shape, with changes in the direction of the magnetization.

Geometry for the Calculation

We now address the problem of actually calculating the damping parameter for the low temperature damping mechanism. The approach is to evaluate the microwave susceptibility using the method of Green's functions (see below). The imaginary part of the susceptibilty is related to the damping parameter.

The geometry assumed is shown in Figure 5.3. The sample forms a slab of infinite extent lying in the x-z plane. The external field and the magnetization point along the z-direction. We consider only cases where a principal crystal axis is parallel to z. As was demonstrated in Section 2.3 the magnetization will then be parallel to the applied field if the magnitude of the applied field is greater than some critical value. Microwaves travel in the +y-direction with the microwave magnetic field in the x-direction. The time and space variation $\exp(i(qy-\omega t))$ is assumed. This geometry is essentially the same as that of the calculations outlined in Chapter 2, Sections 2.1 and 2.3, however the coordinate system has been changed so that the magnetization points in the z-direction (for quantum mechanical reasons). Only small deviations of the magnetization from equilibrium are considered. The components of the magnetization are (m_x, m_y, M_s) to first order in the small quantities m_x and m_y.

There are three principal crystal axes (100), (110) and (111). In our experiments the samples were cut with a

[1$\bar{1}$0] axis normal to the sample plane. We could measure FMR with the applied field parallel to [001], [110] or [111] with the spin wave wavevector q along [$\bar{1}$10]. Experiments may also be performed on samples cut with an [010] axis normal to the sample plane. The [010] plane contains the [001] and [101] crystal axes. An experiment performed with a [010] normal sample with the applied field along the [001] axis is not equivalent to an experiment performed with a [1$\bar{1}$0] normal sample and the applied field along [001] as the direction of the spin wave wavevector with respect to the crystal axes is different. Thus there are five orientations of the crystal axes of interest: with the sample plane being a [010] normal crystal plane, (i) M_s parallel to the [001] axis, (ii) M_s parallel to the [101] axis; with the sample plane being a [1$\bar{1}$0] normal crystal plane, (iii) M_s parallel to the [001] axis, (iv) M_s parallel to the [111] axis and (v) M_s parallel to the [110] axis. Case (i) is shown in Figure 5.3(a) and case (iii) in Figure 5.3(b).

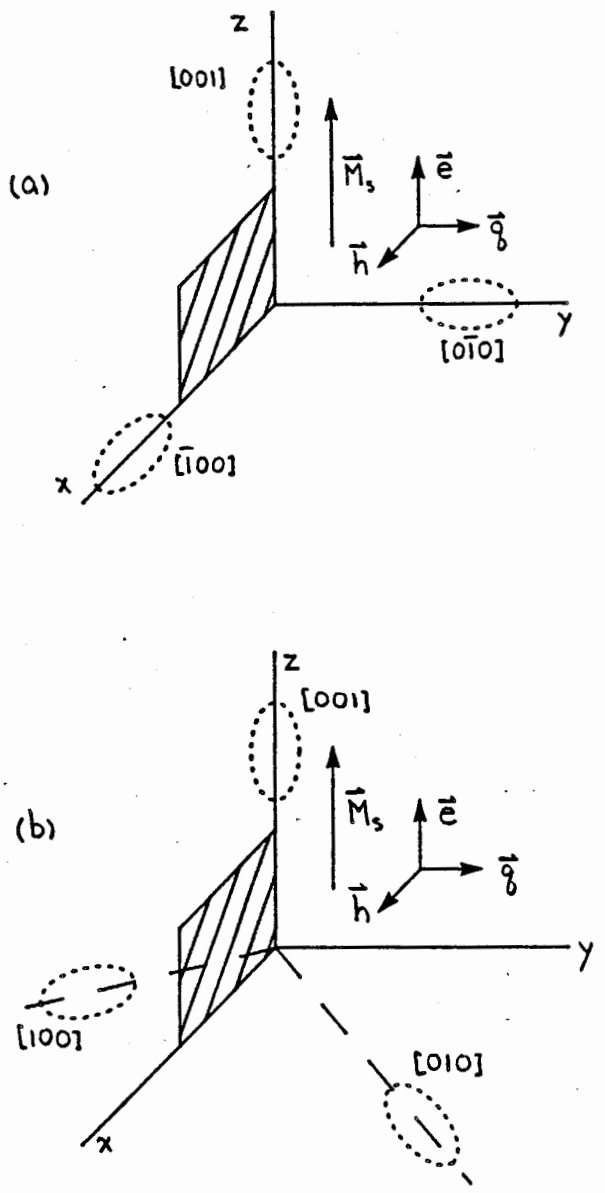

Figure 5.3 The geometry assumed for the calculation of the damping parameter. The X_5 hole pockets are indicated on the figures.

(a) case (i) of the text, the sample normal is [010], the [001] axis is parallel to the z-axis.

(b) case (iii) of the text, the sample normal is [1$\bar{1}$0], the [001] axis is parallel to the z-axis.

The Hamiltonian

To carry out the calculation we need the Hamiltonian which describes the model system. This consists of three parts: the spin wave Hamiltonian, the electron Hamiltonian and the interaction Hamiltonian. Following Sparks[6] the spin wave Hamiltonian may be written:

$$H_{sw} = \Sigma\, A_q b_q^\dagger b_q + 1/2(B_q b_q b_{-q} + B_q^* b_q^\dagger b_{-q}^\dagger) \qquad (5.4)$$

$$A_q = \gamma\hbar(H + 2\pi M_s \sin^2\theta_q + 2Aq^2/M_s)$$

$$B_q = \gamma\hbar[2\pi M_s \sin^2\theta_q \exp(-2i\phi_q)]$$

where $b_q^\dagger$ and b_q are spin wave creation and annihilation operators, (Bose operators), H is the external field (including the static demagnetizing field), A is the exchange constant, γ is the gyromagnetic ratio, q the spin wave wave-vector, and θ_q and ϕ_q are the polar and azimuthal angles of the spin wave wave-vector, with respect to the direction of $\bar{M}_s$. The wave vector q should be written as a vector but will not be so written for typographical ease. Equation (5.4) may be obtained by writing the energy of the spin system including the exchange interaction, the dipole-dipole interaction and the interaction with the external field, and carrying out the first two

Holstein-Primakoff transformations (see Sparks[6]). The non-diagonal terms in the Hamiltonian, $B_m b_m b_{-m}$ and $B_m^* b_m^\dagger b_{-m}^\dagger$, may be removed by carrying out the third Holstein-Primakoff transformation, however it is simpler to work with the Hamiltonian of equation (5.4). The creation and annihilation operators obey the commutation relations:

$$[b_m, b_q^\dagger] = b_m b_q^\dagger - b_q^\dagger b_m = \delta_{mq} \tag{5.5}$$

$$[b_m, b_q] = 0 \qquad [b_m^\dagger, b_q^\dagger] = 0$$

The transverse components of the magnetization, m_x and m_y may be written in terms of the circular components m_+ and m_-:

$$m_+ = m_x + i m_y \tag{5.6}$$

$$m_- = m_x - i m_y$$

$$m_x = (1/2)(m_+ + m_-)$$

$$m_y = (1/2i)(m_+ - m_-)$$

In terms of the spin wave creation and annihilation operators these components are (see Turov[45]):

$$m_-(r) = \sqrt{2\gamma\hbar M_s/V}\ \Sigma \exp(i qr) b_q \tag{5.7}$$

$$m_+(r) = \sqrt{2\gamma\hbar M_s/V}\ \Sigma \exp(-i qr) b_q^\dagger$$

$$m_x(r) = (1/2)\sqrt{2\gamma\hbar M_s/V}\ \Sigma\exp(iqr)(b_q + b^\dagger_{-q})$$

$$m_y(r) = (1/2i)\sqrt{2\gamma\hbar M_s/V}\ \Sigma\exp(iqr)(b_q - b^\dagger_{-q})$$

where V is the volume of the system. Sparks relates m_+ to b_q and m_- to $b^\dagger_q$. If this convention is used the commutator (5.5) must have the opposite sign. This may be seen by comparing the commutation relations for the magnetic moment components with the relations for the angular momentum, $\bar{L}$, and recalling that $\bar{M} = -\gamma\bar{L}$, see Turov[45].

The electron Hamiltonian is simply:

$$H_{el} = \Sigma E_k c^\dagger_k c_k \tag{5.8}$$

where $c^\dagger_k$ and c_k are electron creation and annihilation operators, (Fermi operators), k the electron momentum and E_k the energy of an electron with momentum k. We need to consider electron states located about the three cube axes [100], [010] and [001]. To keep track of which states are under consideration we define three sets of operators: $c^\dagger_{1k}$, c_{1k} for the states along [100], $c^\dagger_{2k}$, c_{2k} for the states along [010], and $c^\dagger_{3k}$, c_{3k} for the states along [001]. In terms of these operators the electron Hamiltonian is:

$$H_{el} = \Sigma E_{1k}\ c^\dagger_{1k}\ c_{1k} + \Sigma E_{2k}\ c^\dagger_{2k}\ c_{2k} + \Sigma E_{3k}\ c^\dagger_{3k}\ c_{3k} \tag{5.9}$$

The electron operators anti-commute:

$$[\, c_m \,,\, c_l^\dagger \,]_+ = c_m\, c_l^\dagger + c_l^\dagger\, c_m = \delta_{ml} \qquad (5.10)$$

$$[\, c_m \,,\, c_l \,]_+ = 0 \qquad [\, c_m^\dagger \,,\, c_l^\dagger \,]_+ = 0$$

The energies E_{1k}, E_{2k} and E_{3k} are those of equation (5.3) evaluated in equilibrium ($m_x, m_y = 0$). They include the kinetic energy and a spin-orbit shift.

The interaction Hamiltonian describes the changes in energy which arise as the magnetization deviates from equilibrium.

Consider case (i), Figure 5.3(a). For the electron states about the [100] axis $\cos(\theta_M) \simeq m_x/M_s$ and the change in energy, ΔE_{100}, is $-(\xi/2M_s)m_x = -(1/2)(\xi/2M_s)(m_+ + m_-)$. For the states about the [010] axis $\cos(\theta_M) \simeq m_y/M_s$ and $\Delta E_{010} = -(\xi/2M_s)m_y$ $= -(1/2i)(\xi/2M_s)(m_+ - m_-)$. For the states about the [001] axis $\cos(\theta_M)$ does not change to first order in m_x and m_y. Let $\Delta E_+ = -(\xi/2M_s)m_+$ and $\Delta E_- = -(\xi/2M_s)m_-$. Transforming to second quantized notation:

$$\Delta E_+ = -(\xi/2M_s)m_+$$

$$= -(\xi/2M_s)\sqrt{2\gamma\hbar M_s/V}\ \Sigma\Sigma\Sigma\ \langle\phi_{k1}|\exp(iqr)b_q|\phi_{k2}\rangle\ c_{k1}^\dagger\ c_{k2}$$

$$= 2\mathcal{P}\Sigma\Sigma\Sigma c_{k+q}^\dagger c_k b_q \qquad (5.11a)$$

where $|\phi_{k1}> = (1/\sqrt{V})\exp(ik_1 r)$ is an electron wave function and $Þ = -(1/2)(\xi/2M_s)\sqrt{2\gamma\hbar M_s/V}$ (this symbol, Þ, is called 'thorn'). Similarly:

$$\Delta E_{-} = 2Þ\Sigma\Sigma c^{\dagger}_{k-q} c_k b^{\dagger}_q \qquad (5.11b)$$

Placing the axis labels on the electron operators:

$$\Delta E_{100} = Þ\Sigma\Sigma(c^{\dagger}_{1k+q}\, c_{1k}\, b_q + c^{\dagger}_{1k-q}\, c_{1k}\, b^{\dagger}_q) \qquad (5.11c)$$

$$\Delta E_{010} = -i Þ\Sigma\Sigma(c^{\dagger}_{2k+q}\, c_{2k}\, b_q - c^{\dagger}_{2k-q}\, c_{2k}\, b^{\dagger}_q)$$

$$\Delta E_{001} = 0$$

The interaction Hamiltonian is the sum $\Delta E_{100} + \Delta E_{010} + \Delta E_{001}$. In general, the component of the magnetization along the [100] axis, M_{100}, may be written:

$$M_{100} = \alpha M_x + \beta M_y + \gamma M_z$$

$$= (\alpha - i\beta) m_+ + (\alpha + i\beta) m_- + \gamma M_z$$

In equilibrium m_+ and m_- are zero so that $M_{100} = \gamma M_z$. The change in energy for the states on the pocket at [100] for a deviation of the magnetization from equilibrium is:

$$\Delta E_{100} = (1/2)(-\xi/2M_S)[(a-i\beta)m_+ + (a+i\beta)m_-]$$

since the change in M_z is second order in m_- and m_+. If we let $(a-i\beta) = A_+$ and $(a+i\beta) = A_-$, with similar definitions of B_+, B_- and C_+ and C_- for the pockets at [010] and [001] respectively, the interaction Hamiltonian may be written:

$$H_{int} = \hbar\Sigma\Sigma((A_+ c^\dagger_{1k+q} c_{1k} + B_+ c^\dagger_{2k+q} c_{2k} + C_+ c^\dagger_{3k+q} c_{3k})b_q +$$

$$(A_- c^\dagger_{1k-q} c_{1k} + B_- c^\dagger_{2k-q} c_{2k} + C_- c^\dagger_{3k-q} c_{3k})b^\dagger_q) \qquad (5.12)$$

with $A_+ = A^*_-$, $B_+ = B^*_-$ and $C_+ = C^*_-$. This Hamiltonian is in fact Hermitian. The constants A_+, B_+ and C_+ are listed in Table 5-2 for the five cases of interest.

TABLE 5-2

Case	Normal	M_S	A_+	B_+	C_+
(i)	[010]	[001]	1	$-i$	0
(ii)	[010]	[101]	$1/\sqrt{2}$	$-i$	$-1/\sqrt{2}$
(iii)	$[1\bar{1}0]$	[001]	$(1+i)/\sqrt{2}$	$(1-i)/\sqrt{2}$	0
(iv)	$[1\bar{1}0]$	[111]	$(1+\sqrt{3}i)/\sqrt{6}$	$(1-\sqrt{3}i)/\sqrt{6}$	$-2/\sqrt{6}$
(v)	$[1\bar{1}0]$	[110]	$i/\sqrt{2}$	$-i/\sqrt{2}$	-1

The total Hamiltonian is $H = H_{sw} + H_{el} + H_{int}$.

5.3 Calculation of the Damping

Green's Functions

Green's functions and their applications to physical problems have been discussed in detail by Zubarev[80]. The reader is referred to that paper for elaboration of the statements made in this section. For our purposes the Green's function for two (time dependent) operators A and B is:

$$G(t) = (-i/\hbar)\theta(t)\mathrm{Tr}(\rho_0[A(t),B(0)]) = \langle\langle A;B\rangle\rangle \qquad (5.13)$$

where the square brackets represent a commutator, ρ_0 is the density matrix for the system under consideration when in thermal equilibrium, the trace represents a thermal average and $\theta(t)$ is the step function, $\theta(t) = 1$ if $t > 0$, $\theta(t) = 0$ if $t < 0$. It can be demonstrated that the Green's function is the response of the operator A to a perturbation $B\delta(t)$. The response to a perturbation of the form $B\exp(-i\omega t)$ is described by the susceptibility $\chi(\omega)$:

$$\chi(\omega) = \langle A(t)\rangle/B\exp(-i\omega t) = 2\pi G(\omega) \qquad (5.14)$$

where $G(\omega)$ is the Fourier Transform of $G(t)$:

$$G(\omega) = (1/2\pi)\int_0^\infty dt\ \exp(i\omega t)G(t) \qquad (5.15)$$

$$= (1/2\pi)\int_{-\infty}^\infty dt\ \exp(i\omega t)G(t)$$

since G is zero for $t \leq 0$.

To evaluate the Green's function we differentiate equation (5.13) with respect to time. The time derivative of the operator A is the commutator of A with the Hamiltonian of the system:

$$i\hbar dA/dt = [A,H] \qquad (5.16)$$

The result of this differentiation will be new Green's functions. These may be differentiated in turn until the original Green's function is obtained, in which case the system of equations resulting from differentiation may be solved exactly, or until Green's functions are obtained which may be related to the original function by an approximation.

The Calculation

In the calculation which follows we wish to determine the response of the magnetization to a transverse driving field:

$$\bar{h}(\bar{r},t) = h_x \exp(i(qy-\omega t))$$

The perturbation is then:

$$H_1 = -\int \bar{m}(\bar{r}) \cdot \bar{h}(\bar{r}) dV$$
$$= -\int m_x(\bar{r}) h_x \exp(i qy) dV$$

Writing m_x in terms of spin wave creation and annihilation operators (5.7):

$$H_1 = -(1/2)\sqrt{2\gamma\hbar M_s/V}\ \Sigma(b_m + b_{-m}^\dagger) h_x \int \exp(i mr)\exp(i qy) dV$$
$$= -(1/2)\sqrt{2\gamma\hbar M_s V}(b_{-q} + b_q^\dagger) h_x \qquad (5.17)$$

These operators enter the Green's functions as the operator B. The operator A is that representing the component of the magnetization of interest, m_x or m_y, or m_+ or m_-. For example:

$$m_- = -(1/2)(\sqrt{2\gamma\hbar M_s/V})(\sqrt{2\gamma\hbar M_s V})\ \Sigma\langle\langle b_m ; b_{-q} + b_q^\dagger \rangle\rangle \exp(i mr) h_x \qquad (5.18)$$

Because there is no coupling between spin waves in this model, only the following Green's functions will be non-zero:

$$G_1 = \langle\langle b_q ; b_q^\dagger \rangle\rangle \qquad (5.19)$$

$$G_2 = \langle\langle b_q ; b_{-q} \rangle\rangle$$

$$G_3 = \langle\langle b_{-q}^\dagger ; b_{-q} \rangle\rangle$$

$$G_4 = \langle\langle b^\dagger_{-q}; b^\dagger_q \rangle\rangle$$

Then:

$$m_-/h_x = -\gamma\hbar M_s \langle\langle b_q; b_{-q} + b^\dagger_q \rangle\rangle = -\gamma\hbar M_s (G_1 + G_2) \tag{5.20}$$

$$m_+/h_x = -\gamma\hbar M_s (G_3 + G_4)$$

$$m_x/h_x = -\gamma\hbar M_s/2 (G_1 + G_2 + G_3 + G_4)$$

$$m_y/h_x = i\gamma\hbar M_s/2 (G_1 + G_2 - G_3 - G_4)$$

The steps in the calculation will be indicated for the Green's function G_1, the procedure being the same for the three other functions.

Taking the time derivative of G_1 and multiplying by $i\hbar$:

$$i\hbar dG_1/dt = \delta(t)\langle [b_q, b^\dagger_q] \rangle - i(\theta(t)/\hbar)\langle [i\hbar db_q/dt, b^\dagger_q] \rangle$$

$$= \delta(t) - i(\theta(t)/\hbar)\langle [[b_q, H], b^\dagger_q] \rangle \tag{5.21}$$

The commutator of b_q with H is:

$$[b_q, H] = A_q b_q + B^*_q b^\dagger_{-q}$$

$$+ \text{Þ}\Sigma (A_- c^\dagger_{1k-q} c_{1k} + B_- c^\dagger_{2k-q} c_{2k} + C_- c^\dagger_{3k-q} c_{3k}) \tag{5.22}$$

so that:

$$i\hbar dG_1/dt = \delta(t) + A_q G_1 + B_q^* G_4 +$$

$$\text{Þ}\Sigma(A\_F_{11}(k) + B\_F_{12}(k) + C\_F_{13}(k)) \qquad (5.23)$$

where $F_{11}(k)$, $F_{12}(k)$ and $F_{13}(k)$ are new Green's functions which contain both electron and spin wave operators:

$$F_{11}(k) = \langle\langle c^\dagger_{1k-q}\, c_{1k} \,; b^\dagger_q \rangle\rangle. \qquad (5.24)$$

F_{12} and F_{13} are defined in a similar manner. The first subscript indicates which of the original Green's functions the new Green's function is derived from. The second subscript represents the pocket with which the electron operators are associated.

Taking the time derivative of $F_{11}(k)$ and multiplying by $i\hbar$ (and not writing down the intervening steps):

$$i\hbar dF_{11}/dt = (E_{1k} - E_{1k-q})F_{11} + \text{Þ}\Sigma(A\_\langle\langle c^\dagger_{1k-q}\, c_{1k-m}\, b_m ; b^\dagger_q \rangle\rangle$$

$$- A\_\langle\langle c^\dagger_{1k-q+m}\, c_{1k}\, b_m ; b^\dagger_q \rangle\rangle + A_+\langle\langle c^\dagger_{1k-q}\, c_{1k+m}\, b^\dagger_m ; b^\dagger_q \rangle\rangle$$

$$- A_+\langle\langle c^\dagger_{1k-q-m}\, c_{1k}\, b^\dagger_m ; b^\dagger_q \rangle\rangle \qquad (5.25)$$

Again we have new Green's functions. These may be related to the original Green's functions by an approximation (the random phase approximation). For example:

$$<< c^{\dagger}_{1k-q}\, c_{1k-m}\, b_m ; b^{\dagger}_q >> \simeq < c^{\dagger}_{1k-q}\, c_{1k-m} > << b_m ; b^{\dagger}_q >> \qquad (5.26)$$

where $< c^{\dagger}_{1k-q}\, c_{1k-m} >$ is the expectation value of the operator $c^{\dagger}_{1k-q}\, c_{1k-m}$. This will be zero unless $m = q$ and $< c^{\dagger}_{1k-q}\, c_{1k-q} > = n_{1k-q}$, the occupation number of the state $(k-q)$ in thermal equilibrium. The assumption is made that the electron spin wave interaction does not disturb the electron distribution. The Green's functions $<< c^{\dagger}_{1k-q}\, c_{1k-m}\, b_m ; b^{\dagger}_q >>$ reduce to the single Green's function $n_{1k-q} << b_q ; b^{\dagger}_q >> = n_{1k-q} G_1$. We have recovered the original Green's functions. Performing the same contraction on the three other sets of Green's functions in equation (5.15) leaves:

$$i\hbar dF_{11}/dt = (E_{1k} - E_{1k-q})F_{11} + Þ(n_{1k-q} - n_{1k})(A_+ G_1 + A_- G_4) \qquad (5.27)$$

Changing to the Fourier components of these Green's functions (equation (5.15)) we can write the equations for the Green's functions in a form which does not contain time derivatives, ($i\hbar dF/dt$ becomes $\hbar\omega F$). We find:

$$F_{11}(k) = Þ[(n_{1k-q} - n_{1k})/(\hbar\omega - (E_{1k} - E_{1k-q}))]\ (A_+ G_1 + A_- G_4) \qquad (5.28)$$

using the same notation for the Green's functions and their Fourier components. Substituting this expression and the equivalent expressions for $F_{12}(k)$ and $F_{13}(k)$ into the Fourier transformed equation for G_1 yields:

$$[\hbar\omega - A_q - (A_+A_-\Gamma_1 + B_+B_-\Gamma_2 + C_+C_-\Gamma_3)]G_1 - [B_q^* + (A_-^2\Gamma_1 + B_-^2\Gamma_2 + C_-^2\Gamma_3)]G_4 = 1 \tag{5.29}$$

where:

$$\Gamma_1 = \text{Þ}^2\Sigma(n_{1k-q} - n_{1k})/(\hbar\omega - (E_{1k} - E_{1k-q})) \tag{5.30}$$

Γ_2 AND Γ_3 are defined similarly for the pockets at [010] and [001]. Performing the same operations (equations 5.21 through 5.29) with G_4 yields:

$$[B_q + (A_+^2\Gamma_1 + B_+^2\Gamma_2 + C_+^2\Gamma_3)]G_1 + [\hbar\omega + A_q + (A_+A_-\Gamma_1 + B_+B_-\Gamma_2 + C_+C_-\Gamma_3)]G_4 = 0 \tag{5.31}$$

where the fact that $A_{-q} = A_q$, and $B_{-q} = B_q$ has been used. Define:

$$\beta_1 = A_+A_-\Gamma_1 + B_+B_-\Gamma_2 + C_+C_-\Gamma_3 \tag{5.32}$$

$$\beta_2 = A_+^2\Gamma_1 + B_+^2\Gamma_2 + C_+^2\Gamma_3$$

$$\beta_3 = A_-^2\Gamma_1 + B_-^2\Gamma_2 + C_-^2\Gamma_3$$

Solving for G_1 and G_4:

$$G_1 = \langle\langle b_q ; b_q^\dagger \rangle\rangle = (\hbar\omega + (A_q + \beta_1))/D \tag{5.33}$$

$$G_4 = \langle\langle b_{-q}^\dagger ; b_q^\dagger \rangle\rangle = -(B_q + \beta_2)/D$$

$$D = (\hbar\omega - (A_q + \beta_1))(\hbar\omega + (A_q + \beta_1)) + (B_q + \beta_2)(B_q^* + \beta_3)$$

Performing the calculation for G_2 and G_3:

$$G_2 = \langle\langle b_q ; b_{-q} \rangle\rangle = -(B_q^* + \beta_3)/D \tag{5.34}$$

$$G_3 = \langle\langle b_{-q}^\dagger ; b_{-q} \rangle\rangle = -(\hbar\omega - (A_q + \beta_1))/D$$

The denominator, D, is the same for all four Green's functions. For our case $\theta_q = \pi/2$, $\phi_q = \pi/2$, so, from equation (5.4):

$$A_q = \gamma\hbar(H + 2\pi M_s + 2Aq^2/M_s)$$

$$B_q = -\gamma\hbar 2\pi M_s = B_q^*$$

In the absence of spin-orbit coupling β_1, β_2, β_3 are zero. The denominator D and the ratios m_x/h_x and m_y/h_x become:

$$D = (\gamma\hbar)^2[(\omega/\gamma)^2 - (H + 2Aq^2/M_s)(H + 4\pi M_s + 2Aq^2/M_s)]$$

$$m_x/h_x = -(\gamma\hbar)^2 M_s (H + 4\pi M_s + 2Aq^2/M_s)/D \tag{5.35}$$

$$m_y/h_x = -(\gamma\hbar)^2 M_s i(\omega/\gamma)/D$$

These expressions are the same as equations (2.18) (the denominator of (2.18) is rewritten below) in the absence of MCA and damping (note the difference in the coordinate system of equation (2.18)). If $\beta_2 = \beta_3$ the denominator may be factored

as:

$$D = (\gamma\hbar)^2((\omega/\gamma)^2 - [H + 2Aq^2/M_s + (\beta_1 + \beta_2)/\gamma\hbar]$$

$$[H + 4\pi M_s + 2Aq^2/M_s + (\beta_1 - \beta_2)/\gamma\hbar]) \qquad (5.36)$$

Such factoring will be possible if $A_+^2 = A_-^2$, $B_+^2 = B_-^2$ and $C_+^2 = C_-^2$, which is true if the sample plane is a (100) plane, see Table 5-2. If the sample plane is a (110) plane the coefficients A_+, A_-, B_+ and B_- are related by $A_+ = B_-$ and $A_- = B_+$. In this situation β_2 will equal β_3 if $\Gamma_1 = \Gamma_2$, that is if the sums for the pockets at [100] and [010] are the same. Due to the symmetry of the situation this will be true (see Figure 5.3(a)) so that for all cases of interest $\beta_2 = \beta_3$. The denominator of equation (2.18) is:

$$D=[H+\alpha+2Aq^2/M_s-i(\omega/\gamma)(G/\gamma M_s)][B+\gamma+2Aq^2/M_s-i(\omega/\gamma)(G/\gamma M_s)]-(\omega/\gamma)^2 \qquad (5.37)$$

where α and γ are effective magnetocrystalline anisotropy (MCA) fields (this γ should not be confused with the gyromagnetic ratio) and G is the Gilbert damping parameter (not to be confused with the Green's functions G). Comparing the two expressions (2.18) and (5.36) suggests identifying the real part of $(\beta_1 \pm \beta_2)/\gamma\hbar$ with an effective MCA field (possibly wavenumber dependent) and the imaginary part with $i(\omega/\gamma)(G/\gamma M_s)$:

$$\alpha = \mathrm{Rl}(\beta_1 + \beta_2)/\gamma\hbar \qquad (5.38)$$

$$\gamma = \mathrm{Rl}(\beta_1 - \beta_2)/\gamma\hbar$$

$$G_1 = -(\gamma M_s/\hbar\omega)\mathrm{Im}(\beta_1 + \beta_2)$$

$$G_2 = -(\gamma M_s/\hbar\omega)\mathrm{Im}(\beta_1 - \beta_2)$$

An interesting result of this calculation is the possibility of the damping depending on the direction of the excursion of M_s from equilibrium, G_1 being the damping parameter for in-plane excursions and G_2 being the damping parameter for out of plane excursions. Writing the expressions for these damping parameters out in full:

$$G_1 = \frac{-\gamma^2\xi^2}{8\omega V}\mathrm{Im}\Big[(|A_+|^2 + A_+^2)\Sigma \frac{n_{1k-q}-n_{1k}}{\hbar\omega-(E_{1k-q}-E_{1k})} + (|B_+|^2 + B_+^2)\Sigma \frac{n_{2k-q}-n_{2k}}{\hbar\omega-(E_{2k-q}-E_{2k})} + (|C_+|^2 + C_+^2)\Sigma \frac{n_{3k-q}-n_{3k}}{\hbar\omega-(E_{3k-q}-E_{3k})}\Big] \qquad (5.39)$$

$$G_2 = \frac{-\gamma^2\xi^2}{8\omega V}\mathrm{Im}\Big[(|A_+|^2 - A_+^2)\Sigma \frac{n_{1k-q}-n_{1k}}{\hbar\omega-(E_{1k-q}-E_{1k})} + (|B_+|^2 - B_+^2)\Sigma \frac{n_{2k-q}-n_{2k}}{\hbar\omega-(E_{2k-q}-E_{2k})} + (|C_+|^2 - C_+^2)\Sigma \frac{n_{3k-q}-n_{3k}}{\hbar\omega-(E_{3k-q}-E_{3k})}\Big]$$

Evaluation of the Damping Parameters

To obtain values for these damping parameters we have to evaluate a sum of the form:

$$S = (1/V)\Sigma(n_{k-q} - n_k)/(\hbar\omega - (E_k - E_{k-q}))$$

for each of the three pockets. The sum is converted to an integral:

$$S = \int d^3k/(2\pi)^3 \, [(n(k-q) - n(k))/(\hbar\omega-(E(k)-E(k-q)))] \qquad (5.40)$$

where n(k) is the Fermi distribution function and E(k) is the energy of an electron in state k. Since k is of the order of k_F ($\simeq 10^8$ cm^{-1}) and q is of the order of $1/\delta$ ($\simeq 10^5$ cm^{-1}), we may expand n(k-q) and E(k-q) about k:

$$n(k-q) \simeq n(k) - (\partial n/\partial k)\cdot q = n(k) - (\partial n/\partial E)(\partial E/\partial k)\cdot q$$

$$= n(k) + \delta(E(k) - E_F)\hbar q\cdot v(k)$$

where $(\partial n/\partial E) = -\delta(E(k) - E_F)$ assuming the Fermi distribution is a step function, and $\partial E/\partial k = \hbar v(k)$. Expanding E(k-q):

$$E(k-q) \simeq E(k) - (\partial E/\partial k)\cdot q$$
$$= E(k) - \hbar q\cdot v(k)$$

The integral (5.40) becomes:

$$S = \int \frac{d^3k}{(2\pi)^3} \frac{\delta(E(k)-E_F)\ \hbar q\cdot v}{\hbar\omega - \hbar q\cdot v} \qquad (5.41)$$

Following Heinrich, Fraitova and Kambersky[75] the finite lifetime of the excited electron states is taken into account by adding a small imaginary part, $-i\hbar/\tau$, to the energy, where τ is the average time between collisions of an electron with a phonon or an impurity. This term must be included on the top of the integrand (in the Δn term) as well as the bottom (in the ΔE term) so that:

$$S = \int \frac{d^3k}{(2\pi)^3} \frac{\delta(E(k)-E_F)\ (q\cdot v - i/\tau)}{\omega - q\cdot v + i/\tau}$$

or, writing this in terms of real and imaginary parts:

$$S = \int \frac{d^3k}{(2\pi)^3} \frac{-[1+q\cdot v\tau(q\cdot v\tau-\omega\tau)]-i\omega\tau}{1+(q\cdot v\tau-\omega\tau)^2} \qquad (5.42)$$

For a spherical Fermi surface this integral may be evaluated analytically, the imaginary part of the integral being:

$$Im(S) = -(k_F^2/(2\pi)^2\hbar v_F)(\omega\tau/ql)\ [\arctan(ql+\omega\tau) + \arctan(ql-\omega\tau)] \qquad (5.43)$$

where v_F is the Fermi velocity and l is the electron mean free path, $l = v_F\tau$. If ql and $\omega\tau$ are both small compared to 1 $\arctan(ql \pm \omega\tau) \simeq (ql \pm \omega\tau)$ and the sum varies directly with the relaxation time τ:

$$Im(S) = [2k_F^2/(2\pi)^2\hbar v_F](\omega\tau) \tag{5.44}$$

If $\omega\tau << 1$ and $ql \simeq 1$, $\arctan(ql + \omega\tau) \simeq \arctan(ql)$ and:

$$Im(S) = [2k_F^2/(2\pi)^2\hbar v_F](\omega\tau/ql)\ \arctan(ql) \tag{5.45}$$

When multiplied by the appropriate constants (see equation 5.39) this is the result of Korenman and Prange[3,4]. It is the form of the wavenumber dependent part of the damping used in Chapter 4 for comparison with experiment.

For a non-spherical Fermi surface, such as our pockets, the integral must be evaluated numerically. The integral may be evaluated in a coordinate system in which the z-axis is parallel to the Γ-X axis of the pocket under consideration. This coordinate system is different for each pocket. The direction of q must be considered for each pocket and each case, see Table 5-2. The energy E(k) in such a coordinate system is (equation 5.3):

$$E(k) = E_x - (\xi/2)\cos(\theta_M) - \hbar^2/2(k_x^2/m_1^* + k_y^2/m_1^* + k_z^2/m_2^*)$$

where E_X is the energy of the X_5 level at the X-point in the absence of spin-orbit coupling and θ_M is the angle between the equilibrium direction of the magnetization and the Γ-X axis. The Fermi surface is given by $E(k) = E_F$ or:

$$k_F^2(\theta,\phi) = \frac{E_X - E_F - (\xi/2)\cos\theta_M}{(\hbar^2/2m_1^*)(\sin^2\theta + (m_1^*/m_2^*)\cos^2\theta)} \tag{5.46}$$

The Fermi velocity is given by $\hbar v_F = |\nabla_k E(k)|$:

$$v_F(k_F,\theta,\phi) = (\hbar k_F(\theta,\phi)/m_1^*)\sqrt{\sin^2\theta + (m_1^*/m_2^*)^2\cos^2\theta} \tag{5.47}$$

The volume element d^3k may be written:

$$d^3k = dS_k dk = k^2(\theta,\phi)\ \sin(\theta)d\theta d\phi dE/\hbar v(\theta,\phi) \tag{5.48}$$

where dS_k is an element of area on a surface of constant energy and dk is an element of length perpendicular to that surface. Carrying out the integration over the energy the integral becomes:

$$S = -\int_0^{\pi} d\theta \int_0^{2\pi} d\phi \frac{k_F^2}{(2\pi)^3 \hbar v_F} \frac{1 + q\cdot v\tau(q\cdot v\tau - \omega\tau) + i\omega\tau}{1 + (q\cdot v\tau - \omega\tau)^2} \tag{5.49}$$

The dot product $q\cdot v_F$ is different for each of the pockets because we use a coordinate system in which k_z is along the Γ-X

axis of the pocket of interest.

5.4 Results

The summations of equation (5.39) have been carried out for the three orientations of the magnetization in the (110) plane. These correspond to the configurations investigated in this thesis. Values of τ of 10^{-14}, 10^{-13}, and 10^{-12} sec, corresponding to room temperature, 77 K, and a resistivity ratio of 100 were used. The parameters for Nickel listed in Table 4-1 and the parameters of HSG for the hole pockets, Table 5-1, were used. A useful conversion factor is 1 Oe^2 = 1.5687×10^{13} eV/cm^3. The sums were evaluated for q varying from 0 to 10^6 cm^{-1} which includes the q-vectors of interest at the three temperatures (see the numbers quoted in Table 2-3).

The absolute value of the effective MCA field which arises from the real part of the integrals is shown on Figure 5.4 for the magnetization along [001] for the three values of τ. The two MCA fields, α and γ, are the same for this orientation $\alpha = \gamma = (\xi^2/8M_s)\mathrm{Rl}(S_{100}+S_{010})$ where S_{100} and S_{010} represent the integrals for the pockets at [100] and [010] respectively. Since these two pockets are equivalent:

$$\alpha = \gamma = (\xi^2/8M_s)2\mathrm{Rl}(S_{100})$$

The calculated fields for $\tau = 10^{-14}$ sec and $\tau = 10^{-13}$ sec were

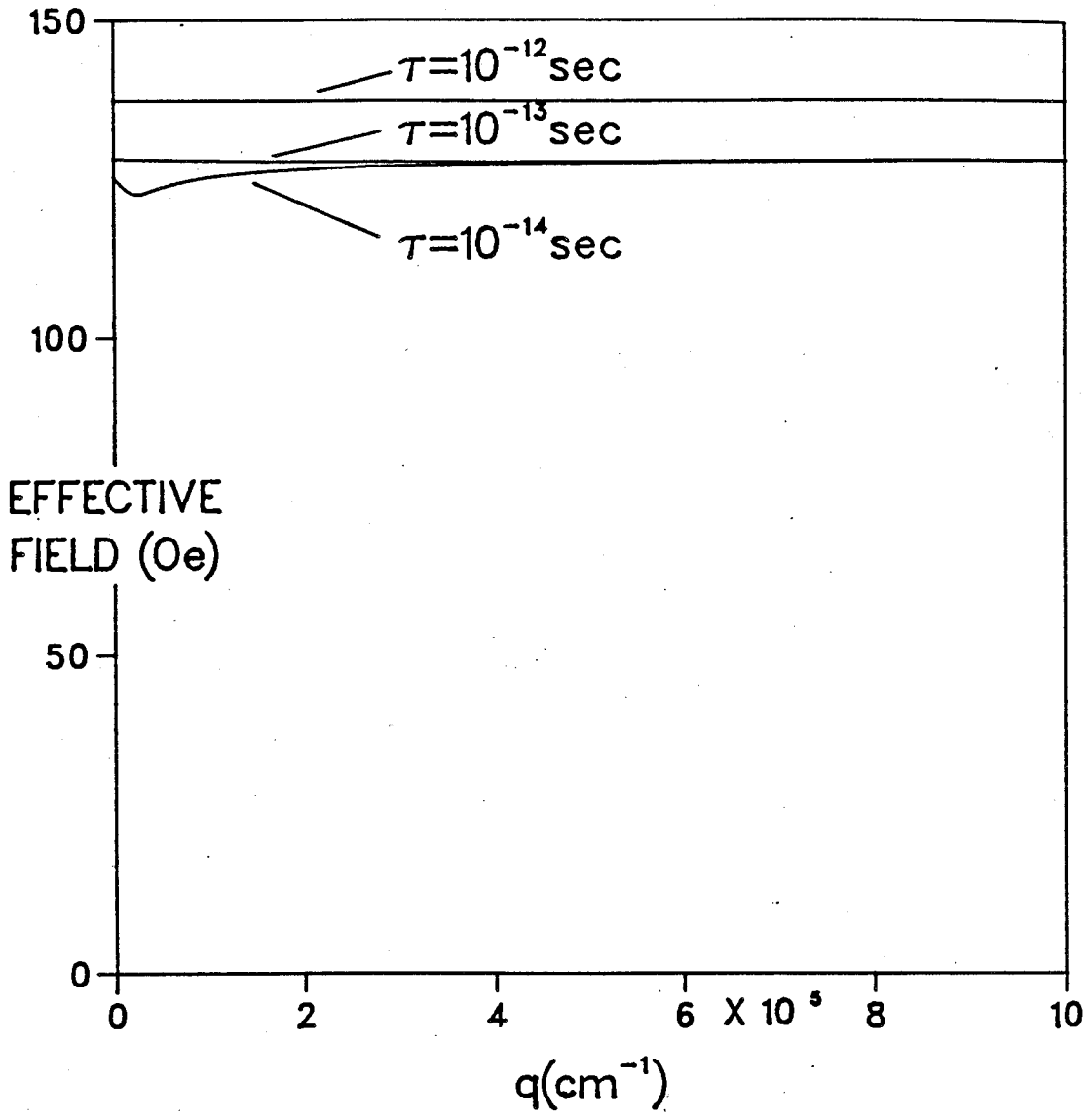

Figure 5.4 The effective MCA field due to the real part of the pocket integrals, as a function of wavenumber q, for three values of the electron relaxation time τ. For the calculation the magnetization was assumed to be parallel to the [001] axis.

found to be independent of q with magnitudes 137 and 128 Oe respectively. This difference is due to the change in the saturation magnetization, since the values of M_s were chosen to correspond to 300 K and 77 K respectively, not to the variation with τ of the integral. There is a small q-dependence at $\tau = 10^{-12}$ sec near q = 0 where $qv\tau \simeq \omega\tau$. The fields are negative which leads to a shift of FMR to higher field values. The fields for the magnetization along [110] and [111] have similar q-dependences and magnitudes. The fields are negative for all three orientations of the magnetization.

The expressions for the two damping parameters, G_1 and G_2, for the three orientations of the magnetization in the $[1\bar{1}0]$ plane are listed in Table 5-3.

TABLE 5-3

M_s	G_1	G_2
[001]	$-(\gamma^2\xi^2/4\omega)\mathrm{Im}(S_{100})$	$-(\gamma^2\xi^2/4\omega)\mathrm{Im}(S_{100})$
[111]	$-(\gamma^2\xi^2/12\omega)[\mathrm{Im}(S_{100})+2\mathrm{Im}(S_{001})]$	$-(\gamma^2\xi^2/4\omega)\mathrm{Im}(S_{100})$
[110]	$-(\gamma^2\xi^2/4\omega)\mathrm{Im}(S_{001})$	$-(\gamma^2\xi^2/4\omega)\mathrm{Im}(S_{100})$

Recall that G_1 is the damping parameter for in-plane excursions of the magnetization from equilibrium while G_2 is the damping parameter for out-of-plane excursions. Note that the damping parameter G_2 is the same for the three orientations of the magnetization and that with the magnetization along [001] $G_1 = G_2$. If the three pockets are equivalent ($S_{100} = S_{010} = S_{001}$) then $G_1 = G_2$ and the damping for the three orientations is the same. Values of G_1 and G_2 for the three temperatures at

q = 0 are listed in Table 5-4 with the values of the wavenumber independent Gilbert damping parameter required by experiment, see Chapter 4. Plots of G_1 and G_2 versus q for the three temperatures and three orientations are shown in Figures 5.5 (M_S along [001]), and 5.7(a) (M_S along [111]) and 5.7(b) (M_S along [110]). Also plotted on Figure 5.5 is G(0) arctan(ql)/ql for $\tau = 10^{-12}$, the form of the wavenumber dependent part of the damping assumed in Chapter 4. The mean free path $l = 4\times10^{-5}$ cm was chosen to match the calculated variation of the damping parameter as closely as possible. It may be compared with the value $l = 5.0\times10^{-5}$ cm determined using $v_F = \hbar k_{XW}/m_1^*$. listed in Table 5-1.

TABLE 5-4

	(001)		(111)		(110)		Expt
τ	G_1	G_2	G_1	G_2	G_1	G_2	G
(sec)		(10^8 sec^{-1})					
10^{-14}	0.0055	0.0055	0.0052	0.0052	0.0051	0.0055	2.45
10^{-13}	0.055	0.055	0.052	0.052	0.051	0.055	7.8
10^{-12}	0.53	0.53	0.51	0.51	0.50	0.53	14

It appears that Kambersky is the only one to have attempted calculation of the damping parameter from the known band structure of Nickel. The numbers quoted in [72] supersede the earlier estimates in [2] and [71]. Kambersky's calculations were carried out for both Nickel and Iron ignoring the shifts in

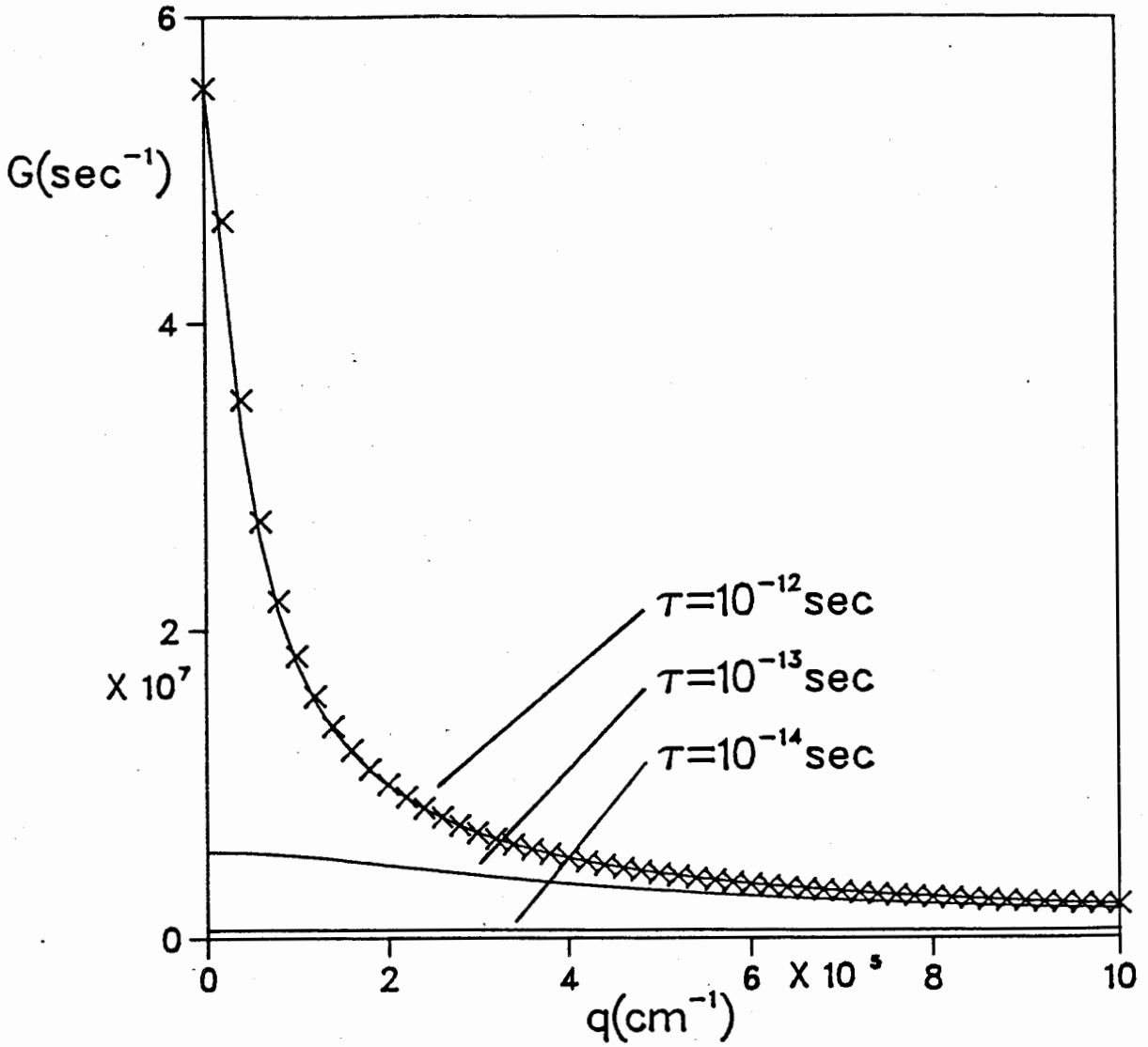

Figure 5.5 The variation of the damping parameter with wavenumber q for three values of the electron relaxation time τ. The magnetization points along [001]. $G_1 = G_2$ for this case. The crosses are a plot of $G(0)\arctan(ql)/ql$ where $l = 4\times10^{-5}$ cm is an electron mean free path at $\tau = 10^{-12}$ sec.

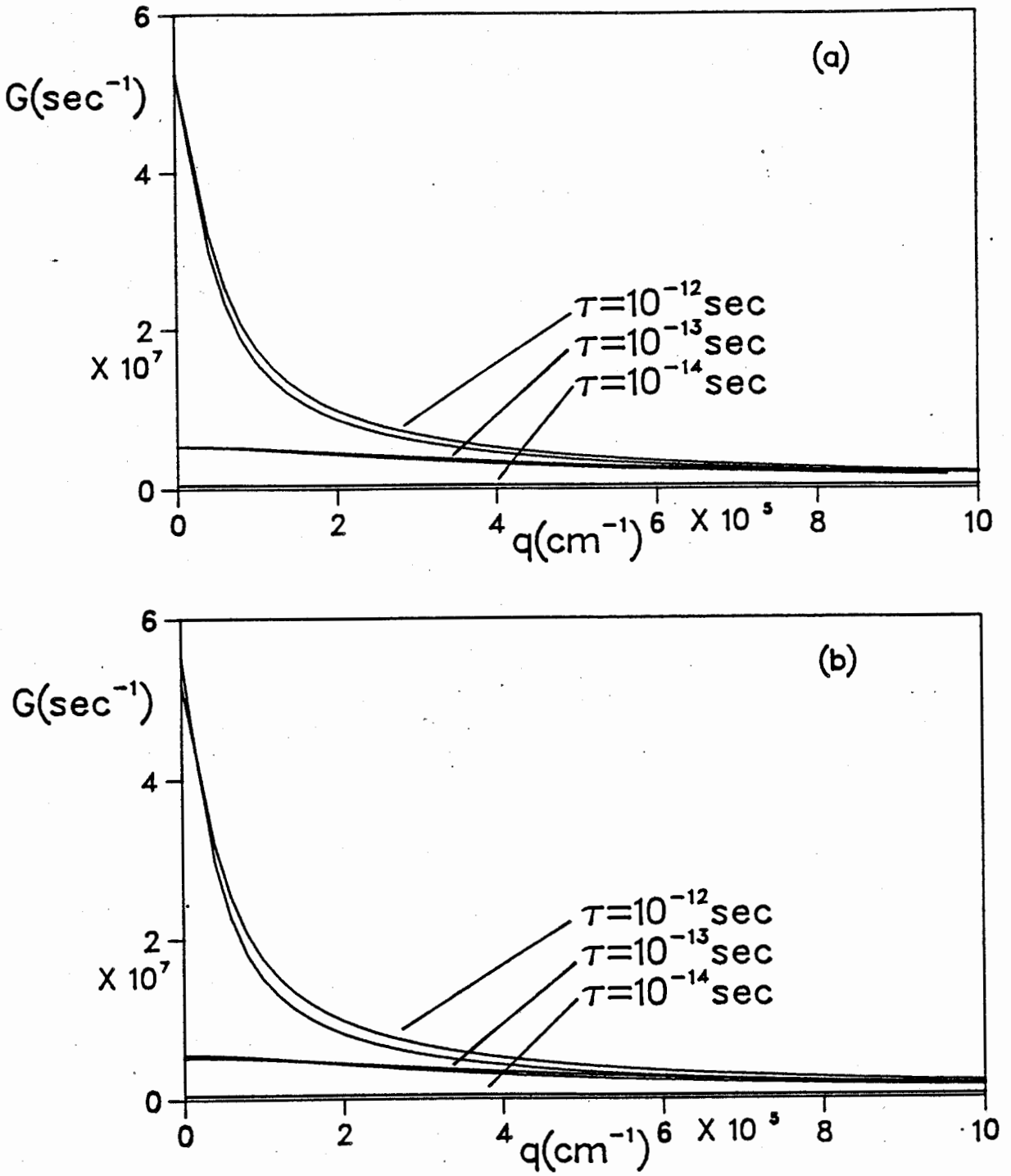

Figure 5.6 The variation of the damping parameters G_1 and G_2 with wavenumber q for three values of the electron relaxation time τ. (a) The magnetization points along [111]. (b) The magnetization points along [110].

energy levels due to spin-orbit coupling. Calculations were also made for the states around Γ-X including the energy shifts. These results are quoted in his Table IV which is reproduced here:

τ (10^{-13} sec)	0.13	0.32	0.80
G (10^{8} sec^{-1})	0.10	0.16	0.35

G is the Gilbert damping parameter for Nickel when M_s points along a (111) direction, and for q = 0. These numbers may be compared with those in Table 5-4.

The damping assumed in Chapter 4 for comparison with experiment was

$$G(q,T) = a(\sigma_0(T)/\sigma_0(295))\arctan(ql_D)/ql_D + b\rho(T)/\rho(295) \qquad (4.3)$$

where σ_0 was the dc conductivity, ρ the resistivity and l_D the d-electron mean free path. The values of a and b required to fit the FMAR data of Cochran and Heinrich[37] were $a = 1.07\times10^{8}$ sec^{-1} and $b = 1.19\times10^{8}$ sec^{-1}. With a resistivity ratio of 100 ($\tau\simeq10^{-12}$) the spin-flip damping, b, is negligible and the damping would be:

$$G(q) = 1.07\times10^{10} \arctan(ql_D)/ql_D$$

When this expression is evaluated for q approaching zero the resulting value for G is some 200 times the values listed in Table 5-4.

The predicted anisotropy of the linewidth is not in agreement with experiment. For example, using $G_1(q=0)$ and $G_2(q=0)$ for our comparison, it would be expected that ΔH_{100} should be larger than ΔH_{111} by approximately 4%. Since G_1 is not equal to G_2 for M_s along (111) the predicted anisotropy would have to be determined by carrying out a calculation of the absorption which included the two damping parameters G_1 and G_2. This has not been done, however it is unlikely that the anisotropy in the linewidth would exceed 4%. In any event the anisotropy is opposite to that observed experimentally, since ΔH_{111} was found to be greater than ΔH_{100} by approximately 12%.

The damping due to the X_5 hole pockets calculated using this simple model of interacting electrons and spin waves is unable to account for the magnitude or the anisotropy of the damping observed in experiment. We conclude that other portions of the Fermi surface must play a more important role in the magnetic damping in Nickel at low temperatures than has been hitherto recognized.

BIBLIOGRAPHY

[1] S.M. Bhagat and L.L. Hirst, Phys. Rev. 151, 401(1966)

[2] V. Kambersky, Can. J. Phys. 48, 2906,(1970)

[3] V. Korenman and R.E. Prange, Phys. Rev. B 6, 2769(1972)

[4] R.E. Prange and V. Korenman, J. Mag. Res. 6, 274(1972)

[5] S. Vonsovskii(ed.), Ferromagnetic Resonance, Pergamon Press, London, 1965

[6] M. Sparks, Ferromagnetic-Relaxation Theory, McGraw-Hill, New York, 1964

[7] W.S. Ament and G.T. Rado, Phys. Rev. 97, 1558(1955)

[8] A.B. Pippard, The Dynamics of Conduction Electrons, Gordon and Breach, New York, 1965

[9] L.L. Hirst and R.E. Prange, Phys. Rev. 139, A892(1965)

[10] R.J. Elliott, Phys. Rev. 96, 266(1954)

[11] E.I. Kondorsky, IEEE Trans. Mag. 10, 132(1974)

[12] S.M. Bhagat and P. Lubitz, Phys. Rev. B10, 179(1974)

[13] S.M. Bhagat and P. Lubitz, Technical Report No. 74-105(1974) University of Maryland(unpub.)

[14] J.N. Lloyd and S.M. Bhagat, Sol. State Comm. 8, 2029(1970)

[15] B. Heinrich, D.J. Meredith and J.F. Cochran, J. Appl. Phys. 50, 7726(1979)

[16] L. Hodges, D.R. Stone and A.V. Gold, Phys. Rev. Lett. 19, 655(1967)

[17] W. Anders, D. Bastian and E. Biller, Z. angew. Phys. 32, 12(1971)

[18] G.T. Rado, Ferromagnetic Resonance at Microwave Frequencies, in Advances in Electronics, Vol. 2, Academic Press, New York, 1950

[19] J.H.E. Griffiths, Nature 158, 670(1946)

[20] K.H. Reich, Phys. Rev. 101, 1647(1956)

[21] C.J. Tung, I. Said and G.E. Everett,
J. Appl. Phys. 53, 2044(1982)

[22] J.J.M. Franse, J. de Phys. 32, C1-186(1971)

[23] D.S. Rodbell, Phys. Rev. Lett. 13, 471(1964)

[24] D.S. Rodbell, Physics 1, 279(1965)

[25] G. Aubert, J. Appl. Phys. 39, 504(1968)

[26] Z. Frait and H. MacFaden, Phys. Rev. 139, A1173(1965)

[27] S.M. Bhagat, L.L. Hirst and J.R. Anderson,
J. Appl. Phys. 37, 194(1966)

[28] J.J.M. Franse, On the Magnetic Anisotropy Energy and the
Magnetostriction of Nickel and Iron
Ph.D. thesis, Amsterdam, 1969

[29] C. Vittoria, R.C. Barker and A. Yelon,
Phys. Rev. Lett. 19, 792(1967)

[30] J.R. Anderson, S.M. Bhagat and F.L. Cheng,
Phys. Stat. Sol.(b) 45, 357(1971)

[31] A.Z. Maksymowicz and K.D. Leaver,
J. Phys. F: Metal Phys. 3, 1031(1973)

[32] G.C. Bailey and C. Vittoria,
AIP Conf. Proc. No. 10, 130(1972)

[33] C.Y. Wu, H.T. Quach and A. Yelon,
AIP Conf. Proc. 29, 681(1975)

[34] C. Vittoria, R.C. Barker and A. Yelon,
J. Appl. Phys. 40, 1561(1969)

[35] C. Vittoria, G.C. Bailey, R.C. Barker and A. Yelon,
Phys. Rev. B7, 2112(1973)

[36] S.M. Bhagat, J.R. Anderson and Ning Wu,
Phys. Rev. 155, 510(1967)

[37] J.F. Cochran and B. Heinrich,
IEEE Trans. Mag. 16, 660,(1980)

[38] G. Dewar, B. Heinrich and J.F. Cochran,
Can. J. Phys. 55, 821,(1977)

[39] K. Myrtle, The Temperature Dependence of the Transmission
of 24 GHz Radiation through Electrolytically Formed Nickel
Single Crystals, M.Sc. thesis, Simon Fraser University, 1983

[40] K. Urquhart, The Effect of a Non-local Conductivity on Microwave Transmission through Ferromagnetic Metals, M.Sc. thesis, Simon Fraser University, 1985

[41] W.F. Brown, Micromagnetics, Interscience Publishers, New York, 1963

[42] L. Kraus and Z. Frait, Czech. J. Phys. B23, 188(1973)

[43] G. Aubert, Y. Ayant, E. Belorizky and R. Casalegno, Phys. Rev. B 14, 5314(1976)

[44] R. Gersdorf, Phys. Rev. Lett. 40, 344(1978)

[45] E.A. Turov, Chapter 3 in S. Vonsovskii(ed.), Ferromagnetic Resonance, Pergamon Press, London, 1965

[46] J.R. MacDonald, Proc. Phys. Soc. London A64, 968(1951)

[47] R. Baartman, Microwave Studies of an Amorphous Ferromagnet, M.Sc. thesis, Simon Fraser University, 1981

[48] J.F. Cochran, B. Heinrich and G. Dewar, Can. J. Phys. 55, 787,(1977)

[49] J.D. Jackson, Classical Electrodynamics (2nd ed.), Wiley, New York, 1975

[50] G.T. Rado and J.R. Weertman, J. Phys. Chem. Solids 11, 315,(1959)

[51] M.G. Calkin and P.J. Nicholson, Rev. Mod. Phys. 39, 361(1967)

[52] J.F. Cochran and B. Heinrich, J. Appl. Phys. 50, 7729(1979)

[53] C. G. Montgomery(ed.), Technique of Microwave Measurements, Radiation Laboratory Series Vol. 11, McGraw-Hill, New York, 1947

[54] E.L. Ginzton, Microwave Measurements, McGraw-Hill, New York, 1957

[55] C.P. Poole, Electron Spin Resonance, A Comprehensive Treatise on Experimental Techniques, Interscience, New York, 1967

[56] W.J.McG. Tegart, The Electrolytic and Chemical Polishing of Metals, Pergamon Press, London, 1959

[57] G. Dewar, Ferromagnetic Antiresonant Microwave Transmission through Nickel, Ph.D. thesis, Simon Fraser University, 1978

[58] G. Feher, Bell System Tech. J. 36, 449,(1957)

[59] J. Schmidt and I. Solomon, J. Appl. Phys. 37,3719(1966)

[60] J.F. Cochran, B. Heinrich and G. Dewar,
Can. J. Phys. 55, 834,(1977)

[61] K. Borer and G. Fremont,
Nucl. Instr. and Meth. 154, 61(1978)

[62] R. Kaul and E.D. Thompson, J. Appl. Phys. 40, 1383(1969)

[63] H. Danan, A. Herr and A.J.P. Meyer,
J. Appl. Phys. 39, 669(1968)

[64] G.K. White and S.B. Woods,
Phil. Trans. Roy. Soc.(London) A251, 273(1959)

[65] M.J. Laubitz, T. Matsumara and P.J. Kelly,
Can. J. Phys. 54, 92(1976)

[66] F.C. Schwerer and J.Silcox, Phys. Rev. Lett. 20, 101(1968)

[67] T. Tokunaga, J. Sci. Hiroshima Univ. Ser. A 38, 215(1974)

[68] P. Goy and C.C. Grimes, Phys. Rev. B 7, 299(1973)

[69] A.V. Gold, J. Low Temp. Phys. 16, 3(1974)

[70] V. Kambersky, Proc. Int. Conf. on Magnetism(ICM-73)
Vol. 5, 124, Moscow, 1974

[71] V. Kambersky, Czech. J. Phys. B26, 1366(1976)

[72] V. Kambersky, Spin-wave Linewidth Calculations
in Ni and Fe, (unpub.)

[73] V. Korenman, Phys. Rev. B 9, 3174(1974)

[74] L. Berger, J. Phys. Chem. Solids 38, 1321(1977)

[75] B. Heinrich, D. Fraitova and V. Kambersky,
Phys. Stat. Sol. 23, 501(1967)

[76] A.V. Gold, J. Appl. Phys. 39, 768(1968)

[77] E.I. Zornberg, Phys. Rev. B 1, 244(1970)

[78] F. Weling and J. Callaway, Phys. Rev. B26, 710(1982)

[79] L. Hodges, H. Ehrenreich and N.D. Lang,
Phys. Rev. 152, 505(1966)

[80] D.N. Zubarev, Soviet Phys. Uspekhi. 3, 320(1960)